


Summer 2011

# Statistical Optimizations of Muscle Action Potentials Based on Modeling and Analysis of Ion Channel Dynamics

GyuTae Kim  
*Old Dominion University*

Follow this and additional works at: [https://digitalcommons.odu.edu/ece\\_etds](https://digitalcommons.odu.edu/ece_etds)

 Part of the [Biomedical Engineering and Bioengineering Commons](#), and the [Electrical and Computer Engineering Commons](#)

---

## Recommended Citation

Kim, GyuTae. "Statistical Optimizations of Muscle Action Potentials Based on Modeling and Analysis of Ion Channel Dynamics" (2011). Doctor of Philosophy (PhD), dissertation, Electrical/Computer Engineering, Old Dominion University, DOI: 10.25777/Sgka-wf05  
[https://digitalcommons.odu.edu/ece\\_etds/91](https://digitalcommons.odu.edu/ece_etds/91)

This Dissertation is brought to you for free and open access by the Electrical & Computer Engineering at ODU Digital Commons. It has been accepted for inclusion in Electrical & Computer Engineering Theses & Dissertations by an authorized administrator of ODU Digital Commons. For more information, please contact [digitalcommons@odu.edu](mailto:digitalcommons@odu.edu).

**STATISTICAL OPTIMIZATIONS OF MUSCLE ACTION  
POTENTIALS BASED ON MODELING AND ANALYSIS OF ION  
CHANNEL DYNAMICS**

by

GyuTae Kim  
B.E. February 1999, Hong-Ik University, Korea  
M.E. December 2004, University of Utah  
M.S. December 2008, University of Tennessee

A Dissertation submitted to the Faculty of  
Old Dominion University in Partial Fulfillment of the  
Requirements for the Degree of

DOCTOR OF PHILOSOPHY

ELECTRICAL AND COMPUTER ENGINEERING

OLD DOMINION UNIVERSITY  
August 2011

Approved by:

---

Frederic D. McKenzie (Director)

---

Mohammed M. Abdallah (Member)

---

Ravindra P. Joshi (Member)

---

Roland R. Mielke (Member)

## **ABSTRACT**

# **STATISTICAL OPTIMIZATIONS OF MUSCLE ACTION POTENTIALS BASED ON MODELING AND ANALYSIS OF ION CHANNEL DYNAMICS**

GyuTae Kim

Old Dominion University, 2011

Director: Dr. Frederic D. McKenzie

An Electromyogram (EMG) is an electrical signal, which is measured from a skeletal muscle during voluntary and involuntary contractions. EMGs are useful in interpreting pathological states of the musculoskeletal system. In particular, EMGs offer valuable information concerning the timing of muscular activity and its relative intensity. Various EMG models have developed with many different purposes from a pure mathematical model to a pattern structure model [17,46]. Sophisticated EMG models are necessary to examine the effects of small changes in muscular morphology and activities [46]. Due to the crucial importance of EMG models, all factors in the model should be precise and accurate. Especially, an intracellular action potential (IAP) model, the starting point of an EMG model, should be precisely generated because of its importance as the main component for an EMG model. Generally, the Rosenfalck IAP model [75,89] has been used because of its computational simplicity [59,72,77]. However, the Rosenfalck IAP model oversimplifies a real IAP, which has been experimentally measured, and it results in mismatching amplitudes and time duration between a real and modeled IAP.

This research proposes a mathematical IAP model using a series of modified gamma and erlang probability density functions. The optimization of the proposed IAP model was conducted by several different numerical methods, namely Gauss-Newton, Steepest

Descent, and Conjugate Gradient methods. These optimizing methods for the proposed muscle IAP model were validated by applying them to the experimental results of the Hodgkin and Huxley neuron action potential [11]. Due to the similarity in the mechanism of both nerve and muscle IAP generations, the validation shows that the methods and results are reasonably applied and obtained in the proposed muscle model, which for the first time incorporates properties that explain ion channel behavior in IAP generation.

This thesis is dedicated to my parents, JungMan Kim and YoungHye Bae, who are my mentors for life. Without their encouragements and sacrifices, I couldn't have finished one of my most important academic careers. I also thank my two sisters and their families for their endless support during my long school years. Finally, I want to thank my wife, SunHee Lee, who always trusts and supports me without any doubts.

## ACKNOWLEDGEMENTS

I have some people that I need to mention without whose help this work would never have been completed. First of all, my former academic advisor, Dr. Mohammed Ferdjallah, lead me to the success of this dissertation with his continuous encouragement and research inspiration. His thoughtful academic efforts and guidance showed me the interconnections between engineering and medicine, and helped me to have a broadened perception of Biomedical Engineering. I would also like to thank my current academic advisor, Dr. Frederic McKenzie, who strongly supported me in finishing this dissertation without any discontinuity. His care and supervision of my research have reassured me to continue my academic journey. I'm grateful to other committee members, Dr. Roland Mielke and Dr. Ravindra Joshi, for their help and guidance for the successful completion of this dissertation.

## TABLE OF CONTENTS

	Page
LIST OF TABLES .....	ix
LIST OF FIGURES .....	x
 Chapter	
1. INTRODUCTION .....	1
1.1 MOTIVATION AND PROBLEM STATEMENT .....	1
1.2 HODGKIN AND HUXLEY EXPERIMENTS .....	3
1.3 ACTION POTENTIALS: NERVE VS. MUSCLE .....	9
1.4 PREVIOUS ACTION POTENTIAL MODELS IN MUSCLE .....	10
1.5 APPROACH .....	14
1.6 ORGANIZATION .....	15
 2. PHYSIOLOGICAL BACKGROUND .....	 19
2.1 SKELETAL MUSCLE .....	19
2.2 MUSCLE FIBER .....	22
2.2.1 STRUCTURE .....	22
2.2.2 SLIDING FILAMENT THEORY .....	24
2.2.3 ACTION POTENTIAL .....	25
2.3 ION CHANNEL .....	27
2.3.1 VOLTAGE-GATED $\text{Na}^+$ CHANNEL .....	29
2.3.2 VOLTAGE-GATED $\text{K}^+$ CHANNEL .....	30
2.3.3 $\text{Na}^+/\text{K}^+$ ADENOSINE TRIPHOSPHATASE .....	30
2.4 ACTION POTENTIAL TRANSMISSION .....	31
 3. MATHEMATICAL BACKGROUND .....	 34
3.1 GAMMA PROBABILITY DENSITY FUNCTION .....	34
3.2 ELANG PROBABILITY DENSITY FUNCTION .....	35
3.3 NUMERICAL OPTIMIZATION .....	36
3.3.1 OBJECTIVE FUNCTION .....	37
3.3.2 GAUSS-NEWTON METHOD .....	39
3.3.3 STEEPEST DESCENT METHOD .....	42
3.3.4 CONJUGATE GRADIENT METHOD .....	43
 4. INTRACELLULAR ACTION POTENTIAL MODELING .....	 45
4.1 NEURON INTRACELLULAR ACTION POTENTIAL .....	45
4.1.1 DATA PREPARATION .....	45
4.1.2 CONSTRUCTION OF OBJECTIVE FUNCTION .....	47
4.1.3 OPTIMIZATION IN GAUSS-NEWTON METHOD .....	48

4.1.4	OPTIMIZATION IN STEEPEST DESCENT METHOD.....	52
4.1.5	OPTIMIZATION IN CONJUGATE GRADIENT METHOD.....	55
4.2	MUSCLE FIBER INTRACELLULAR ACTION POTENTIAL.....	56
4.2.1	DATA PREPARATION.....	56
4.2.2	CONSTRUCTION OF OBJECTIVE FUNCTION.....	58
4.2.3	OPTIMIZATION IN THREE METHODS .....	58
5.	MODEL VALIDATION & MODIFICATION .....	64
5.1	VALIDATION.....	64
5.2	PARAMETER DETERMINATIONS .....	66
5.3	VALIDATION FOR THE PROPOSED IAP MODEL .....	67
5.3.1	MODEL VALIDATION: SOURCE 1.....	69
5.3.2	MODEL VALIDATION: SOURCE 2.....	69
5.3.3	MODEL VALIDATION: SOURCE 3.....	70
5.4	MODIFICATION .....	70
6.	DISCUSSIONS.....	79
6.1	ION CHANNEL (CONDUCTANCE) MODELING .....	79
6.2	ION CHANNEL CONDUCTIVITY .....	81
6.3	TOTAL IONIC CURRENT.....	86
6.4	TRANSMEMBRANE CURRENT.....	87
6.5	APPLICATION OF ION CHANNEL .....	90
7.	CONCLUSION AND FUTURE WORKS .....	92
7.1	CONCLUSION.....	92
7.2	FUTURE WORKS.....	95
	REFERENCES .....	97
	VITA.....	103



## LIST OF TABLES

Table	Page
1. Different Muscle Fiber Types and their characteristics.....	21
2. Different Ion Concentration at Intracellular and Extracellular spaces across the cell membrane.....	28
3. Summary of computed parameters under different optimization methods in neuron IAP model.....	55
4. Summary of computed parameters under different optimization methods in muscle IAP model.....	62
5. Parameters based on the results of different optimization methods. ....	67
6. Summary of computed parameters by using different sources.....	74
7. Final parameters for a muscle IAP model.....	77

## LIST OF FIGURES

Figure	Page
1. Voltage Clamp Technique.....	5
2. Hodgkin and Huxley (H-H) Electric Equivalent Circuit.....	5
3. Nerve Action potential with ionic conductance .....	7
4. A measured and modeled Intracellular Action Potentials (IAP).....	11
5. Connective Tissue Wrappings of Skeletal Muscle.....	20
6. Structure of a skeletal muscle fiber, myofibril, and sarcomere.....	21
7. Typical Intracellular Action Potential (IAP) in a skeletal muscle.....	26
8. Brief Diagram of Na <sup>+</sup> and K <sup>+</sup> Ion Channels .....	28
9. Typical Path of Neural Stimulus from the brain to the tendon .....	32
10. The measured neuron IAP and its digitized IAP .....	46
11. Generated neuron IAP by Gauss-Newton with gamma PDF .....	50
12. Generated neuron IAP by Gauss-Newton with erlang PDF .....	50
13. Generated neuron IAP by steepest descent with gamma PDF .....	53
14. Generated neuron IAP by steepest descent with erlang PDF .....	53
15. Generated neuron IAP by conjugate gradient with gamma PDF .....	54
16. Generated neuron IAP by conjugate gradient with erlang PDF .....	54
17. The measured muscle IAP and its digitized IAP.....	57
18. Generated muscle IAP by Gauss-Newton with gamma PDF.....	59
19. Generated muscle IAP by Gauss-Newton with erlang PDF.....	59
20. Generated muscle IAP by steepest descent with gamma PDF .....	60
21. Generated muscle IAP by steepest descent with erlang PDF .....	60
22. Generated muscle IAP by conjugate gradient with gamma PDF.....	61
23. Generated muscle IAP by conjugate gradient with erlang PDF .....	61
24. Digitized measured muscle IAP data for validation.....	68
25. Removed initial membrane potentials of the digitized IAP data.....	68
26. Measured Source #1 and a generated IAP with the initial set #1 .....	71
27. Measured Source #1 and a generated IAP with the initial set #2.....	71
28. Measured Source #2 and a generated IAP with the initial set #1 .....	72
29. Measured Source #2 and a generated IAP with the initial set #2.....	72
30. Measured Source #3 and a generated IAP with the initial set #1 .....	73
31. Measured Source #3 and a generated IAP with the initial set #2.....	73
32. Normalized Erlang PDF with $\alpha_2=5$ .....	76
33. Normalized Erlang PDF with $\alpha_3=8$ .....	76
34. Modeled muscle IAP with measured IAPs .....	77
35. Modeled muscle Intracellular Action Potential (IAP) with its components.....	78
36. Generated conductances for Sodium and Potassium in nerve.....	82
37. Generated conductances for Sodium and Potassium in muscle .....	82
38. Na <sup>+</sup> conductances of muscle and neuron.....	83
39. K <sup>+</sup> conductances of muscle and neuron.....	83
40. Generated ionic currents for Sodium, Potassium, and leakage in muscle .....	85
41. Generated capacitor current in muscle. ....	85
42. Generated Transmembrane current in muscle.....	88

## **CHAPTER 1**

### **INTRODUCTION**

There are highly increasing demands to understand ion channel dynamics for their critical functions in the cell [71]. Ion channels provide the core paths for various ions and generate electrical signals by differences in ion concentrations. Mainly, these signals are used for the physiological communication between cells, and the correct signals can be produced only by well understood ion channel dynamics. Recently, more applications of ion channels have been addressed; for example, an ion channel is a new target in drug delivery [29,50]. Moreover, the studies of pain and many diseases at the cellular level often require ion channel dynamics and behaviors. Based on these current studies, the precise and correct generation of an electrical signal from the cell is possible when the concepts of ion channel dynamics are applied.

#### **1.1 MOTIVATION AND PROBLEM STATEMENT**

Skeletal muscle is the major inner contractile tissue of the human motor system. A muscle consists of hundreds of muscle fibers that are the specialized cells in muscle. These muscle fibers are functionally packed into a Motor Unit (MU), a systemic unit with a single motor neuron and its innervated muscle fibers. For a muscular excitation, the brain generates an electrical signal and sends it to the muscle through the spinal neurons. A motor unit in the muscular system is composed of one motor neuron and many muscle fibers. The signal arrives at a motor neuron and is sent to the innervated muscle fibers. This physical connection site between a motor neuron and a muscle fiber is a communication link called the Neuromuscular Junction (NJ). The axon terminal in this

junction holds many vesicles that contain neurotransmitters called acetylcholine. An arrived signal at the axon terminal stimulates the vesicles to open and release acetylcholine into the space between the motor neuron and muscle fiber. The released neurotransmitters bind to specific neurotransmitter receptors on the End Plate (EP) of a muscle fiber. The signal from the EP starts to open ion channels for ionic movement. An ion channel is an ionic path in the cell membrane, a bilayer structure covering the muscle cell. Each ion is permeable only through a specific ion channel. For example, a sodium ( $\text{Na}^+$ ) ion channel allows only  $\text{Na}^+$  ions to pass through it. Therefore, the electrical signal can trigger changes in ion concentrations by opening and closing many ion channels. These changes in ion concentrations, in turn, generate an electrical signal called the intracellular action potential (IAP).

Voluntary and involuntary contractions of muscle are caused by electrical signals, which are generated in the peripheral and central nervous system. These signals, called Electromyograms (EMGs), are measured and analyzed to study the activities of muscle. Generally, a complete EMG can be obtained by the summation of all muscle fiber action potentials (MFAP) in the muscle. MFAPs are electrical signals from a muscle fiber during muscular activity. For the computation of a MFAP, a weighting function related to measuring location and transmembrane current (or ionic current) is required. An IAP is generally used to compute the transmembrane current, based on the mathematical proof by Rosenfalck [75,89].

The main reason to use an IAP as a bioelectrical source in computing a MFAP is its relative ease in measuring, compared with the transmembrane current. According to Rosenfalck [75], the transmembrane current can be calculated by the second derivative of

the IAP [75]. However, the Rosenfalck IAP model was developed based on a simple signal pattern approximation [75,95]. This means that the Rosenfalck IAP model does not consider ion concentrations and ion channel activities, which are the core physical principles generating the IAP. Moreover, several issues such as mismatching results in amplitudes and time duration were raised when the Rosenfalck IAP model was used [95]. According to Nandedkar [95], the maximum value in computed transmembrane current using the Rosenfalck IAP model was 4 times smaller than the experimental value. Also, the duration time and rising time of the IAP and its second derivative were 2 times longer than those of the measured data. A rectified version of the Rosenfalck IAP model was developed by Nandedkar [95]. However, the Nandedkar IAP model also failed to overcome the mismatching problem in time duration of the IAP and its second derivative when compared with experimental data [17]. Therefore, neither Rosenfalck nor Nandedkar were successfully able to develop a valid IAP model. Their unrealistic models may lead to incorrect results if EMG is modeled and simulated based on these IAP models. Therefore, an accurate IAP model is critical to generating realistic findings in ion channel dynamics and potential activities on the muscle fiber.

## **1.2 HODGKIN AND HUXLEY EXPERIMENTS**

Hodgkin and Huxley's (H-H) experiments have significantly affected the modern understanding of neural excitability. Through their series of five articles published in 1952, they experimentally unveiled the interconnection between the nerve action potential and ionic conductance [10-14]. The nerve action potential is mainly generated by specific ions' movements, such as sodium ( $\text{Na}^+$ ), potassium ( $\text{K}^+$ ), chloride ( $\text{Cl}^-$ ), A-

type potassium ( $K(A)^+$ ), high-voltage activated calcium ( $Ca^{2+}$ ), calcium-dependent potassium ( $K(Ca)^+$ ) and persistent sodium (NaP) [19]. These ions' movements are enabled through ion channels, specifically voltage-dependent ion channels. Different ionic charges make ion channels open to specific ions and allow those ions to flow in or out of the cell. The ionic flow or ionic movement through an ion channel is called ionic current. The ionic current can be expressed by the multiplications of ionic conductance and the potential difference between the membrane potential and an equilibrium potential for a specific ion. According to the H-H experiments, the potential differences can be calculated or directly measured by the Nernst equation and the current clamp technique, respectively. Therefore, they are determined to be constants. This implies that ionic conductance is the only changing factor over time during an IAP generation. This was also the initial hypothesis by Hodgkin and Huxley for explaining their experimental results. In the 1950s, Hodgkin and Huxley counted only two ions, sodium ( $Na^+$ ) and potassium ( $K^+$ ), for nerve excitability and other unknown ions were treated as portions of leakage. Thus, only three ionic currents, namely  $Na^+$ ,  $K^+$ , and leakage, were counted to form the total ionic current in the H-H neuron experiment.

To measure the membrane activities during action potential, two important techniques were used: the space clamp and the voltage clamp. The space clamp is a technique to make all voltage dependent variables independent from the axial distance by replacing axoplasm with electrodes in a high volume conductivity solution. The axon from a giant squid was well fitted for this technique because of its amazing size, up to 1 mm in diameter, compared with other creatures' axons, normally less than several  $\mu m$  in diameter. In addition, a giant squid axon has only two types of voltage-dependent

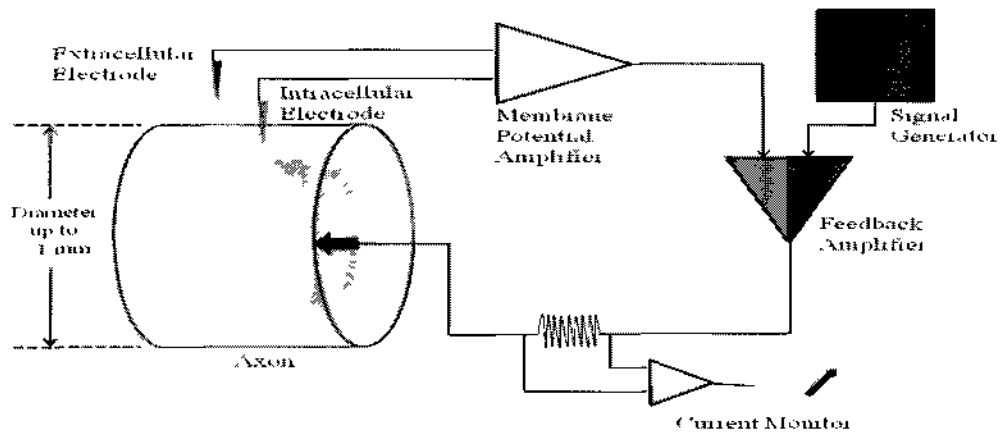


FIG. 1: Voltage Clamp Technique [110]. Two electrodes at intracellular and extracellular areas continuously measure the membrane potential, and it is sent to the feedback amplifier via the membrane potential amplifier. The feedback amplifier finds the difference between the clamped and membrane voltages, and it returns into the cell. The membrane current is continuously measured at the current monitor.

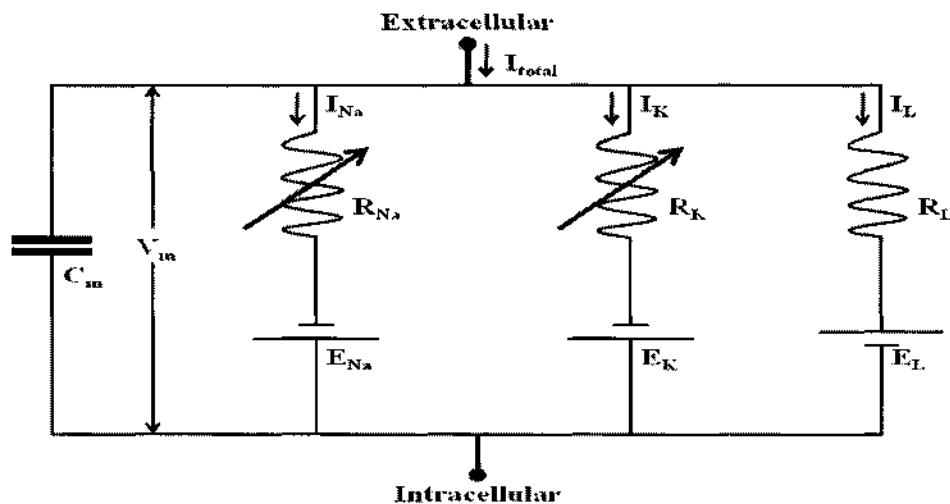


FIG. 2: Hodgkin and Huxley (H-H) Electric Equivalent Circuit (reproduced from the original figure) [11]. Membrane potential ( $V_m$ ), equilibrium potentials for sodium ( $E_{Na}$ ), potassium ( $E_K$ ), and leakage ( $E_L$ ) are suggested as constants. Ionic currents are expressed as  $I_{Na}$ ,  $I_K$ , and  $I_L$  for sodium, potassium, and leakage, respectively.

conductance,  $\text{Na}^+$  and  $\text{K}^+$ , on the nerve membrane. These advantages made it easier to apply the techniques and fundamental hypothesis.

The voltage clamp is a technique to measure the ionic current at a certain level of “clamp” voltage. A generated voltage is applied into the cell membrane through an inserted electrode, and the ionic current at the given voltage is measured. This technique provides the experimental results related to the dynamics of an ion channel. Since the majority of ion channels in a cell membrane are voltage-gated ion channels, most ion channels are operated by the changes of the applied voltage across the cell membrane. Therefore, the measured current by the voltage clamp technique mostly results from the dynamics of voltage-gated ion channels. At the same time, the changes in ionic current directly reflect the changes in ionic conductance.

Based on their discoveries, they designed an equivalent circuit (Figure 2) which can show the electrical properties in a segmented nerve membrane. The H-H equivalent circuit presents the total ionic current as determined by the summation of independent ionic currents of different ion species. As shown in the H-H circuit model, the total ionic current,  $I_{ION}$ , is given by:

$$I_{ION} = \sum_{x=1}^3 I_x \quad (1.1)$$

where  $x$  presents a different ion species, and the summation is limited by 3 because of the H-H experimental initial hypothesis [11]. Again, each ionic current can be computed



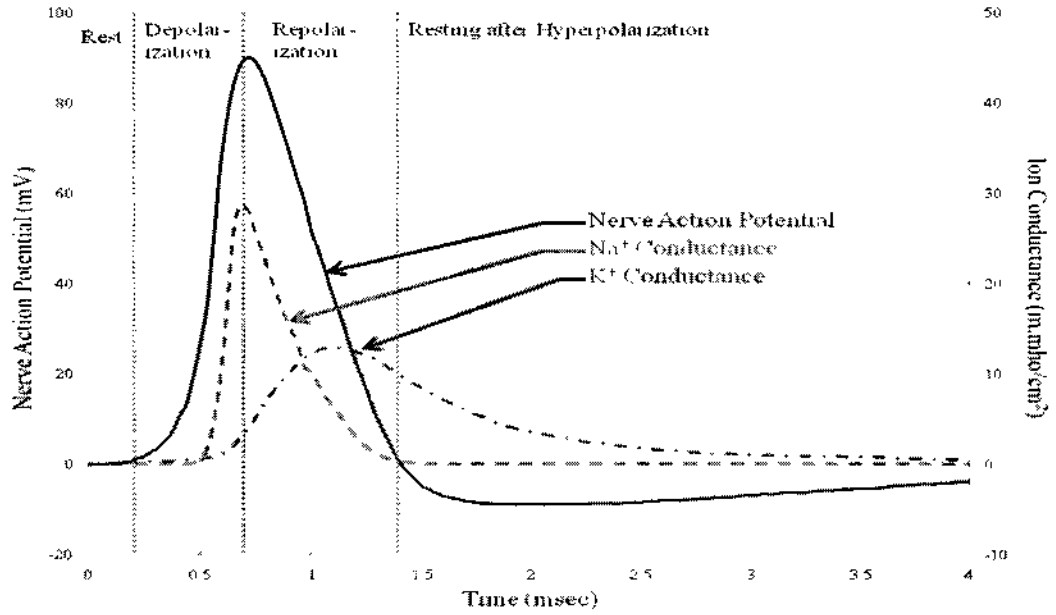


FIG. 3: Nerve Action potential with the conductance for Sodium ( $\text{Na}^+$ ) and Potassium ( $\text{K}^+$ ) (reproduced from the original figure) [11]. A generated action potential (V), the conductance for sodium ( $g_{\text{Na}}$ ), and that for potassium ( $g_{\text{K}}$ ) are displayed with the total conductance ( $g$ ).

by the multiplication of ionic conductance and the difference between the membrane potential and the ionic potential for each ion species.

$$I_x = g_x(V_m - E_x) \quad (1.2)$$

where  $g_x$  is the conductance for  $x$  ion, and  $V_m$  and  $E_x$  are the membrane potential and the equilibrium potential, respectively. Due to the H-H hypothesis, the ionic current can be finally expressed as follows:

$$I_{\text{ION}} = g_{\text{Na}}(V_m - E_{\text{Na}}) + g_{\text{K}}(V_m - E_{\text{K}}) + g_{\text{L}}(V_m - E_{\text{L}}) \quad (1.3)$$

The total membrane current,  $I_{\text{total}}$ , is obtained by the summation of the ionic current and

the membrane capacity current as shown in the H-H equivalent circuit, which gives the following equation:

$$I_{\text{total}} = I_{\text{ION}} + C_m \frac{dV_m}{dt} \quad (1.4)$$

where  $C_m$  is the membrane capacity. The H-H equivalent circuit could be created because of the critical assumption that each ionic conductance independently responds to the changing membrane potential. Based on this assumption, Hodgkin and Huxley examined the conductance for sodium ( $\text{Na}^+$ ) and potassium ( $\text{K}^+$ ) with different voltage levels. Through their experiments, they found that the  $\text{Na}^+$  conductance lasted only several milliseconds, but  $\text{K}^+$  conductance lasted as long as a clamped voltage was applied. Finally, Hodgkin and Huxley could demonstrate the major influences on the membrane potential from two ionic currents,  $I_{\text{NA}}$  and  $I_{\text{K}}$ , by tracking their changing ionic conductances. This experimental conclusion is well expressed in an action potential figure with ionic conductance (Figure 3).

As known in electrical concepts, conductance is the inverse of electrical resistance. Therefore, high conductance implies that  $\text{Na}^+$  and  $\text{K}^+$  ions can pass through the membrane easily. However, each ionic conductance for  $\text{Na}^+$  and  $\text{K}^+$  responds differently to the change of transmitted voltage which is obvious since the duration of  $\text{Na}^+$  conductance is transient, and  $\text{K}^+$  conductance lasts as long as the transmitted voltage is applied. As shown in Figure 3, this results in two independent ionic conductances during action potential generation. The first phase in the action potential model, depolarization, is mostly governed by the fast increase in  $\text{Na}^+$  conductance. During the second phase, repolarization, the combined effects from the changes in  $\text{Na}^+$  and  $\text{K}^+$  conductances affect

the action potential. This causes a relatively slow process during repolarization. Even after repolarization, the  $K^+$  conductance sustains by slowly decreasing, and it causes the third phase, hyperpolarization. Even though no changes are shown in muscle, there are other ions', mainly chloride ( $Cl^-$ ), conductances involved in recovering to the resting membrane potential in the nerve. Due to their minor effects on the action potential, Hodgkin and Huxley treated the ions with minor effects as a combined conductance, called leakage conductance,  $g_L$ .

### **1.3 ACTION POTENTIALS: NERVE VS. MUSCLE**

The relationship between action potential and independent ionic conductances has been experimentally proven by Hodgkin and Huxley. Ionic conductance primarily depends on the activities of an ion channel for specific ion species. Thanks to the discoveries by Hodgkin and Huxley, we know that the properties of ion channels for different ion species have no effect on each other, and they work independently. It implies that an action potential can be generated if each ionic conductance is modeled correctly. In addition, an action potential with independently combined ionic conductances can easily show the critical activities of ion channels, which was experimentally concluded and modeled by Hodgkin and Huxley.

The original Hodgkin and Huxley experiments were limited to nerve tissue. However, ionic movements through ion channels during action potential are very similar in nerve and muscle. In both, there are excitable cells, neurons in nerve and muscle fibers in muscle. These specialized cells are stimulated and generate an electric signal. In neurons, the electric signal is transmitted to neighboring neurons and relaxes as physiological

information among neurons. In skeletal muscle, this electrical signal causes a muscular contraction that mostly terminates in a tendon, which is a connective tissue between muscle and bone. During the generation of action potential, sodium ( $\text{Na}^+$ ) and potassium ( $\text{K}^+$ ) play the main roles in both nerve and muscle. During the depolarization phase, the conductance for  $\text{Na}^+$  rapidly increases and affects the sharp increase of the action potential in both. After reaching the highest peak point, the conductance for  $\text{Na}^+$  drops quickly but that for  $\text{K}^+$  increases in a relatively slow manner. This results in slow repolarization. After repolarization, there is a slight difference in the shape of action potentials in nerve and muscle; there is no hyperpolarization phase in muscle IAP. In nerves, the excessive  $\text{K}^+$  conductance causes more negative amplitude than the resting membrane potential and it is compensated for by the increase of chloride ( $\text{Cl}^-$ ) conductance. In muscle, however, there is no hyperpolarization, which indicates that fewer different ion species are involved in muscle than in nerve action potential. Most changes in muscle action potential can be assumed to be controlled by  $\text{Na}^+$  and  $\text{K}^+$ . Therefore, the design of the muscle action potential is easier because the smaller number of ion species means small effects in the model of the action potential. Therefore, the muscle action potential can be modeled by three ionic components:  $\text{Na}^+$ ,  $\text{K}^+$ , and leakage.

#### **1.4 PREVIOUS ACTION POTENTIAL MODELS IN MUSCLE**

In modeling an Electromyogram (EMG), a single muscle fiber action potential (MFAP) is the core element. The most known analytical intracellular action potential (IAP) model is the Rosenfalck IAP model [75]. In 1993, Stashuk [27] showed a technique for simulation of an EMG by using Rosenfalck IAP models. In 1994, Dumitru et al. [21] directly used

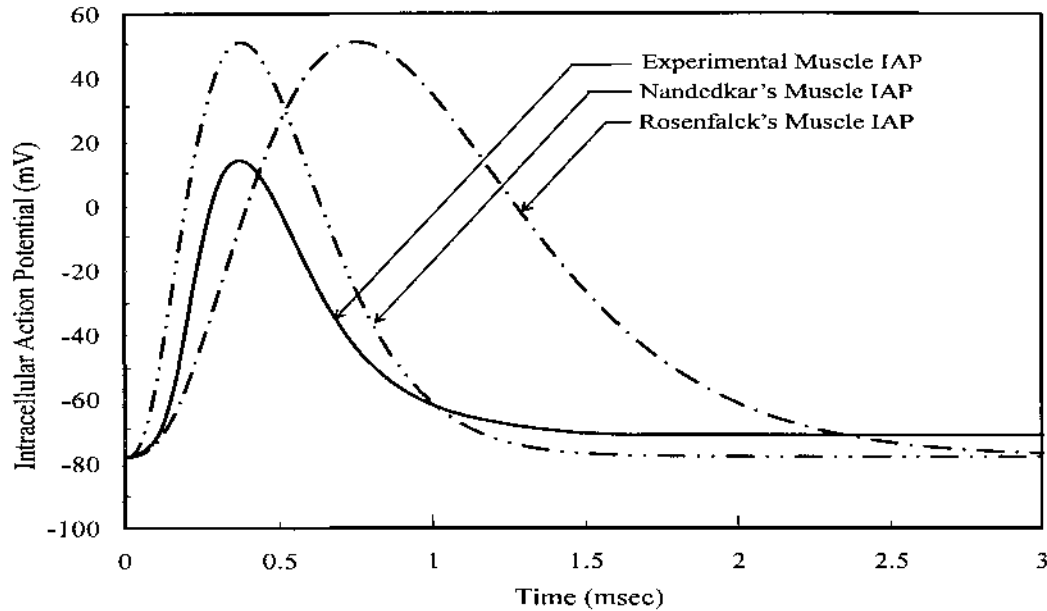


FIG. 4: Measured and modeled Intracellular Action Potentials (IAP). Experiment-derived Muscle IAP in solid line, Rosenfalck IAP model in dashed dotted line, and Nandedkar IAP model in dashed double dotted line.

the Rosenfalck IAP model for the determination of a single MFAP. In 1999, Merletti et al. [80] applied the Rosenfalck IAP model to simulate a surface myoelectric signal model without any modifications. In 2000, Dunchêne et al. [46] also adopted the Rosenfalck IAP model in the generation of a complete EMG. However, the authors identified an incorrectness of the Rosenfalck IAP model and attempted several continuous efforts in rectifying the IAP model. However, in the end, they simply used the Rosenfalck IAP model with different default values. In 2004, Mammrberg et al. [16] used the Rosenfalck IAP model in developing a fast technique for the generation of a MFAP. In the same year, Lowery et al. [72] used the Rosenfalck IAP model as the main bioelectrical source

to generate MFAP at different positions in the muscle. As shown in many MFAP and EMG models, the Rosenfalck IAP model has been considered a reliable and relatively correct IAP model. In 2005 and 2006, the Rosenfalck IAP model was used as a reference to develop an even more accurate IAP model [16,60].

Ultimately, the Rosenfalck IAP model had mismatching values in the amplitudes and time durations of the IAP (Figure 4). In 1983, Nandedkar and Stålberg [95] suggested a modified analytical expression of the IAP by substituting a doubled IAP propagation distance. This method solved the problem of mismatching amplitudes in the Rosenfalck IAP model, but the Nandedkar IAP model still contained unrealistic time durations (Figure 4). In 1993, van Veen et al. [17] attempted to find the most reliable sources for the MFAP by comparing different bioelectrical sources from an analytical modeled source to a measured transmembrane current. In their study, the authors emphasized the distorted results of the Rosenfalck and the Nandedkar IAP models by using the comparisons with a measured data [17].

To rectify and improve these incorrect IAP models, various efforts have been made. For these efforts, there are two typical tendencies: simple modification of the Rosenfalck IAP model and the summation of separate signals. The Nandedkar IAP model [95] is one of the representative methods that modify the Rosenfalck IAP model. This method is very simple and straightforward. Based on the Rosenfalck IAP model, the default values in the model are changed to match a real IAP. Because the Nandedkar IAP model directly uses the Rosenfalck IAP model, there are no more computational burdens or time consuming processes. However, this method still contains unrealistic time durations of IAP even after changing the default values as reported. The other method, the separate

signal summation, takes a different approach to generate the IAP model. A measured IAP can be divided into two, three or even four separate phases depending on the purposes of a study. These phases are the rising, the rapid falling, and the slow falling phases. According to Falces et al. [53,54], there is one more phase, the transition phase, between the rapid falling and the slow falling phase. The method of separate signal summation uses these divided phases as independent signals. The Dimitrov and Dimitrova (D-D) IAP model [37,57,58] is a separate signal summation method that assigns an analytical expression for each phase. However, the simple analytical expression cannot help to understand the ionic movements in IAP profiles. In particular, the summation of independent signals in each phase generally results in discontinuity in the second derivative, which is an unavoidable computational process in an EMG model [54,97-99]. To overcome this problem, Arabadzhiev et al. [97-99] suggested a single analytical function for an IAP model. However, a linear summation of enumerated functions in the Arabadzhiev's IAP model was not able to overcome the limitation contained in the D-D IAP model.

As can be deduced from this discussion, many researchers worked on the development of an IAP model. However, none of the previous IAP models have satisfied or explained all essential sources for IAP profiles. Therefore, a new IAP model is required that satisfies the following aspects:

- (1) Realistic Amplitudes and Time Duration,
- (2) Ionic Movements and Ion Channel Morphology,
- (3) Easy Mathematical Computation and Implementation.

## 1.5 APPROACH

Based on the H-H experiment conclusions, an analytical expression with three independent ionic properties was formed as an objective function. The ionic properties were expressed by using a modified gamma probability distribution function and an erlang probability distribution function, which are assumed to show the number of ion channel states and the speed of ionic flow. These two factors were the main components to decide the ionic properties. As discussed in the H-H experiments, the limits were set to three: sodium ( $\text{Na}^+$ ), potassium ( $\text{K}^+$ ), and leakage. To validate that the proposed methods were correct, one experimentally measured IAP [11] from a nerve cell was compared with simulated results from a model developed using the proposed methods. The validated methods were then used to create a muscle IAP model. After a muscle IAP was modeled by using measured muscle IAP data [17], the proposed method to generate the muscle IAP model was compared with other measured IAP data [75,105] for validation and modification.

The designed objective function was curve-fitted into the measured IAP data. The following equations in 1.5 and 1.6 show a gamma probability density function for a single ion channel conductance and its expanded expression for an IAP model, respectively.

$$g_I(t) = \gamma t^\alpha e^{-\beta t} \quad (1.5)$$

$$IAP_{model}(t) = \sum_{i=1}^3 \gamma_i t^{\alpha_i} e^{-\beta_i t} \quad (1.6)$$



where  $t$  is time, and  $i$  shows the number of independent ion species, including the leakage ion channel. Three ion channel conductance models are expressed in this IAP model. In all, nine unknown parameters,  $[\alpha_1, \alpha_2, \alpha_3, \beta_1, \beta_2, \beta_3, \gamma_1, \gamma_2, \gamma_3]$ , are assigned based on the model expression. Due to the limitation of optimization techniques, it is nearly impossible to have a complete zero error between the reference and objective function, which can result in parameter values that are not unique. Therefore, several different optimization techniques were used to examine the variability of the obtained values. In this dissertation, Gauss-Newton, Steepest Descent, and Conjugate Gradient methods were used to find the final values of the unknown parameters. For examining the properties of ion channels, the values in  $\alpha$  and  $\beta$  were carefully analyzed and discussed. These parameters,  $\alpha$  and  $\beta$ , in each ion channel conductance model are believed to closely connect with the biological characteristics such as the number of ion channel states and the speed of ion movement across the ion channels.

The main objective of this dissertation is to find a new IAP model, which represents the realistic values of IAP in amplitudes and time durations. Furthermore, the newly developed IAP model is expected to show the morphological properties of ion channels by considering the basic mechanisms in IAP generation. Initially, a new IAP is modeled and simulated for advanced Electromyogram (EMG) generation. However, it eventually becomes a study of an ion channel and its conductance. Through this new IAP model, the ion channel activities underlying action potentials can be understood more clearly, and various applications for this model are expected to grow significantly.

## **1.6 ORGANIZATION**

This dissertation is composed of separate chapters based on their main topics. The

physiological and mathematical backgrounds are covered in chapters 2 and 3. In chapter 4, IAP model generation is presented based on the given mathematical background. The validation of the developed IAP model is described in chapter 5. Several applications of the IAP model are introduced in chapter 6. In addition, the detailed dynamic properties of ion channels are analyzed and discussed. Finally, the future work and dissertation conclusion are presented in chapter 7. Following are specific summaries of each chapter.

**Chapter Two** provides a brief explanation of the physiological background. Muscle and muscle fiber, the fundamental component of muscle, are thoroughly examined, and the mechanical mechanism in muscle fiber during muscle contraction is explained in detail. In addition, the different types of muscle fiber are reviewed, and their brief characteristics are presented. Ion movement and the dynamics of ion channel in cell excitation are presented in this chapter. Ion movements are the main causes that generate IAP and the dynamics of ion channels are the key to understanding the kinetics of ion movements. To discuss the properties of ion channels through IAP modeling, other ion channel models are also briefly presented. In particular, the relationship between IAP and the dynamics of ion channel is explained in modeling aspects.

**Chapter Three** presents the mathematical basis for IAP modeling. The historic background that the gamma probability distribution function has been widely used in IAP modeling is given. The relationship between gamma and erlang probability distribution functions is presented, and its physiological meanings are provided. Three different optimization techniques, namely Gauss-Newton, Steepest Descent, and Conjugate Gradient methods, are explained. Their pros and cons are characterized and discussed. In particular, the limitations of these optimization techniques are discussed and some

suggestions are provided.

**Chapter Four** gives the detailed processes of IAP modeling. Based on the proposed objective function with gamma and erlang probability distribution functions, three optimization techniques are applied to generate IAP models. In each optimization method, nine unknown parameters are determined, and some of them are used to explain the physiological characteristics.

**Chapter Five** presents the validation of the generated IAP model by comparing several measured IAP. From previous studies, some measured IAP data were obtained by digitizing them. These experimentally measured IAPs are directly compared with the generated IAP model. By applying some limits to variables, the generated IAP model is analyzed and investigated.

**Chapter Six** suggests some applications based on ion channel dynamics, which is the fundamental basis of IAP modeling. Currently, many research areas in drug delivery, pharmacology, and neurosciences require understanding the properties of ion channels. The difficulties and limitations in optical technologies demand accurate ion channel models to predict physiological changes at the cellular level. In addition, detailed discussions of the newly generated IAP model are provided. As shown in H-H experimental conclusions in nerve, the relationship between IAP and ionic conductance is investigated in muscle. From the modeling aspects, the differences of IAP in nerve and muscle are investigated, and the main causes are explained based on the changes in ionic conductance.

**Chapter Seven** provides final conclusions based on the generated IAP model. In this chapter, the overall work and discussions are summarized and some restrictions are

discussed. Based on the discussions, future works related to this dissertation are recommended.

## CHAPTER 2

### PHYSIOLOGICAL BACKGROUND

Muscle is a contractile inner tissue. Mainly, muscle can be classified into three different types, skeletal, smooth, and cardiac muscles, depending on their functional characteristics. Skeletal muscle, also called voluntary muscle, is directly involved with body formation and movement by attaching to bones. This type of muscle controls the conscious postures based on the transmitted neural signal from the brain and the central nervous system (CNS). Smooth muscle is an involuntary muscle, which is located around the boundaries at different organs, such as arteries, veins, urinary bladder, respiratory tract, and the eye's iris. Cardiac muscle is muscle found in the heart.

#### 2.1 SKELETAL MUSCLE

Skeletal muscle is composed of hundreds of muscle fibers in thin contractile layers. These fibers are interconnected physically and functionally. A physical connection of muscle fibers, called fascicle, is wrapped by perimysium, a type of connective tissue. The structural flexibility of fascicles is critical in locomotion by allowing changing length [63,67]. The functional connection of its muscle fibers, called a Motor Unit (MU), is composed of a single motor neuron and its innervated muscle fibers. In both connections, the muscle fiber is a core element to form a structural and functional structure. Depending on the sizes of muscles, the numbers of muscle fibers vary. In skeletal muscle, all muscle fibers are organized in parallel bundles, enabling all muscle fibers in a muscle to contract and relax together efficiently. In a fascicle, a type of connective tissue, called endomysium, exists by filling the spaces among muscle fibers.

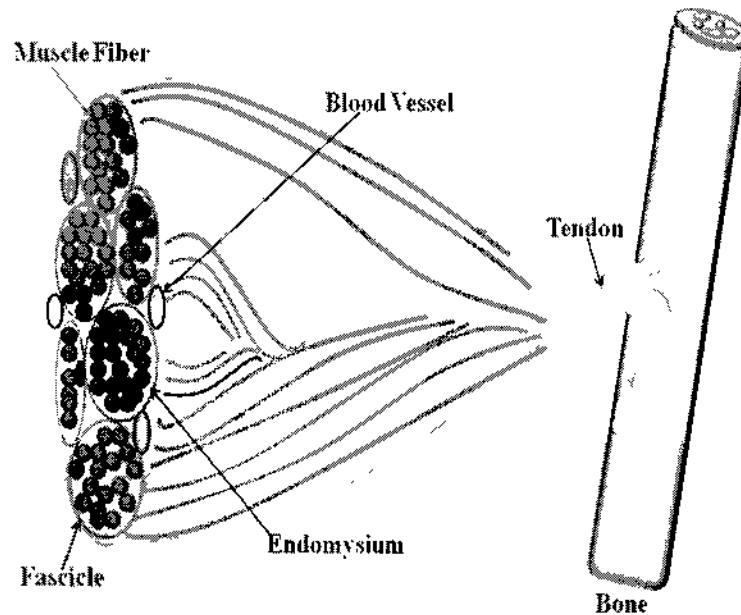


FIG. 5: Connective Tissue Wrappings of Skeletal Muscle. Muscle fibers are wrapped into fascicles physically. Tendon plays the main role in connecting muscle to bone. Epimysium covers the entire skeletal muscle protecting it from abrasion with other muscles and bones.

Endomysium contains collagen fibers and continuously connects to the tendons and the perimysium. Between fascicles, there are blood vessels and they help to supply oxygen for energy generation. The entire skeletal muscle is enveloped in epimysium, which is composed of connective tissues. Epimysium protects muscles from the abrasion of other muscles and bones. A tendon is a strong bundle of connective tissue, mainly composed of collagen and water. The major function of tendons is to connect muscle to bone and pass a transmitted force. Recent research shows that the elasticity of tendon directly affects muscular function in locomotion [83,87].

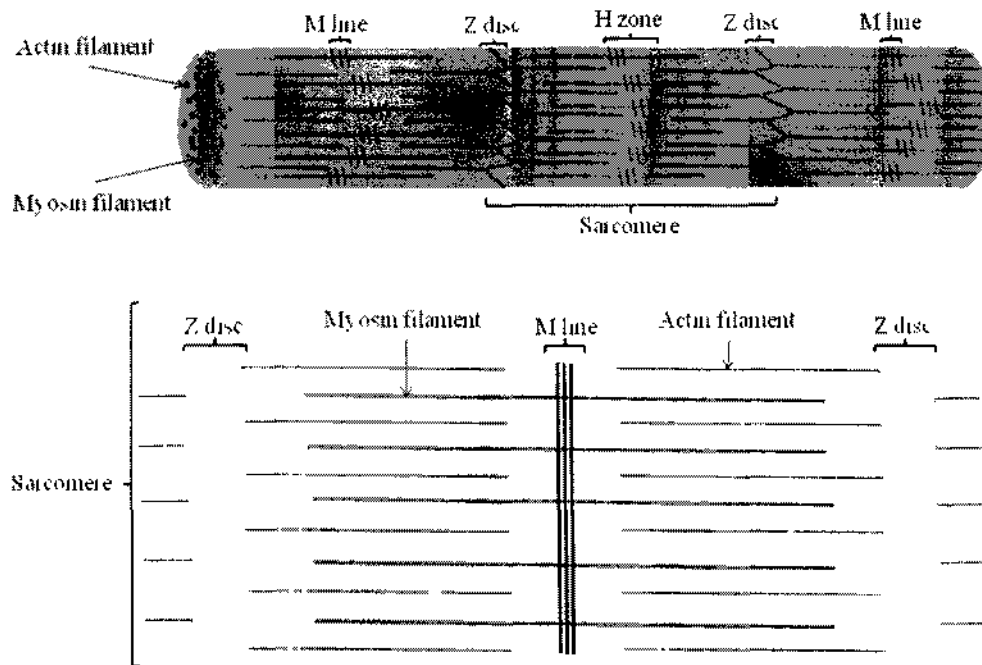


FIG. 6: Structure of a skeletal muscle fiber, myofibril, and sarcomere. Muscle fiber is composed of numerous myofibrils. A myofibril has longitudinal connected sarcomeres, which have two types of proteins, actin and myosin filaments.

TABLE 1: Different Muscle Fiber Types and their characteristics. The speed of contraction is different because of the different energy producing mechanisms.

Muscle Fiber Types	Type I	Type IIa	Type IIb
<b>Contraction Speed</b>	Slow	Fast	Very Fast
<b>Resistance to Fatigue</b>	High	Middle	Low
<b>Involving Activities</b>	Aerobic	Long Term Anaerobic	Short Term Anaerobic
<b>Generated Force</b>	Low	High	Very High
<b>Oxidative Capacity</b>	High	High	Low
<b>Glycolytic Capacity</b>	Low	High	High

## **2.2 MUSCLE FIBER**

Muscle fiber, also called myofiber, is a contractile cell with a cylindrical shape. It is a fundamental unit composing a muscle through a parallelized connection. It is generally categorized into three different types depending on its various characteristics such as contraction time, the size of motor neuron, fatigue resistance, etc.

### **2.2.1 STRUCTURE**

A general fiber has a diameter that ranges from 5 to 100  $\mu\text{m}$  and a length that can be many centimeters. The origination of muscle fiber is the myoblast, an individual embryonic muscle cell, and some myoblasts become a myotube in a period of embryonic developments. A myotube has many nuclei in a single plasma membrane and differentiates into a muscle fiber. Muscle fiber is composed of many parallel subunits called myofibrils. Again, a myofibril has longitudinal connected subunits, called sarcomeres. Each sarcomere has two special types of proteins, actin thin and myosin thick filaments, in a tightly organized pattern. Depending on the positions of the two proteins, there are specific sections on a sarcomere. M-line is the center of a sarcomere, and contains enzymes for the energy metabolism of muscle fibers. Each sarcomere is bounded by Z-disc, also called Z-line, which contains  $\alpha$ -actinin, a type of protein. Typically, the sarcomere is formed by the interdigitation of myosin and actin filaments. The  $\alpha$ -actinins in Z-disc attach to the actin filament and fix the locations of actin filaments. Actin and myosin filaments are overlapped and make the densest portion called A-band. Under microscopic examination, A-band represents the darkest color because of its structure. Contrary to A-band, there is the thinnest portion, H-zone. This



specialized area holds the myosin filaments and is located in the middle of the A-band. The I-band is located at the ends of the A-band and contains Z-disc.

Two proteins, actin and myosin filaments, are the core subunits of a sarcomere. An actin filament is composed of many globular proteins, called G-actin, and other attached proteins to F-actin, which is polymerized by G-actins. In each G-actin, there is a specialized binding site for the myosin head-binding site. The main attached proteins in an actin filament are tropomyosin and troponin. These proteins are involved in controlling muscle contraction. A myosin filament consists of the combinations of three pairs of molecules. Two of the pairs are identical molecules called myosin heavy chain. Each myosin heavy chain contains a globular region called a myosin head. This specialized region has the binding sites for actin and plays the main role in the contraction of a myofibril.

Generally, a muscle fiber is divided into three main types: type I, type IIa, and type IIb. Type I fibers slowly contract by using cellular respiration. Due to their power generation mechanisms, type I fibers can sustain their contractions for a relatively long time. Type I fibers also show high resistance to fatigue, but the produced power is relatively low. Type IIa fibers have a faster contraction time than type I fibers. Compared with type I fibers, type IIa fibers have less endurance. Even though the resistance to fatigue of type IIa fibers is fairly high, the resistance is lower than that of type I fibers. Type IIb fibers have a very fast contraction time, and the produced power in a limited time is also very high. Compared with other fiber types, type IIb fibers have much lower resistance to fatigue and, thus, a short time for maintaining power.

### 2.2.2 SLIDING FILAMENT THEORY

The geometry of parallel and serial arrangements in muscles has important effects on the mechanical muscle contraction and relaxation. During the contraction of muscle fibers, it is not necessary for muscle fiber components to be shortened. Instead of physical shortenings of myosin and actin filaments, the cross movements in myofibrils under the interdigitated connections of myosin and actin filaments are used for the whole muscle contraction.

A transmitted impulse from the brain and nervous system arrives at the neuromuscular junction, which is the functional connection between the terminals of a nerve and muscle fiber. The impulse triggers the release of neurotransmitters, acetylcholine (ACh). The diffused AChs bind to their receptors on the motor end plate of the muscle fibers and trigger a muscle action potential. During the muscle fiber contraction, the generated action potential travels along the surface of the muscle fiber. The generated muscular action potential is transmitted into the muscle fiber at the T tubule, which is a deep invagination on the surface of the membrane. The sarcoplasmic reticulum (SR), a specialized organelle to regulate the level of calcium ( $CA^{2+}$ ) ions in a muscle fiber, is located around the T tubule. After a neural impulse is transmitted into the muscle fiber, the inhibitor enzyme, acetylcholinesterase (AChE), terminates AChs to prevent another action potential from arising until more AChs are released from the motor neurons. The flowing action potential stimulates the SR to release  $CA^{2+}$ . The flooded  $CA^{2+}$  binds to troponin on the actin filament and exposes the binding sites for myosin. The myosin head in the myosin heavy chain pulls the actin to the center of the sarcomere by the repeated attaching and detaching processes. After the action potential

ends,  $Ca^{2+}$  are removed by active transport into the SR. The contraction of a muscle fiber is terminated when the myosin binding sites are blocked.

### 2.2.3 ACTION POTENTIAL

A cell is surrounded and protected by a specialized lipid<sup>1</sup> bilayer called a cell membrane. A typical cell membrane is composed of three types of lipids: phosphoglycerides, sphingolipids, and sterols. Of these lipids, phosphoglycerides and sphingolipids contain the dual amphipathic nature, which means the hydrophilic (water-soluble) and hydrophobic (water-insoluble) characteristics at each end of the lipid. Significantly, the hydrophilic part, called the polar head of a lipid, is exposed to the interior and exterior cellular environments. It prevents any electrically charged particles, typically ions, from passing directly through the cell membrane. For the pathways of specific ions, there are specialized gates, called ion channels. Due to their selectivity, a potential difference is created between the inside and the outside of the cell membrane. The same structural properties are maintained in muscle fibers.

During no cellular excitations, the interior and the exterior cell membrane have different ionic gradients because of the different ion concentrations. Generally, there are excessive amounts of sodium ( $Na^+$ ) and chloride ( $Cl^-$ ) at the outside and excessive amounts of potassium ( $K^+$ ) on the inside of the membrane during no cell excitations. This difference in the ionic concentration gradients is maintained until other stimuli from the nervous system through motor neurons are transmitted to muscle fibers. A typical membrane potential in muscle during the resting state is -70 mV to -90 mV.

---

<sup>1</sup> A group of biological molecules, which are not soluble in water.

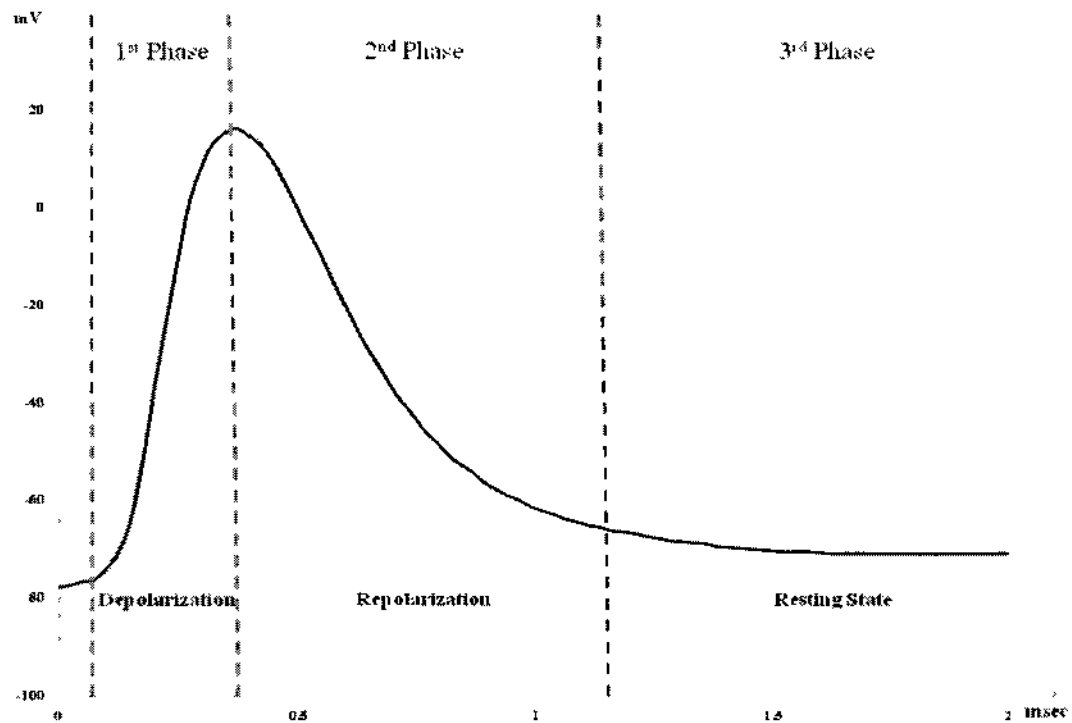


FIG. 7: Typical Intracellular Action Potential (IAP) in a skeletal muscle with the separated phases. The fast initial increase, called depolarization, is the first IAP phase. The second phase is the period that the IAP goes back to polarized values, which is repolarized. Finally, the potential has the resting state after IAP dynamics are relieved.

The neurotransmitters, AChs, from a motor neuron trigger ion channels to open by binding to their receptors on muscle fibers. The open ion channels for a specific ion increase the ionic conductance for the ion, which results in the easiness in the ionic inward or outward flows. Initially, the  $\text{Na}^+$  ion channels are open soon after the neural stimulations start. This causes fast inward flows of  $\text{Na}^+$ , and it governs depolarization in the action potential. As indicated in the resting membrane potential, the inside muscle fiber is negatively charged. Therefore, the positively charged ions flow into the cell membrane when a potential steady state is broken. Of the main ion species in the

potential generation across the membrane, the positively charged ions are  $\text{Na}^+$  and  $\text{K}^+$ . The ion channels for both ions are open when the action potential starts to be generated. However, the speed rates of the ionic inward and outward flows are different: faster inward  $\text{Na}^+$  flow than outward  $\text{K}^+$  flow. Also, the lasting times of  $\text{Na}^+$  and  $\text{K}^+$  conductance in the applied potentials are well explained in the H-H experimental results. Therefore, the fast inward  $\text{Na}^+$  flow with shorter lasting time affects the fast depolarization, and the slow outward  $\text{K}^+$  flow with longer lasting time governs the slow repolarization in an action potential. In other words, the ion channels for  $\text{K}^+$  are open longer than those for  $\text{Na}^+$  during the action potential.

The action potential in the muscle fiber is a self-propagating force. Once triggered by the neural stimuli, the muscular action potential travels along the surface of a muscle fiber with an approximate velocity of 4 m/sec. This specific traveling speed is called conduction velocity, and it primarily depends on the diameter of the fiber. After the first action potential occurs at the segmented fiber around the end plate region, the action potential is repeatedly generated at each segment until it arrives at the tendon. With this method, the action potential spreads like an electrical wave over the membrane.

### **2.3 ION CHANNEL**

An ion channel is a transmembrane protein, providing a specialized path for ions in the cell membrane, which is composed of bilayered phospholipid molecules. The cell membrane enables a cell to maintain its unique characteristics. However, cells need to communicate with other cells for specific biological regulation. For this purpose, cells send and receive electrical signals by allowing ions to flow with inward or outward

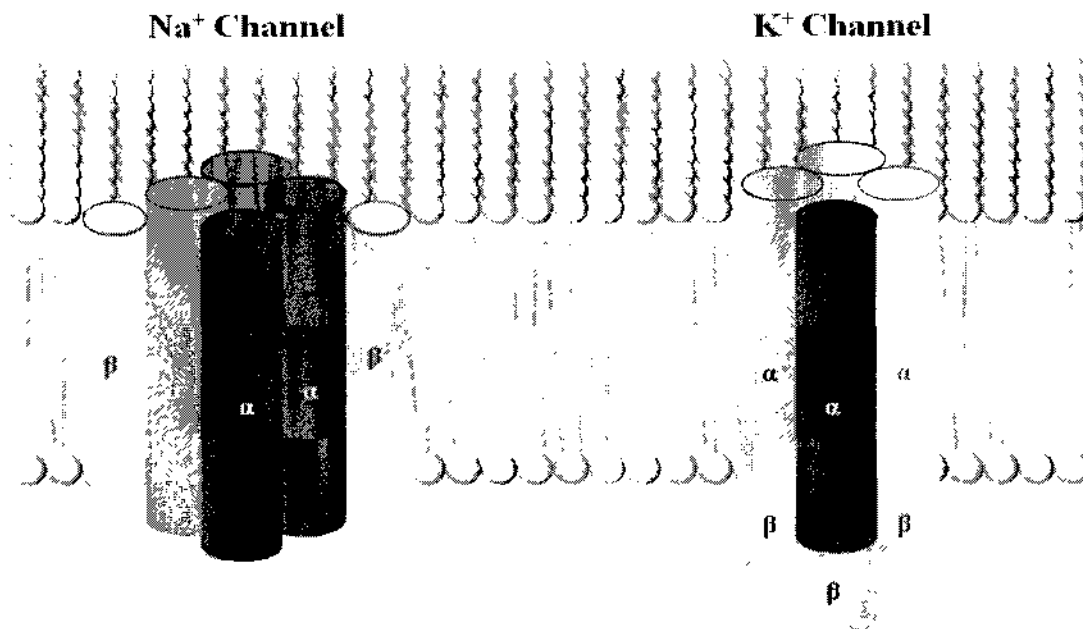


FIG. 8: Simplified Diagram of Na<sup>+</sup> and K<sup>+</sup> Ion Channels. A Na<sup>+</sup> ion channel is composed of four α-subunits and several associated β-subunits, depending on the localization of ion channels. A K<sup>+</sup> ion channel has four α-subunits with an auxiliary β-subunit for each α-subunit, which are arranged around the channel center.

TABLE 2: Different Ion Concentrations at Intracellular and Extracellular spaces across the cell membrane. During resting state, the excessive amounts of sodium (Na<sup>+</sup>) and chloride (Cl<sup>-</sup>) are maintained at the extracellular area and the excessive amount of potassium (K<sup>+</sup>) are at the intracellular area. The unit, mEq/L, means the amount of a substance that will react with one mole of electrons.

ION	INTRACELLULAR	EXTRACELLULAR
Sodium (Na <sup>+</sup> )	10	142
Potassium (K <sup>+</sup> )	140	4
Calcium (Ca <sup>2+</sup> )	0.0001	2.4
Magnesium (Mg <sup>2+</sup> )	58	1.2
Chloride (Cl <sup>-</sup> )	4	103
Bicarbonate (HCO <sub>3</sub> <sup>-</sup> )	10	28
Sulfate (SO <sub>4</sub> <sup>-</sup> )	2	1

\*unit: mEq/L

directions across the cell membrane. In ionic movements, an ion channel provides the main routes for ions. Ion channels vary due to the nature of their gating, which can allow specific ions to pass through them, and the number of gates. Voltage-gated channels are opened and closed based on the membrane potential caused by the different concentrations of ions. A voltage-gated, also called voltage-dependent, ion channel is a governing and major type of ion channel. Ligand-gated channels are operated by the attachments or dissociation of some specific ligands, chemical messenger molecules, to the ion channels. A stress activated channel is another type of ion channel. It simply opens and closes in response to the mechanical deformation of a cell membrane.

As mentioned, the voltage-gated ion channels are dominant in the cell membrane, which indicates that the kinetics of voltage-gated ion channels is critical to affect the changes of membrane potential [62]. In addition to the voltage-gated ion channel, the  $\text{Na}^+/\text{K}^+$  pump plays an important role in maintaining the resting membrane potential by the repeated exchanges of  $\text{Na}^+$  and  $\text{K}^+$ .

### **2.3.1 VOLTAGE-GATED $\text{Na}^+$ CHANNEL**

A voltage-gated  $\text{Na}^+$  channel is a membrane protein composed of four  $\alpha$ -subunits and several associated  $\beta$ -subunits. The four  $\alpha$ -subunits construct a structural main core, which is the pathway for  $\text{Na}^+$  ions [28]. In turn, an  $\alpha$ -subunit consists of four homologous domains with six helical regions. Each domain has a tetrodotoxin (TTX) binding site, which selectively controls fast acting  $\text{Na}^+$  channels. Voltage-gated  $\text{Na}^+$  channels are critical in the generation and propagation of action potentials [93]. The probability of open  $\text{Na}^+$  channels increases dramatically during depolarization and then rapidly

decreases. The open  $\text{Na}^+$  channels allow only  $\text{Na}^+$  ions and result in a high  $\text{Na}^+$  concentration inside the cell membrane. The area occupied by  $\text{Na}^+$  channels on the total surface is very small, but each channel can pass many ions -- approximately  $10^7$  ions in a second [23]. Therefore, a channel carries a significant number of ions through it during depolarization.

### **2.3.2 VOLTAGE-GATED $\text{K}^+$ CHANNEL**

A voltage-gated  $\text{K}^+$  channel is another membrane protein to provide a specialized path for  $\text{K}^+$  through the cell membrane. A  $\text{K}^+$  channel is composed of four monomeric  $\alpha$ -subunits, which surround the structural pore. Each  $\alpha$ -subunit is associated with a  $\beta$ -subunit, and these  $\beta$ -subunits control the function of channels. Due to the relatively longer response time to a triggering potential, the conductance by voltage-gated  $\text{K}^+$  channels is tightly connected to the membrane potential. Notably, the repolarization in the action potential is mainly governed by the dynamics of voltage-gated  $\text{K}^+$  channels. While the action potential rapidly increases, the conductance of the  $\text{K}^+$  channel increases slowly. Even after the action potential reaches its peak, the increasing conductance still remains for a short time. This leads to slow repolarization in the action potential.

### **2.3.3 $\text{Na}^+/\text{K}^+$ ADENOSINE TRIPHOSPHATASE**

$\text{Na}^+/\text{K}^+$  ATPase, also called a  $\text{Na}^+/\text{K}^+$  pump or simply  $\text{Na}^+$  pump, is an enzyme<sup>2</sup> that controls an active transport of ions through the cell membrane. The  $\text{Na}^+/\text{K}^+$  pump is composed of  $\alpha$ -subunits and  $\beta$ -subunits [52]. The  $\alpha$ -subunit consists of specific binding

---

<sup>2</sup> A protein that helps to increase the rates of chemical reactions



sites of  $\text{Na}^+$ ,  $\text{K}^+$ , and  $\text{ATP}^3$ ; these sites are exposed to extracellular space for  $\text{K}^+$  and to intracellular space for  $\text{Na}^+$  and  $\text{ATP}$  during the active ionic transportation [5]. The  $\beta$ -subunit is a special component in providing the routes for  $\alpha$ -subunits in membrane and attaching sites for  $\text{K}^+$  ions [52].

The negative gradient of an intracellular action potential is not a stable state. Rather, it is better referred to as the steady state. For maintaining this state, an active transport is required, and the  $\text{Na}^+/\text{K}^+$  pump plays the main role in establishing the membrane gradient. In skeletal muscles, the  $\text{Na}^+/\text{K}^+$  pump controls the balance of  $\text{Na}^+$  and  $\text{K}^+$  across the cell membrane and also in many other cell types, such as the cells in the kidney, blood vessels, and the heart [51]. During the typical steady state of an excitable cell,  $\text{K}^+$  has higher concentrations than  $\text{Na}^+$  inside the cell by the active transport of the  $\text{Na}^+/\text{K}^+$  pump. Transportation starts with the  $\text{Na}^+$  binding to the pump from within the intracellular space. A phosphorylation<sup>4</sup> by  $\text{ATP}$  binds to the pump and causes it to open to the extracellular space. During its outward opening, 3  $\text{Na}^+$  ions are released and 2  $\text{K}^+$  ions are attached to the pump. The deformation of phosphorylation switches the pump opening to intracellular space, and the 2 attached  $\text{K}^+$  are finally released into the cell membrane. As shown in the pumping process, this transportation requires  $\text{ATPs}$ . Therefore, it is called an active transport.

## 2.4 ACTION POTENTIAL TRANSMISSION

The initial neural signal generated in the brain is sent to a muscle fiber through serial or parallel connected neurons. Muscle fibers are functionally arranged into a motor unit

---

<sup>3</sup> Adenosine Triphosphate, used as metabolic energy for the intracellular active transfer

<sup>4</sup> A combination of a phosphate group and a protein or other molecule

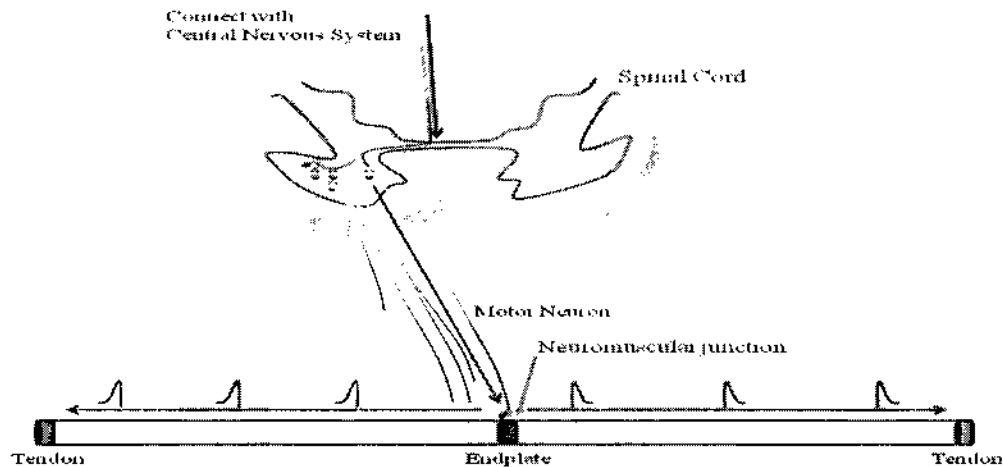


FIG. 9: Typical Path of Neural Stimulus from the brain to the tendon. Neuron and muscle fiber is connected at a neuromuscular junction and action potential flow follows the surface of the muscle fiber by self-propagation.

(MU). Each MU has one motor neuron axon and tens or hundreds of muscle fibers, which the neuron axon innervates. There is a special connective junction called the neuromuscular junction (NJ) where each muscle fiber is connected with the single axon through the motor end plate with a structural space called the synaptic cleft. Due to the connecting property, all muscle fibers in a MU are stimulated simultaneously.

The NJ provides the communication link between the motor neuron axon and muscle fibers. A motor neuron contains acetylcholine vesicles at its end, and each vesicle holds many neurotransmitters called acetylcholines (ACh). The signal from the nervous system stimulates the vesicles to release AChs into the NJ. The AChs bind to the ACh receptors, which are located at the motor end plate. It triggers the sodium ( $\text{Na}^+$ ) and potassium ( $\text{K}^+$ ) ion channels to open and allow ionic flow through the cell membrane. From the motor

end plate, the neural stimuli from the brain and nervous system flow following the surface of muscle fibers. This electrical potential also flows into the T tubule, the invaginated area of the sarcolemma<sup>5</sup>, and stimulates the inner contraction process. Finally, the traveling action potential dissipates in the tendon.

---

<sup>5</sup> The plasma membrane of the muscle cell

## CHAPTER 3

### MATHEMATICAL BACKGROUND

Many measured biological data are typically optimized with specially designed functions to reproduce the same or similar experimental results. Through optimizations, many benefits in times and costs can be actualized, and more modified optimization methods are developed for those advantages.

#### 3.1 GAMMA PROBABILITY DENSITY FUNCTION

A gamma probability density function (PDF) has been widely used because of its practical features in expressing an empirical result. Originally, a gamma PDF was applied to design the dye-dilution curve of blood flow [86]. The main reason to adopt a gamma PDF was its mathematical convenience and easy applicability to various dilution curves [40]. Based on the curve-fitting on a variety of dilution curves, 114 normal and abnormal curves, a gamma PDF was suggested as a good characterization for normal curves as well as a theoretical analysis of a typical dilution curve [40]. Because of the empirical applications by a gamma PDF [64], it also has been applied for designing an intracellular action potential (IAP) model [75,89,95]. Although these IAP models shown in the previous studies failed to represent a precise IAP model [60], these studies suggested a roughly approximated prototype for IAP models by using a gamma PDF. A typical gamma PDF is given as follows:

$$g_{PDF}(x) = \frac{1}{\Gamma(k)\theta^k} x^{k-1} e^{-\frac{1}{\theta}x} \quad (3.1)$$

where  $\Gamma(k)$  is a gamma function. Two parameters,  $k$  and  $\theta$ , control the shape and the change rate of a gamma PDF. With a fixed value of  $\theta$ , the general shape of a gamma PDF is controlled by the parameter,  $k$ . The higher values in  $k$  with fixed  $\theta$  generate the narrower and delayed signals. Unlike  $k$ ,  $\theta$  produces a wider and delayed signal as it becomes smaller in the fixed  $k$ . These effects, also called gamma variates, were carefully examined by using normal and abnormal curves many decades ago [40,86].

In this dissertation, a modified gamma PDF is used by simple replacements as follows:

$$g_M(x) = \gamma x^\alpha e^{-\beta x} \quad (3.2)$$

where  $(k-1)$  is replaced by  $\alpha$ , and  $\frac{1}{\theta}$  is replaced by  $\beta$ . The amplitude component in the gamma PDF is replaced by  $\gamma$ . The skewness of a gamma PDF is very useful in explaining ionic flows at different rates [33]. The depolarization and repolarization by the movements of sodium ( $\text{Na}^+$ ) and potassium ( $\text{K}^+$ ) in the IAP result from fast  $\text{Na}^+$  ion flow into cells at the beginning of the IAP and slow  $\text{K}^+$  ion flow out of cells at the rest part of the IAP [33]. These different ionic flows can be modeled by using independently separate gamma PDFs. Due to the historical and physiological findings, a series of modified gamma PDFs can be an accurate and meaningful IAP model.

### 3.2 ERLANG PROBABILITY DENSITY FUNCTION

The Erlang probability density function (PDF) is a special form of a gamma PDF. In a gamma PDF, two parameters,  $k$  and  $\theta$ , are non-integers in equation 3.1. However,  $k$ , the shape parameter, is forced to be integers in the Erlang PDF. As an example, the Erlang

PDF was used for the analytical solution for a compartmental chain [96]. The integer values in  $k$ ,  $\alpha$  in the modified gamma PDF, help to explain the relation between  $\alpha$  and the number of ion channel states. The state of ion channel means the current form of the ion channel. By changing its form, ion channels provide paths for specific ions. Each formation of the ion channel is assumed to be stable, continuing for several milliseconds [102]. Based on this assumption, ion channel formation at each state can be independent and stable. Currently, this kind of assumption is required for ion channel models because of the lack of visual data of transmembrane proteins, which are the structural units of ion channels. By using the Erlang PDF, the assumable total states of ion channels will be explained by means of numerical values.

### **3.3 NUMERICAL OPTIMIZATION**

Numerical optimization is often used to represent various biological data [20,56,66,101]. Optimization mainly finds the minimum or maximum of an objective function that contains important values to designate critical changes in the measured data. Depending upon the limitations of the final solutions, optimization can be divided into two types: unconstrained and constrained optimizations. As implied by their names, unconstrained optimization has no boundary or initial restrictions in the core variables of a given objective function while constrained optimization does. Generally, the ranges for the variables in the given objective functions are not specifically defined. Notably, the dynamic models for ion channels are still vague because of their size limitations and structural complications [2,3,61,62]. Therefore, many models for the physiological

dynamics or kinetics of ion channels require the approaches of unconstrained optimization methods.

In general, the physiological changes are non-linear and the final model is not stable in optimization [6]. In particular, the uniqueness of obtained solutions is one of the most challenging processes in an “inverse problem” [6]. These difficulties may be decreased by using several different methods in numerical optimizations. In this study, three numerical methods will be applied to generate an intracellular action potential (IAP) model: Newton method, Steepest Descent method, and Conjugate Gradient Method. In addition, the Levenberg-Marquardt algorithm will be used to support finding a numerical solution in the Gauss-Newton method.

### **3.3.1 OBJECTIVE FUNCTION**

An objective function is a mathematical equation for the evaluation of its fitness to experimental results in a typical optimization technique [48]. An objective function generally contains multiple criteria which control functional dynamics [55,70]. Eventually, the functional dynamics are expressed as the important characteristics underlying the measured data. Therefore, the creation of an objective function is the most important process which one must accomplish in optimization.

In constructing an objective function, several critical aspects should be deliberated. First, the variables in an objective function should represent meaningful criteria to explain the dynamics underlying the experimental data [48]. Theoretically, many optimization problems can be solved by using different equations and variables. For example, the intracellular action potential (IAP) has been modeled with different

equations and variables. Rosenfalck and Nandedkar [75,89,95] suggested a modified gamma distribution function as an IAP model and Dimitrov and Dimitrova (D-D) [37,57,58] created the summation of three independent analytical expressions that were composed of a modified gamma distribution function and a polynomial function. The most recent IAP model was generated based on the multiplication of a modified gamma distribution function and a more lengthened polynomial function by D-D [98,99]. However, no IAP model successfully denoted the meanings of variables, and all IAP models were simply empirical adjustments. Due to the theoretically weak approximation, most IAP models are often criticized for their modeling origins and replaced by other alternatives. Therefore, all values in an objective function are required to be used as significant factors.

The second factor is the continuity of the objective function. As optimization algorithms require more sophisticated solutions, they need the higher order derivatives of an objective function [107]. For example, Newton methods in optimization use the Hessian matrix, the second derivatives of the objective function, but Gauss-Newton methods adopt the Jacobian matrix, the first derivative, for reducing complex computations. However, Newton methods may generate more accurate solutions than Gauss-Newton methods because of the loss of functional components. The continuity of an objective function is also linked to computational efficiency in optimization. Generally, the higher order continuous derivative of an objective function produces faster convergence of an optimization [107]. Therefore, any discontinuity is unacceptable in creating an objective function.



The third is functional efficiency. As shown in the examples of IAP modeling, an unlimited expansion of any function might generate the optimized shape to experimental data [98,99]. However, a meaningless long function can decrease the computational speed and also cause low credibility of a generated model [48].

The last considerable aspect in optimization is the solution uniqueness. Most optimization processes for nonlinear data require iterative methods to find solutions. However, the iterative process solutions contain unsolved local minimum points [7]. Due to computational limitations, it is tremendously difficult to satisfy all those local minimum points in one solution. The incomplete solutions often cause problems of uniqueness [7,44,48,109]. To improve and solve these problems, various approaches have been tried: (1) the adoption of alternative methods [7,48,109], (2) the combination of traditional optimization methods [48], and (3) computational modification of the optimization process [44]. However, computational modification is too complex to apply to general cases. Therefore, alternative methods and their combinations are widely used for the uniqueness of solutions.

### **3.3.2 GAUSS-NEWTON METHOD**

The Gauss-Newton method is a numerical optimization algorithm to find non-linear least square solutions. This method is a modified version of the Newton method, and it generally requires no second derivatives, called Hessians. In least square problems, the non-linear solutions can be found by iterative methods because of their computational limits. Most limitations are caused by the weak properties in convergence during the iterative process. Convergence limitations mainly result from choosing the wrong initial

variable values for the solutions, or the ill-conditioned multiplications of the first derivatives, called Jacobians, can also raise this kind of problem. Therefore, a modified Gauss-Newton method is used in this study by adding the second derivative component to overcome the computational limits. For the computation of the second derivatives, the Levenberg-Marquardt algorithm is introduced. This algorithm takes the advantages of both the Gauss-Newton and the gradient descent methods [41], but instead of directly computing the second derivatives, the Levenberg-Marquardt algorithm finds an approximate Hessian matrix to ensure the existence of its inversion.

$$\mathbf{H} = (\mathbf{J}^T \mathbf{W} \mathbf{J} + \mu \mathbf{I}) \quad (3.3)$$

where  $\mathbf{J}$  is the Jacobian matrix, and  $\mathbf{W}$  is the weighting matrix.  $\mathbf{I}$  is the identity matrix. By taking a low conditioning factor,  $\mu$ , the algorithm has properties similar to the Gauss-Newton method, and it operates like the gradient descent method with a high factor. The factor can be determined based on the previous and updated solutions. There is no specific value for the initial factor, but it starts with 0.5 in practice. For accurate computational results, the modified Hessian matrix is not used in this study. However, the essential idea to adapt two different optimization methods is applied by using equation 3.3.

With an initial guess,  $\beta_0$ , the Gauss-Newton method updates the set of solutions,  $\beta$ , in every iteration. The solution at  $n^{\text{th}}$  iteration is as follows:

$$\beta_n = \beta_{n-1} + \Delta\beta \quad (3.4)$$

where  $\beta_n$  is the solution after the  $n^{\text{th}}$  iteration, and  $\beta_{n-1}$  is the solution after the  $(n-1)^{\text{th}}$  iteration.  $\Delta\beta$  is the computed increment or decrement vector and is calculated as follows:

$$\Delta\beta = (\mathbf{J}^T\mathbf{J})^{-1}(-\mathbf{J}^T\mathbf{r}) \quad (3.5)$$

where  $\mathbf{r}$  is the residual matrix, which is the difference between the measured data and a given objective function.  $\mathbf{X}^T$  and  $\mathbf{X}^{-1}$  represent the transpose and inverse matrix of  $\mathbf{X}$ , respectively. However, the component of  $\mathbf{J}^T\mathbf{J}$  can be ill-conditioned, which means singular<sup>6</sup>. To avoid this computational problem, the Hessian matrix is added and applied to find the increment or decrement vector. The final equation is as follows:

$$\Delta\beta = \varepsilon \cdot (\mathbf{H} + \mu\mathbf{D})^{-1} \cdot \mathbf{J} \quad (3.6)$$

where  $\mathbf{H}$  is the Hessian matrix of the residual matrix.  $\mathbf{D}$  is the diagonal matrix of  $\mathbf{H}$ , and  $\mu$  is the Marquardt parameter.  $\varepsilon$  is the fractional parameter between 0 and 1 that controls the incremental size of the solution.

Before the next iteration, the newly computed solution is compared with the previous solution by using the sum of squared residuals (SSR). A typical SSR is as follows:

$$\text{SSR} = \sum_{i=1}^n (\mathbf{M}(i) - \mathbf{F}(i))^2 \quad (3.7)$$

where  $\mathbf{M}$  is the measured data, and  $\mathbf{F}$  is a modeled function with the number of  $n$ . SSR generally measures the discrepancy between the measured data and a modeled function. By finding the SSR, the tightness of a model to measured data can be estimated which is a very popular method in various areas [1,4,38]. The iteration in the modified Gauss-

---

<sup>6</sup> A matrix has no inversion.

Newton method continues until a preset condition, generally specific values in SSR, is satisfied [84].

### 3.3.3 STEEPEST DESCENT METHOD

The steepest descent method, also known as the gradient descent method, is used to find the minimums of nonlinear functions in engineering and the natural sciences [88]. This method is the simplest and easiest method of the gradient descent algorithms. This method has solutions, which are linearly converged, and it generally converges even with a poor initial guess for the solution [88]. A typical process in updating the solution is as follows:

$$\beta_{n+1} = \beta_n + \alpha_n \mathbf{J}_n \quad (3.8)$$

where  $\beta_{n+1}$  and  $\beta_n$  are the solutions after  $(n+1)^{\text{th}}$  and  $(n-1)^{\text{th}}$  iterations, respectively.  $\alpha$  is the step size or step length, and  $\mathbf{J}$  is the Jacobian matrix of a given objective function. Generally, the step size can be computed as follows:

$$\alpha_n = \arg \min f(\beta_n + \alpha \mathbf{J}_n) \quad (3.9)$$

where *arg min* means the argument of the minimum for the given objective function,  $f$ , and the  $\alpha$ , which satisfies the condition, is replaced by the previous value during the iteration process. There are many approaches for finding the step size under line-search rules [108]. In practice, however, the norm of the Jacobian matrix should be one for the accurate step size computation [18]. In particular, the given search method can cause unnecessary computation for the trajectory if the final solution is close to the current

point [18]. As in the Gauss-Newton method, the SSR is introduced in the iteration to evaluate the performance of the current solution by comparing it with the measured data. The iteration continues if terminating conditions are not met.

### 3.3.4 CONJUGATE GRADIENT METHOD

The Conjugate gradient method is another gradient descent method, and the iterative formula in the conjugate gradient method is slightly different from the steepest descent method. Instead of directly using the Jacobian matrix in computing the next solution, there is one step to find the search direction vector,  $\mathbf{S}$ .

The general iteration formula is as follows:

$$\boldsymbol{\beta}_{n+1} = \boldsymbol{\beta}_n + \alpha_n \mathbf{S}_n \quad (3.10)$$

where  $\boldsymbol{\beta}_{n+1}$  and  $\boldsymbol{\beta}_n$  are the solutions for the  $(n+1)^{\text{th}}$  and the  $n^{\text{th}}$  iterations, respectively.  $\alpha$  is the step size, and  $\mathbf{S}$  is the search direction vector. The vector is again calculated as follows:

$$\mathbf{S}_{n+1} = -\mathbf{J}_{n+1} + \delta_n \mathbf{S}_n \quad (3.11)$$

where  $\mathbf{S}_{n+1}$  and  $\mathbf{S}_n$  are the direction vectors for the  $(n+1)^{\text{th}}$  and the  $n^{\text{th}}$  iterations.  $\mathbf{J}$  is the Jacobian matrix of the given objective function, and  $\delta$  is the conjugate gradient parameter. Generally, the conjugate gradient method has different versions depending on the computational method for its parameter,  $\delta$ : the Polak-Ribiere (PR), the Fletcher-Reeves (FR), Hestenes-Stiefel (HS), and Dai-Yuan (DY) methods [49,73,79,106]. The computational formulas for each version is as follows:

$$\text{PR: } \delta_n = \frac{\mathbf{J}_n^T \mathbf{d}_{n-1}}{\|\mathbf{J}_{n-1}\|^2} \quad (3.12)$$

$$\text{FR: } \delta_n = \frac{\|\mathbf{J}_n\|^2}{\|\mathbf{J}_{n-1}\|^2} \quad (3.13)$$

$$\text{HS: } \delta_n = \frac{\mathbf{J}_n^T \mathbf{d}_{n-1}}{\mathbf{S}_{n-1}^T \mathbf{d}_{n-1}} \quad (3.14)$$

$$\text{DY: } \delta_n = \frac{\|\mathbf{J}_n\|^2}{\mathbf{S}_{n-1}^T \mathbf{d}_{n-1}} \quad (3.15)$$

where  $\mathbf{d}_{n-1}$  is the difference between two successive Jacobian matrixes,  $\mathbf{J}_n$  and  $\mathbf{J}_{n-1}$ . Depending on the convexness or the concaveness of the given objective function, these versions produce different results. However, the classified versions are meaningless if the given objective function has both convexness and concaveness at the same time [49]. In many cases, PR and HS are often used because of the component,  $\mathbf{S}_{n-1}^T \mathbf{d}_{n-1}$ , in the formula, which is considered to increase the efficiency of the conjugate gradient method [49]. Notably, PR and HS can restart the optimization process from the beginning if an ill direction vector is produced [49,104]. In addition, PR can update to various directions by the first derivative computation. Like other optimization methods, the conjugate gradient method also uses an iteration process to find solutions. The SSR is also used to decide the termination of the process by comparing a preset condition.

## CHAPTER 4

### INTRACELLULAR ACTION POTENTIAL MODELING

Intracellular action potentials (IAPs) in neuron and muscle have similar characteristics in the generating mechanisms but different shapes. The different IAPs require a different number of ion types to model the IAP in neuron and muscle. Therefore, a different number of involving components should be applied in IAP modeling.

#### 4.1 NEURON INTRACELLULAR ACTION POTENTIAL

For a reference, a measured neuron intracellular action potential (IAP) was obtained by digitizing the original data in a published journal paper [11]. The obtained IAP was measured from the hindmost nerve cells of *Loligo*<sup>7</sup>, which have giant axons with a diameter range between 400 and 800  $\mu\text{m}$  [10]. The sampled axons were tested to determine whether their membranes could generate an action potential after removing axoplasm *in vitro*<sup>8</sup>. With a short rectangular step voltage through one inserted electrode, the potential difference was recorded [10]. The potential difference to the applied short shock was compared with a computational value, which was controlled by the connected capacitor to the inserted electrode and the exposed total membrane area to the current flow.

##### 4.1.1 DATA PREPARATION

The digitized IAP was obtained by using Desktop Ruler (version 1.45). The measured IAP was displayed on a computer screen, and the time and the potential amplitude were

---

<sup>7</sup> A genus of squids

<sup>8</sup> Terminology for a procedure in a controlled environment

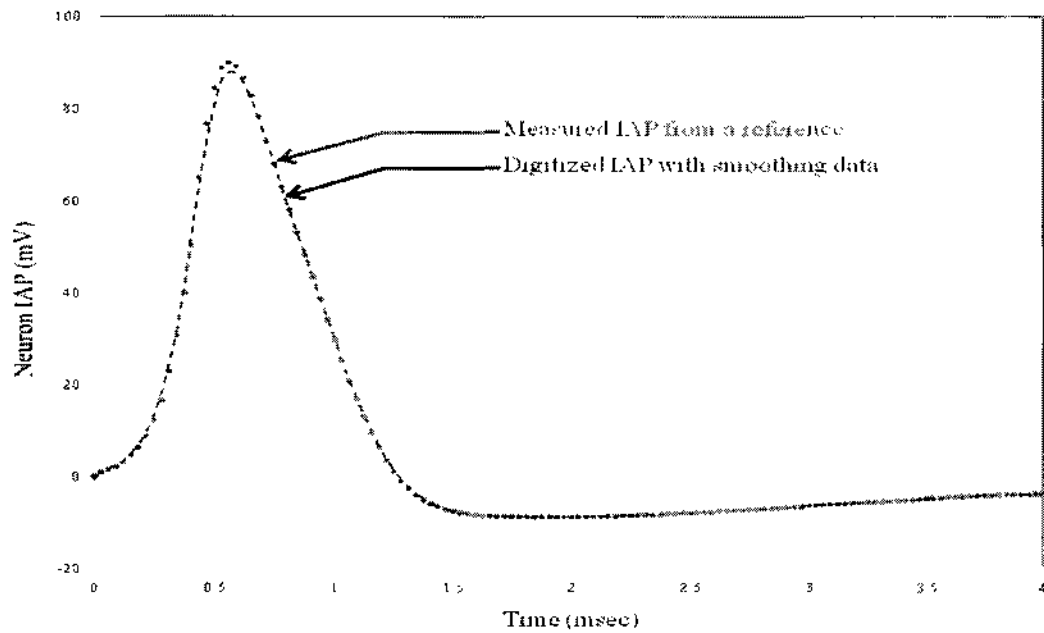


FIG. 10: The measured neuron IAP [11] in dots and its digitized IAP in dashes. After smoothing the data, the digitized IAP has a 2.5 % smaller value in the highest amplitude. The general neuron IAP initially has a negative value, approximately  $-60 \sim -65$  mV [12], but the neuron IAP in the reference [100] was adjusted to zero (0) by removing the initial amplitude.

recorded manually by Desktop Ruler. Several noticeable points, the zero and the highest amplitude, were selected and converted to the matched potential values. These points were used as references to decide other measured potential amplitudes from the digitized values. All potential amplitudes were calculated based on comparisons with point references. These manual recordings of the digitized potential amplitudes resulted in jagged lines that could cause computational difficulties in optimization. Therefore, to reduce possible computational complications, the recorded digitized values were smoothed in Matlab (version 7.8). The data smoothing was performed using Matlab defaults, the moving average method with span 5. There was an approximately 2.5 % loss



in the highest amplitude due to the smoothing procedure. This amount of error can be acceptable because it could happen even between two measured data [105]. Therefore, the small loss in the highest amplitude by smoothing was acceptable in this study.

#### 4.1.2 CONSTRUCTION OF OBJECTIVE FUNCTION

The objective function for the neuron IAP was constructed with two modified functions, modified Gamma and modified Erlang probability distribution functions (PDF). As emphasized in the Hodgkin and Huxley experiments [11], the most influent ions in generating the neuron IAP are sodium ( $\text{Na}^+$ ) and potassium ( $\text{K}^+$ ). In addition to these ions, there is another important ion, chloride ( $\text{Cl}^-$ ), which plays a critical role in the repolarization from the hyperpolarization. The small influences by other ions, such as A-type potassium ( $\text{K(A)}^+$ ), high-voltage activated calcium ( $\text{Ca}^{2+}$ ), calcium-dependent potassium ( $\text{K(Ca)}^+$ ) and persistent sodium (NaP), were combined into the leakage as Hodgkin and Huxley proposed in their studies [11-14]. Therefore, there were four independent Gamma PDFs or four independent Erlang PDFs in the objective function for a neuron IAP as follows:

$$F_{\text{NeuronIAP}}(t) = \sum_{i=1}^4 \gamma_i t^{\alpha_i} e^{-\beta_i t} \quad (4.1)$$

where  $t$  is time in msec. In the Gamma PDF,  $\alpha$  is any real number, but it is limited to an integer in the Erlang PDF. Each Gamma or Erlang PDF represents the ionic conductance for the main ions, such as  $\text{Na}^+$ ,  $\text{K}^+$ ,  $\text{Cl}^-$  and leakage, in time. The unknown parameters,  $\alpha$ ,  $\beta$ , and  $\gamma$ , were assigned for shape, rate, and adjusted amplitude, respectively. The parameter characteristics were determined by the properties of general Gamma and

Erlang PDFs. The separated parameter characteristics are useful in expressing the skewed IAP shape, which is controlled by the combined movements of  $\text{Na}^+$  and  $\text{K}^+$  ions.

Of the unknown parameters, the values in  $\alpha$  were assumed as indicators to match with the number of ion channel states. Due to the relationship between ion channel states and channel structural complexity, the higher value in  $\alpha$  implies the more complicated structural characteristics. Therefore, the highest  $\alpha$  represents the number of  $\text{Na}^+$  channel states and the second highest  $\alpha$  shows the  $\text{K}^+$  channel states. Based on this hypothesis, the lowest values in  $\alpha$  suggests the number of leakage channel states.

### 4.1.3 OPTIMIZATION IN GAUSS-NEWTON METHOD

The digitized IAP from reference [11] was assigned as the desired (target) signal for optimization. The Gauss-Newton method requires an initial guess for the estimated parameters. In determining the initial guess, the ionic conductance changes for each main ion were considered. For example,  $\text{Na}^+$  conductance rapidly increases at the beginning of IAP and drops before  $\text{K}^+$  conductance reaches its peak value in the time domain. Unlike  $\text{Na}^+$  conductance,  $\text{K}^+$  conductance increases relatively slowly at the beginning of IAP dynamics and decreases while IAP repolarizes. By reflecting these specific conductance changes, the initial values for the unknown parameters were determined. The initial parameters were the same for both objective functions with the Gamma PDF or the Erlang PDF, and they were empirically given as [2, 3, 5, 8, 0.3, 0.1, 0.5, 1.2, 1.6, -0.004, 0.1, -0.03] for  $[\alpha_1, \alpha_2, \alpha_3, \alpha_4, \beta_1, \beta_2, \beta_3, \beta_4, \gamma_1, \gamma_2, \gamma_3, \gamma_4]$ . To measure the difference between the desired and optimized IAPs, the residue was calculated, and the sum square of residue (SSR) was computed in each iteration as follows:

$$residue(n) = V_{des}(n) - V_{opt}(n) \quad (4.2)$$

$$ssr = \sum_{i=1}^n residue(i) \quad (4.3)$$

where  $V_{des}$  and  $V_{opt}$  are the desired and the optimized IAP, respectively, and  $n$  is the number of digitized values from the reference. An iterative process continues until a newly computed SSR is the same as the previous SSR.

In the Gauss-Newton method, the Jacobian matrix is required to update the unknown parameters, and the Hessian matrix was added for a better solution in the inverse computation of parameter vector,  $[\alpha_1, \alpha_2, \alpha_3, \alpha_4, \beta_1, \beta_2, \beta_3, \beta_4, \gamma_1, \gamma_2, \gamma_3, \gamma_4]$ . The Jacobian and Hessian matrices were calculated as follows:

$$J_r = \begin{bmatrix} \frac{\partial r(1)}{\partial \alpha_1} & \frac{\partial r(1)}{\partial \alpha_2} & \frac{\partial r(1)}{\partial \alpha_3} & \frac{\partial r(1)}{\partial \alpha_4} & \frac{\partial r(1)}{\partial \beta_1} & \frac{\partial r(1)}{\partial \beta_2} & \dots & \frac{\partial r(1)}{\partial \gamma_3} & \frac{\partial r(1)}{\partial \gamma_4} \\ \frac{\partial r(2)}{\partial \alpha_1} & \frac{\partial r(2)}{\partial \alpha_2} & \frac{\partial r(2)}{\partial \alpha_3} & \frac{\partial r(2)}{\partial \alpha_4} & \frac{\partial r(2)}{\partial \beta_1} & \frac{\partial r(2)}{\partial \beta_2} & \dots & \frac{\partial r(2)}{\partial \gamma_3} & \frac{\partial r(2)}{\partial \gamma_4} \\ \vdots & \vdots & \vdots & \vdots & \vdots & \vdots & \dots & \vdots & \vdots \\ \frac{\partial r(n)}{\partial \alpha_1} & \frac{\partial r(n)}{\partial \alpha_2} & \frac{\partial r(n)}{\partial \alpha_3} & \frac{\partial r(n)}{\partial \alpha_4} & \frac{\partial r(n)}{\partial \beta_1} & \frac{\partial r(n)}{\partial \beta_2} & \dots & \frac{\partial r(n)}{\partial \gamma_3} & \frac{\partial r(n)}{\partial \gamma_4} \end{bmatrix} \quad (4.4)$$

$$H = \begin{bmatrix} \frac{\partial^2 r(1)}{\partial \alpha_1^2} & \dots & \frac{\partial^2 r(1)}{\partial \alpha_1 \partial \gamma_4} & \frac{\partial^2 r(1)}{\partial \alpha_2 \partial \alpha_1} & \dots & \frac{\partial^2 r(1)}{\partial \alpha_2 \partial \gamma_4} & \frac{\partial^2 r(1)}{\partial \alpha_3 \partial \alpha_1} & \dots & \frac{\partial^2 r(1)}{\partial \gamma_3 \partial \gamma_4} & \frac{\partial^2 r(1)}{\partial \gamma_4^2} \\ \frac{\partial^2 r(2)}{\partial \alpha_1^2} & \dots & \frac{\partial^2 r(2)}{\partial \alpha_1 \partial \gamma_4} & \frac{\partial^2 r(2)}{\partial \alpha_2 \partial \alpha_1} & \dots & \frac{\partial^2 r(2)}{\partial \alpha_2 \partial \gamma_4} & \frac{\partial^2 r(2)}{\partial \alpha_3 \partial \alpha_1} & \dots & \frac{\partial^2 r(2)}{\partial \gamma_3 \partial \gamma_4} & \frac{\partial^2 r(2)}{\partial \gamma_4^2} \\ \vdots & \vdots & \vdots & \vdots & \vdots & \vdots & \vdots & \vdots & \vdots & \vdots \\ \frac{\partial^2 r(n)}{\partial \alpha_1^2} & \dots & \frac{\partial^2 r(n)}{\partial \alpha_1 \partial \gamma_4} & \frac{\partial^2 r(n)}{\partial \alpha_2 \partial \alpha_1} & \dots & \frac{\partial^2 r(n)}{\partial \alpha_2 \partial \gamma_4} & \frac{\partial^2 r(n)}{\partial \alpha_3 \partial \alpha_1} & \dots & \frac{\partial^2 r(n)}{\partial \gamma_3 \partial \gamma_4} & \frac{\partial^2 r(n)}{\partial \gamma_4^2} \end{bmatrix} \quad (4.5)$$

where  $r$  is residue. For implementing the Hessian matrix, a modified Hessian matrix was adopted as follows:

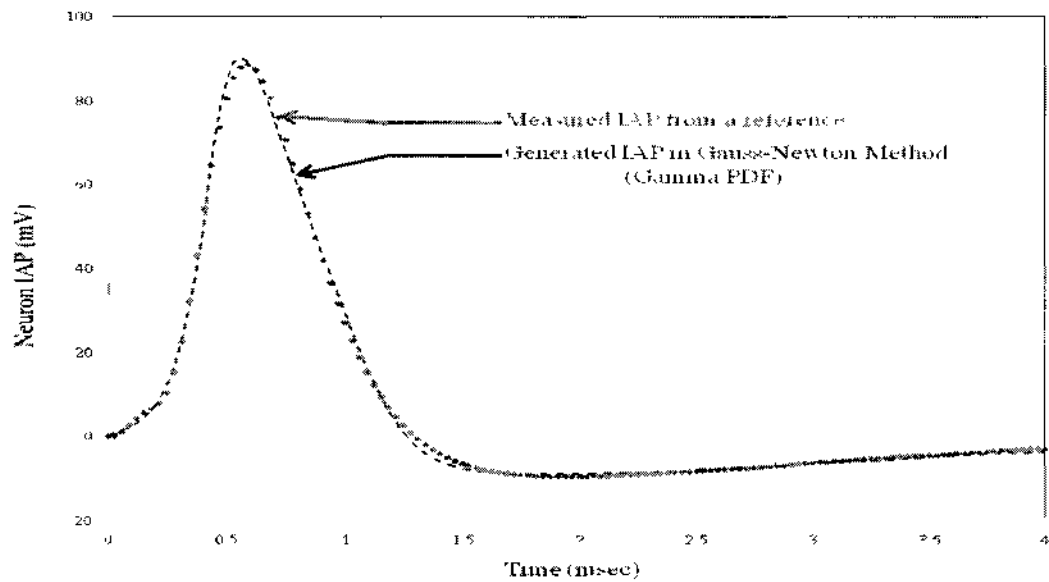


FIG. 11: The measured neuron IAP [11] in dots and the generated IAP in dashes. The IAP model was generated by using the Gauss-Newton method and its objective function was composed of four independent Gamma PDFs.

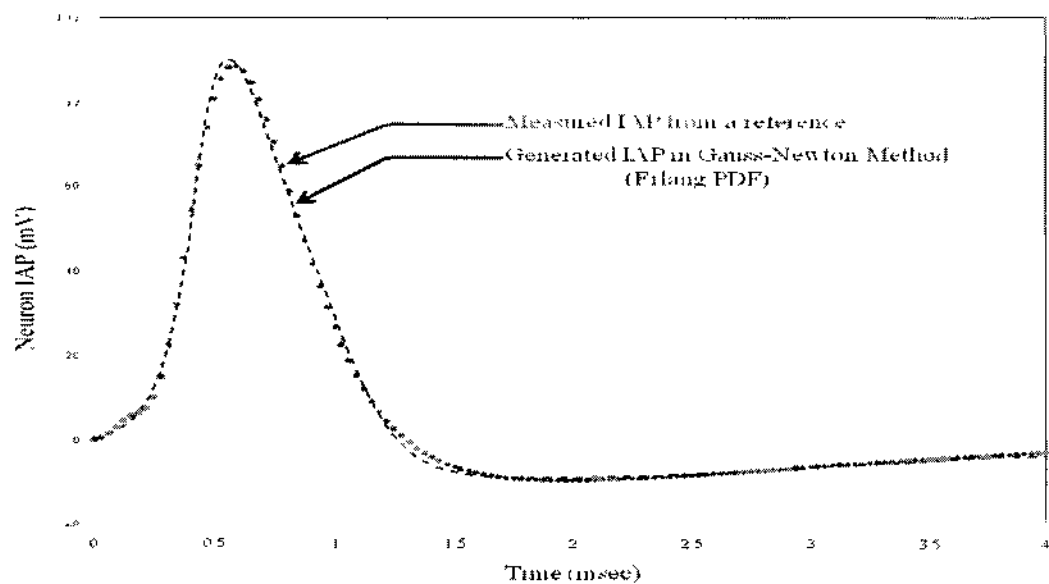


FIG. 12: The measured neuron IAP [11] in dots and the generated IAP in dashes. The IAP model was generated by using the Gauss-Newton method and its objective function was composed of four independent Erlang PDFs.

$$\mathbf{H}_{jk} = 2 \sum_{i=1}^n (r_i \frac{\partial^2 r_i}{\partial P_j \partial P_k} + \frac{\partial r_i}{\partial P_j} \frac{\partial r_i}{\partial P_k}) \quad (4.6)$$

where the indices,  $j$  and  $k$ , denote the corresponding parameters, and  $n$  is the number of digitized values from the reference.  $\mathbf{P}$  implies the parameter vector. After every iteration, the parameter vector was updated using equations (3.4) and (3.6) with a fractional parameter, 0.1, as shown in equation (4.7). Theoretically,  $\mu$  is a fractional parameter and a smaller value for  $\mu$  produces more accurate results. However, the longer time is necessary with the smaller  $\mu$ . In addition, there is a high chance that the process finally falls into a local minima and fails to find the better solution. Therefore,  $\mu$  should be determined as a trade-off point between computational time and accuracy. A newly computed parameter vector was compared with the previous parameter vector by computing a new residue. The new residue is again used for calculating a new SSR.

$$\Delta \mathbf{P} = 0.1 \times (\mathbf{H}_{jk} + \mu \mathbf{D}) \times \mathbf{J}_r \quad (4.7)$$

where  $\Delta \mathbf{P}$  is the increment or decrement of the parameter vector, and  $\mathbf{D}$  is the diagonal matrix of the Hessian matrix.  $\mu$  also represents the Marquardt parameter. Before the next iteration,  $\mu$  is updated based on the comparison between the previous and new SSR values. If the new SSR is smaller than the previous one,  $\mu$  is divided by a specific factor, which is generally  $\pi$  ( $\pi$ ), and it generates a new value for  $\mu$  for the next iteration. In the opposite case,  $\mu$  is multiplied by  $\pi$  ( $\pi$ ) for the next iteration. This is the core of the Levenberg-Marquardt algorithm, and its process is as follows:

$$\begin{aligned} \text{new } ssr < \text{previous } ssr: & \quad \text{new } \mu = \frac{\text{previous } \mu}{\pi} \\ \text{new } ssr \geq \text{previous } ssr: & \quad \text{new } \mu = \text{previous } \mu \times \pi \end{aligned} \quad (4.8)$$

Due to the limits in finding a complete zero (0) error solution, the iterative process was terminated when there were no additional decreases in newly computed SSR values. At the same time, any distorted results were also considered in deciding the end of an iteration. The zig-zag search for the global minimum sometimes causes a worse optimization result with a better SSR value. Therefore, the iterative process was stopped based on empirical evidence.

#### 4.1.4 OPTIMIZATION IN STEEPEST DESCENT METHOD

The optimization process in steepest descent method was similar to that in the Gauss-Newton methods except for the method to update the changes in the parameter vector. Unlike the Gauss-Newton methods, the second derivative matrix, the Hessian matrix, was excluded for finding the increment or decrement of the parameter vector. After computing the Jacobian matrix of the given objective function as equation (4.4), the changes in the parameter vector were calculated as follows:

$$\Delta \mathbf{P} = (oss \div \| \mathbf{g} \|) \times \mathbf{g} \quad (4.9)$$

where  $\mathbf{P}$  is the parameter vector,  $[\alpha_1, \alpha_2, \alpha_3, \alpha_4, \beta_1, \beta_2, \beta_3, \beta_4, \gamma_1, \gamma_2, \gamma_3, \gamma_4]$ , and  $oss$  is the optimal step size.  $\mathbf{g}$  is the multiplication of the Jacobian matrix and residue, and  $\| \mathbf{g} \|$  is the norm of  $\mathbf{g}$ . The  $\Delta \mathbf{P}$  was used to update the parameter vector and the newly computed parameter vector was applied for the next generated IAP model. By using SSR value, the tightness to the desired data was evaluated and the next iteration started if an obtained IAP model was not close enough to the measured IAP. As explained in the Gauss-Newton methods, the continuity of the iteration process depends on empirical experiences.

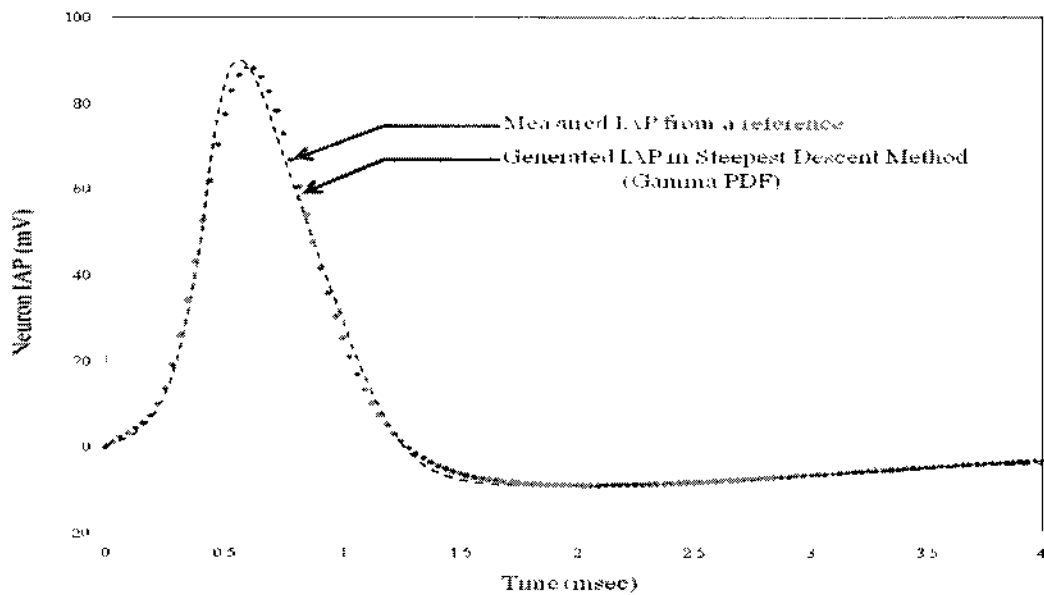


FIG. 13: The measured neuron IAP [11] in dots and the generated IAP in dashes. The IAP model was generated by using the Steepest Descent method and its objective function was composed of four independent Gamma PDFs.

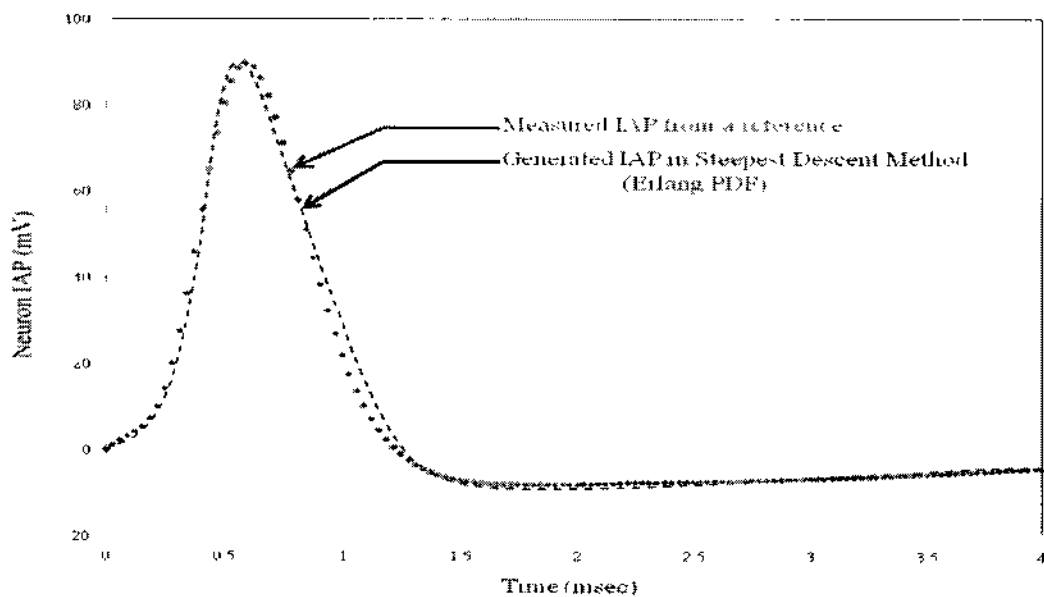


FIG. 14: The measured neuron IAP [11] in dots and the generated IAP in dashes. The IAP model was generated by using the Steepest Descent method and its objective function was composed of four independent Erlang PDFs.

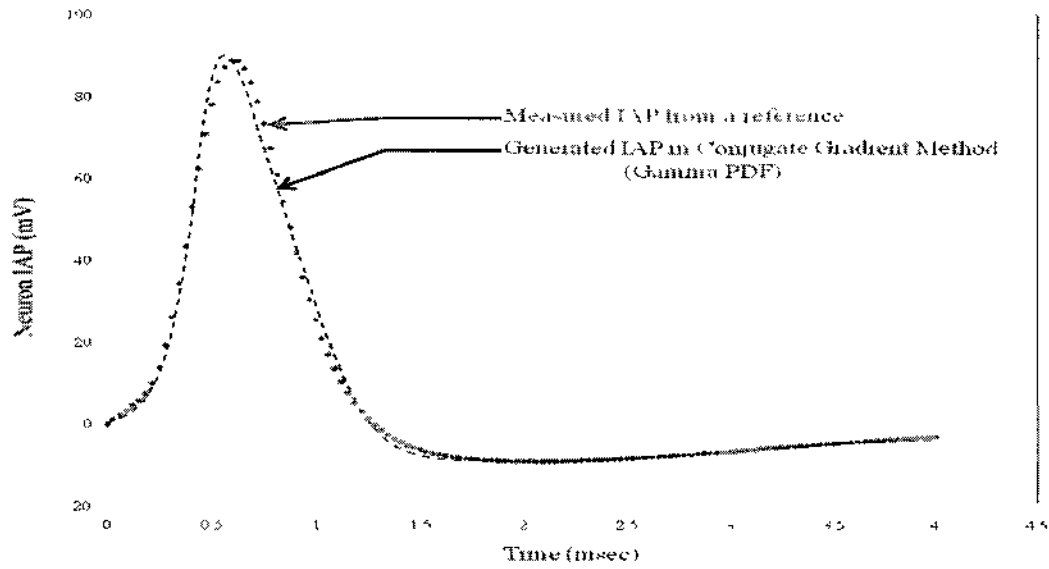


FIG. 15: The measured neuron IAP [11] in dots and the generated IAP in dashes. The IAP model was generated by using the Conjugate Gradient method and its objective function was composed of four independent Gamma PDFs.

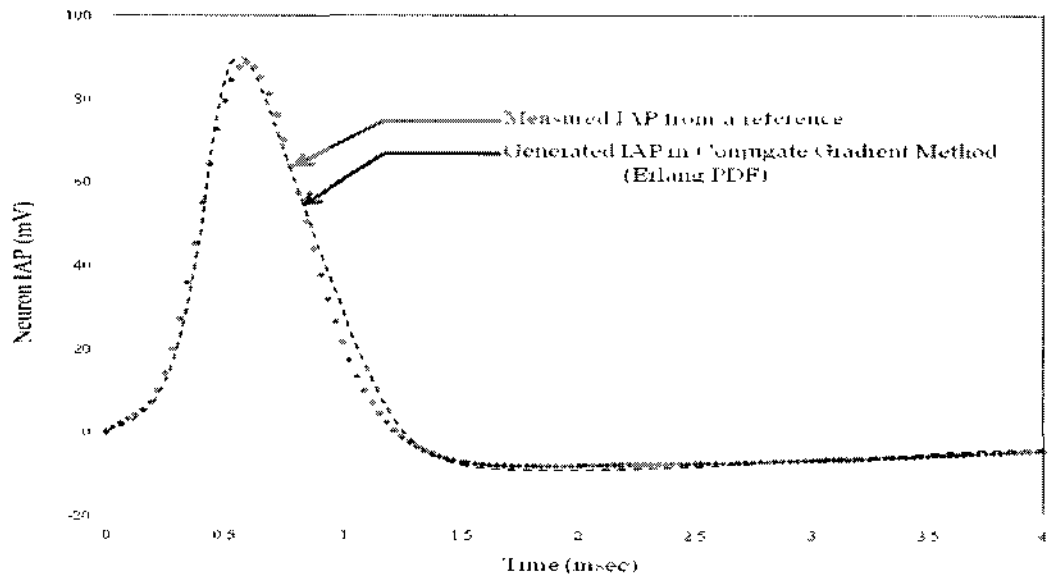


FIG. 16: The measured neuron IAP [11] in dots and the generated IAP in dashes. The IAP model was generated by using the Conjugate Gradient method and its objective function was composed of four independent Erlang PDFs.



TABLE 3: Summary of computed parameters,  $[\alpha_1, \alpha_2, \alpha_3, \alpha_4, \beta_1, \beta_2, \beta_3, \beta_4, \gamma_1, \gamma_2, \gamma_3, \gamma_4]$ , under different optimization methods such as the Gauss-Newton, the Steepest Descent, and the Conjugate Gradient with objective functions using the Gamma PDFs or the Erlang PDFs. The SSR for each case was the final value after iterations.

Parameter	Gauss-Newton		Steepest Descent		Conjugate Gradient	
	Initial	Final (G/E)	Initial	Final (G/E)	Initial	Final (G/E)
$\alpha_1$	2	2.39 / 2	1	1.04 / 1	1	1.04 / 1
$\alpha_2$	3	2.92 / 3	3	2.91 / 3	3	2.91 / 3
$\alpha_3$	5	4.99 / 5	6	6.13 / 6	6	6.13 / 6
$\alpha_4$	8	8.21 / 8	8	8.13 / 8	8	8.13 / 8
$\beta_1$	0.3	0.31 / 0.29	0.05	0.05 / 0.05	0.05	0.05 / 0.05
$\beta_2$	0.1	0.08 / 0.08	0.08	0.08 / 0.08	0.08	0.08 / 0.08
$\beta_3$	0.5	0.45 / 0.46	0.15	0.16 / 0.15	0.15	0.16 / 0.15
$\beta_4$	1.2	1.28 / 1.21	0.6	0.67 / 0.67	0.6	0.67 / 0.67
$\gamma_1$	1.6	0.93 / 1.34	1.9	1.98 / 1.98	1.9	1.98 / 1.98
$\gamma_2$	-0.004	-0.006 / -0.004	-0.015	-0.016 / -0.015	-0.015	-0.015 / -0.015
$\gamma_3$	0.1	0.08 / 0.08	0.1	3.4e-7 / 1.5e-6	0.1	3.4e-7 / 1.5e-6
$\gamma_4$	-0.03	-0.02 / -0.03	-0.004	4.1e-4 / 5.9e-4	-0.004	4.1e-4 / 5.9e-4
SSR	-	179.62 / 190.75	-	441.34 / 709.28	-	446.31 / 724.17

\*G/E = Gamma / Erlang

#### 4.1.5 OPTIMIZATION IN CONJUGATE GRADIENT METHOD

As with previous methods, the conjugate gradient method also involved the Jacobian matrix to update the parameter vector. Most of the process was similar to that of the steepest descent method except for the search direction parameter. Of several different approaches in computing the search direction parameter, the Polak-Ribiere (PR) method was used because of its efficiency with regards to the conjugate gradient method. The search direction parameter,  $\delta$ , in the PR method was as follows:

$$\delta = \frac{g_{new} \times g_{new}}{g_{old} \times g_{old}} \quad (4.10)$$

$$\Delta \mathbf{P} = \text{oss} \times (\mathbf{g}_{\text{new}} + \delta \times \Delta \mathbf{P}_{\text{old}}) \quad (4.11)$$

where  $\mathbf{g}_{\text{new}}$  is the multiplication of the current Jacobian matrix and current residue, and  $\mathbf{g}_{\text{old}}$  is that of the previous Jacobian matrix and previous residue.  $\text{oss}$  is the optimal step size and  $\Delta \mathbf{P}_{\text{old}}$  is the previous parameter vector. By using these computations, the parameter vector was updated in every iteration. The updated parameter vector was applied to the proposed objective vectors in the Gamma or the Erlang PDFs, and the newly generated IAP model was compared with the desired data by a residue. As in previous methods, the SSR value was computed in every iteration, and this was used to decide the continuity of the iteration process. If the SSR increased, the iteration was terminated, but the process kept running as long as the SSR continuously decreased.

Using my hypothesis, the highest value, 8, in  $\alpha$  is connected with the  $\text{Na}^+$  channel and the second highest value, 5, in  $\alpha$  is connected with the  $\text{K}^+$  channel. For the leakage, the assigned  $\alpha$  is 1.

## 4.2 MUSCLE FIBER INTRACELLULAR ACTION POTENTIAL

The reference for an intracellular action potential (IAP) in a muscle fiber was obtained from a published journal paper [17] as was also done for a neuron IAP. The muscle IAP was obtained in rat EDL<sup>9</sup> muscle in vivo [17].

### 4.2.1 DATA PREPARATION

The measured IAP was digitized using Desktop Ruler (version 1.45). Some points, such as the zero and the highest amplitudes, were utilized as references to decide other

---

<sup>9</sup> Extensor Digitorum Longus. A pinnate muscle located at the lateral part of the front of the leg.

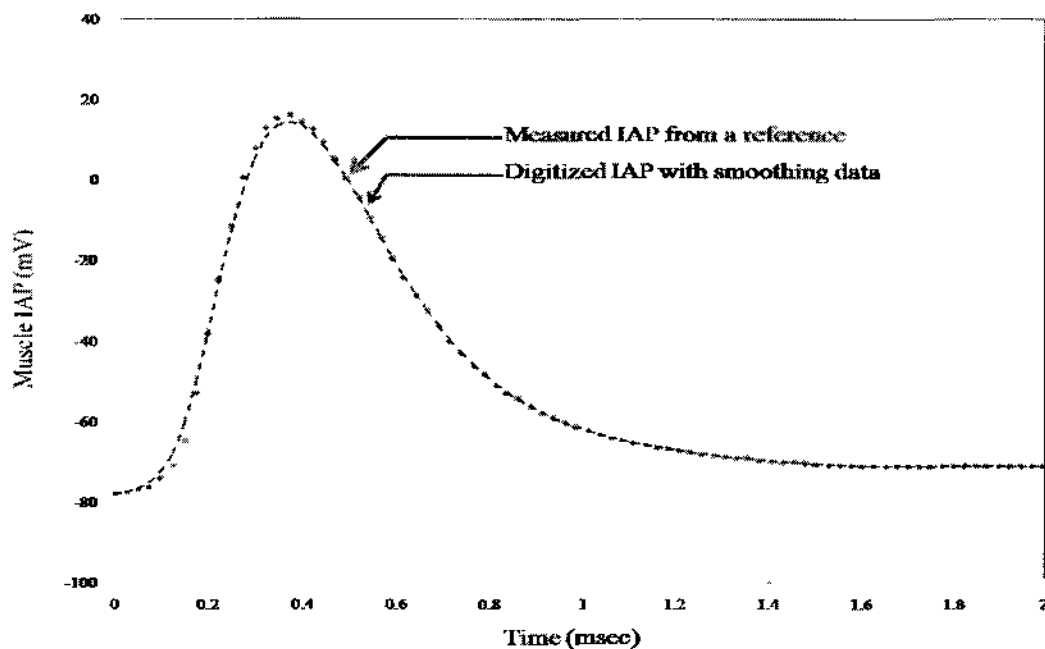


FIG. 17: The measured muscle IAP [17] in dots and its digitized IAP in dashes. After smoothing the data, the digitized IAP has a 1.95 % smaller value in the highest amplitude. General muscle IAP initially has a membrane potential and it is shown in the digitized muscle IAP.

measured potential amplitudes from the manually digitized values. All potential amplitudes were calculated based on the comparisons with point references. As was done in the neuron IAP data preparation, the digitized IAP was smoothed in Matlab with the moving average method by span 5. Due to the smoothing, there was approximately 1.95% loss in the highest amplitude. The reference IAP had an initial membrane potential of approximately -77.7 mV that was directly adopted in the digitized IAP. The initial membrane potential was generally removed in the computation of residue; therefore, there were no effects by the initial membrane potential.

### 4.2.2 CONSTRUCTION OF OBJECTIVE FUNCTION

Unlike the neuron IAP, muscle IAP is mainly governed by three ions, namely sodium ( $\text{Na}^+$ ), potassium ( $\text{K}^+$ ), and leakage. Therefore, the objective function has only three independent Gamma or Erlang PDFs as follows:

$$F_{\text{muscleIAP}}(t) = \sum_{i=1}^3 \gamma_i t^{\alpha_i} e^{-\beta_i t} \quad (4.12)$$

where  $t$  is time in msec. In the Gamma PDF,  $\alpha$  is any real number, and it is an integer in the Erlang PDF. Just like the objective functions in the neuron IAP, each Gamma or Erlang PDF represents the ionic conductance for the main ions in time. The unknown parameters,  $\alpha$ ,  $\beta$ , and  $\gamma$ , were assigned for shape, rate, and adjusted amplitude, respectively. In addition, the values in  $\alpha$  again play a role in signifying the number of ion channel states as done in the neuron IAP model. Based on the relationship between ion channel states and channel structural complexity, the higher value in  $\alpha$  implies the more complicated structural characteristics. Therefore, the highest  $\alpha$  represents the number of  $\text{Na}^+$  channel states, and the second highest  $\alpha$  shows the  $\text{K}^+$  channel states. Finally, the lowest values in  $\alpha$  correspond to the number of leakage states.

### 4.2.3 OPTIMIZATIONS IN THREE METHODS

Three optimization methods, the Gauss-Newton, the steepest descent, and the conjugate gradient methods, were applied to optimize a recorded IAP from muscle fiber as was done in the optimization of the neuron IAP. Even though the optimizing performance by the Gauss-Newton method in modeling a neuron IAP was the best based on the closeness to the reference data, all three methods were again applied to examine if there were any

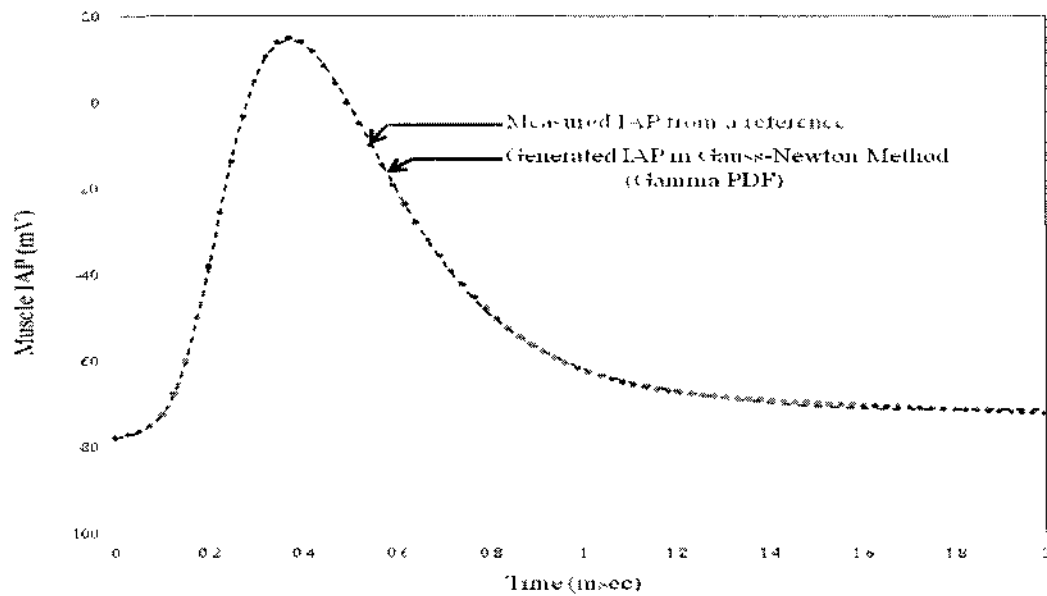


FIG. 18: The measured muscle IAP [17] in dots and the generated IAP in dashes. The IAP model was generated by using the Gauss-Newton method and its objective function was composed of three independent Gamma PDFs.

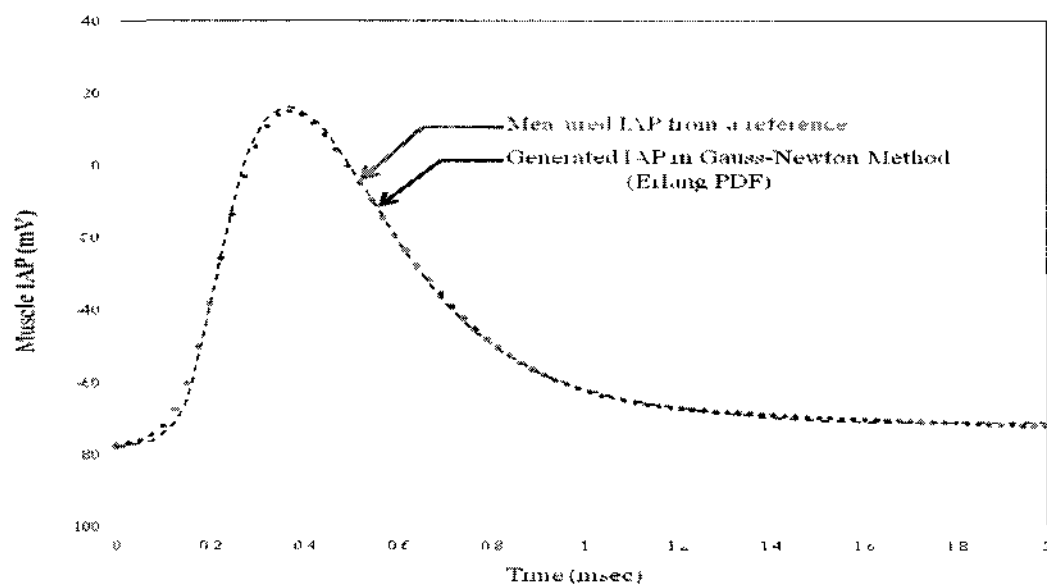


FIG. 19: The measured muscle IAP [17] in dots and the generated IAP in dashes. The IAP model was generated by using the Gauss-Newton method and its objective function was composed of three independent Erlang PDFs.

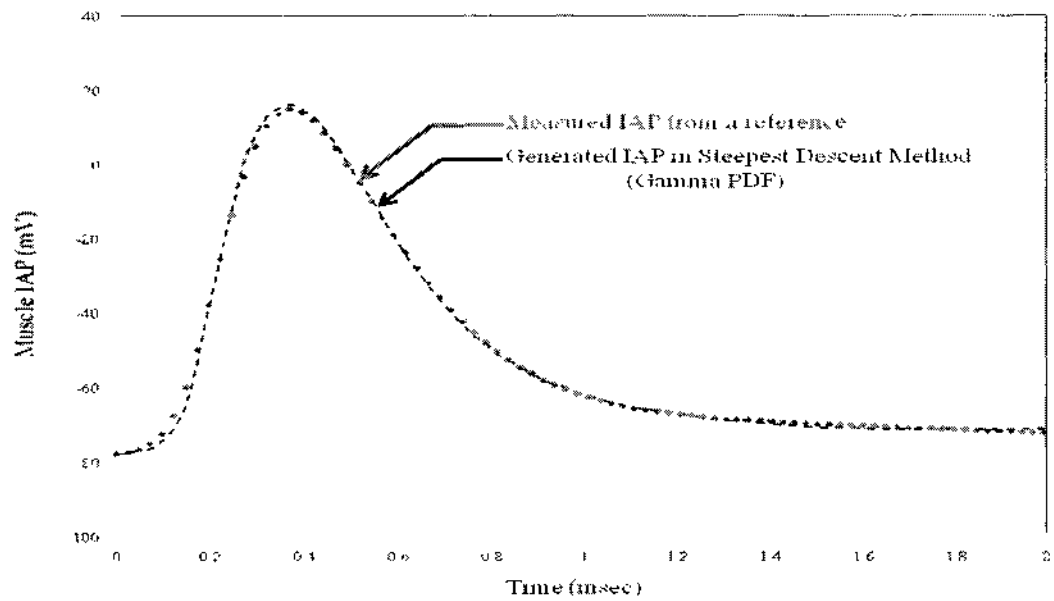


FIG. 20: The measured muscle IAP [17] in dots and the generated IAP in dashes. The IAP model was generated by using the Steepest Descent method and its objective function was composed of three independent Gamma PDFs.

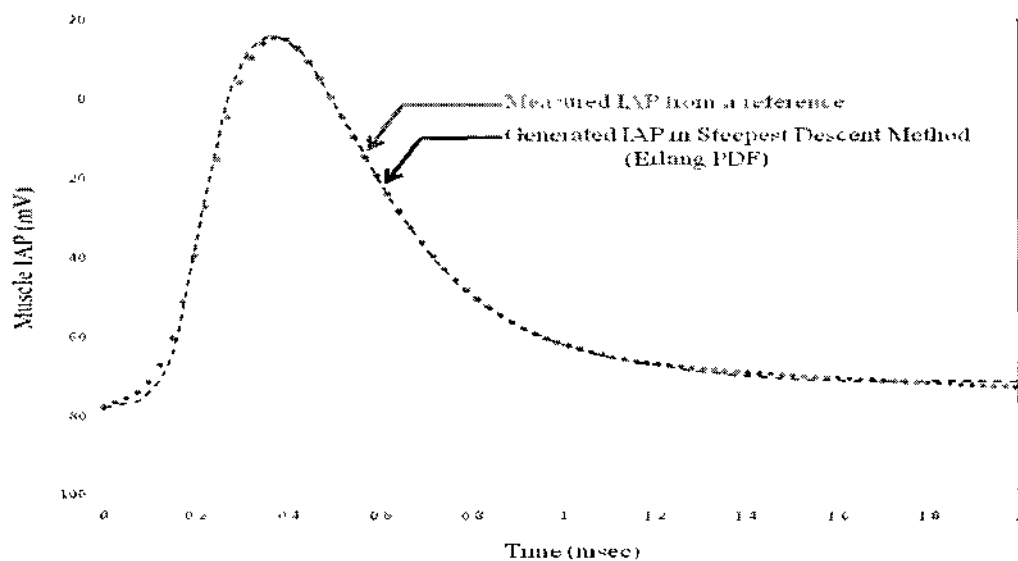


FIG. 21: The measured muscle IAP [17] in dots and the generated IAP in dashes. The IAP model was generated by using the Steepest Descent method and its objective function was composed of three independent Erlang PDFs.

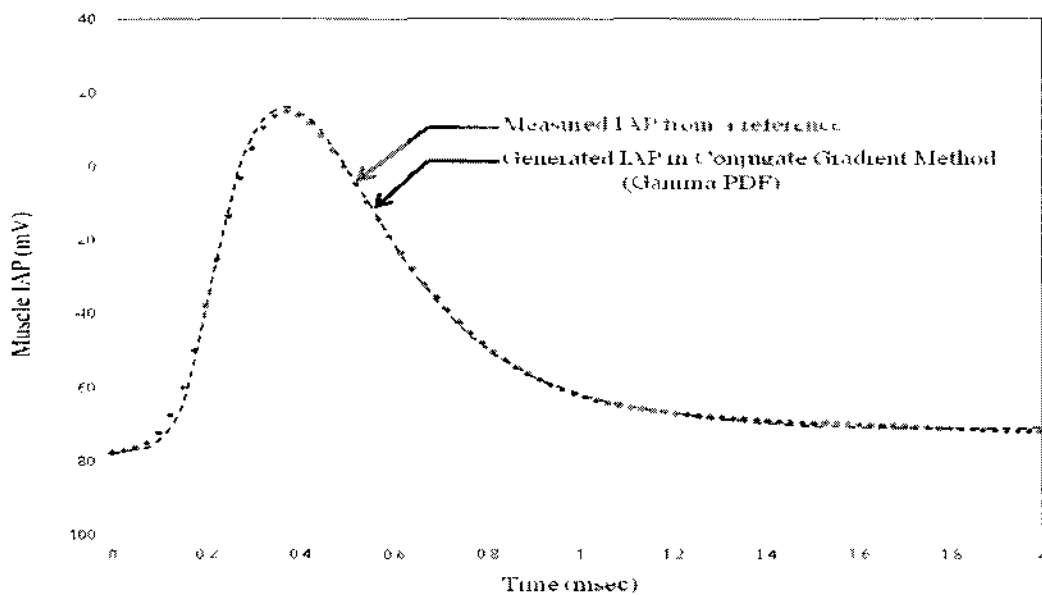


FIG. 22: The measured muscle IAP [17] in dots and the generated IAP in dashes. The IAP model was generated by using the Conjugate Gradient method and its objective function was composed of three independent Gamma PDFs.

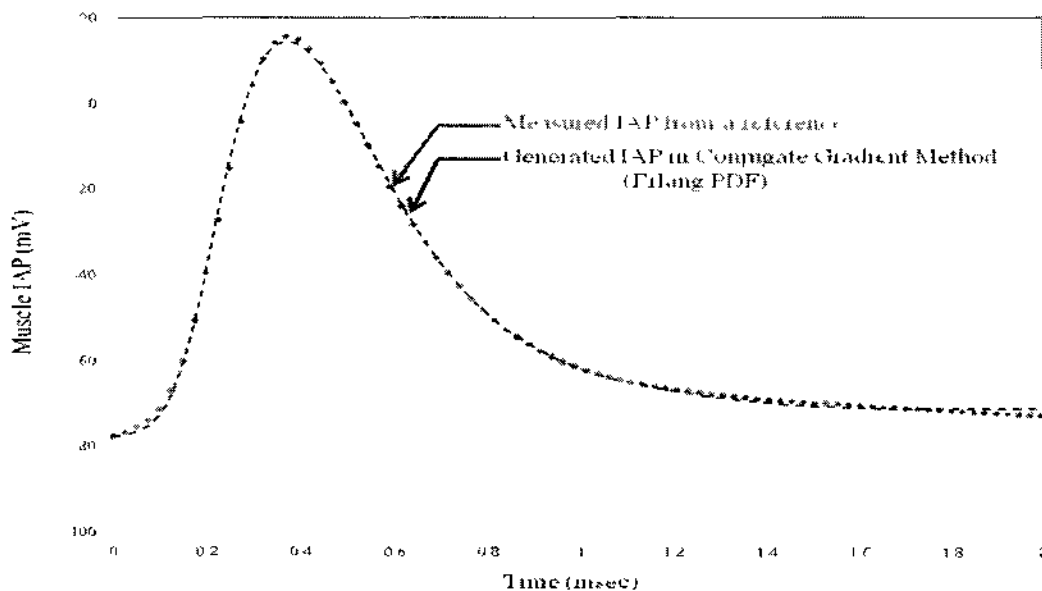


FIG. 23: The measured muscle IAP [17] in dots and the generated IAP in dashes. The IAP model was generated by using the Conjugate Gradient method and its objective function was composed of three independent Erlang PDFs.

TABLE 4: Summary of computed parameters,  $[\alpha_1, \alpha_2, \alpha_3, \beta_1, \beta_2, \beta_3, \gamma_1, \gamma_2, \gamma_3]$ , under different optimization methods, such as the Gauss-Newton, the Steepest Descent, and the Conjugate Gradient with objective function using the Gamma PDFs or the Erlang PDFs. All values under each optimization methods are the final with specific SSR.

Parameter	Initial	Gauss-Newton		Steepest Descent		Conjugate Gradient	
		Gamma	Erlang	Gamma	Erlang	Gamma	Erlang
$\alpha_1$	1	1.02	1	1.142	1	1.117	1
$\alpha_2$	5	4.95	5	4.712	5	4.775	5
$\alpha_3$	8	7.198	8	7.741	8	7.695	8
$\beta_1$	0.35	0.302	0.316	0.336	0.3696	0.335	0.374
$\beta_2$	3	2.818	2.924	2.803	2.9518	2.829	2.954
$\beta_3$	6	5.782	6.562	6.263	6.2497	6.238	6.252
$\gamma_1$	8	7.589	8.711	7.565	12.0237	7.873	12.328
$\gamma_2$	580	465.032	599.694	579.951	580.0019	579.989	580.605
$\gamma_3$	14000	10984	20373	14000	14000	14000	14000
SSR	-	13.3005	16.3538	14.8248	42.1556	14.8954	41.912

different results in the muscle IAP optimization. The desired (target) signal was digitized from a reference [17,105] and was treated by the same process as shown in the neuron IAP data preparation. By considering the ionic conductance changes for each main ion, an initial guess for the method was obtained. For instance, the rapid increase and decrease of  $\text{Na}^+$  conductance was considered, and the relative slow increase and decrease of the  $\text{K}^+$  conductance was applied in creating an initial guess. The initial values for the unknown parameters were the same for both objective functions, the Gamma PDF and the Erlang PDF, and they were empirically given as [1, 5, 8, 0.35, 3, 6, 8, 580, 14000] for  $[\alpha_1, \alpha_2, \alpha_3, \beta_1, \beta_2, \beta_3, \gamma_1, \gamma_2, \gamma_3]$ . Including the initial guess, the process was mostly the same as that in the neuron IAP optimization of the Gauss-Newton methods.

The optimization processes of the muscle IAP in the steepest descent and the conjugate gradient methods were also very similar to those in neuron IAP optimization.



Applying the same optimal step size, the processes were completed. In both methods, only the Jacobian matrix was used for updating the parameter vectors, and iteration was the main approach to find a final result for the parameters. Like the neuron IAP optimization, SSR values were used to show the tightness to the desired data, and the iterative process continued if an obtained SSR was smaller than the previous one. In the conjugate gradient method, the Polak-Ribiere (PR) method was used to find the search direction parameter because of its computational efficiency. Overall, the results of the Gauss-Newton method showed better performances with smaller SSRs in both neuron and muscle. Moreover, the objective function with the Gamma PDFs produced smaller SSRs than that with the Erlang PDFs.

Again, the highest value, 8, in  $\alpha$  is related to the  $\text{Na}^+$  channel and the second highest value, 5, in  $\alpha$  is connected with the  $\text{K}^+$  channel based on my hypothesis. For the leakage, the assigned  $\alpha$  is 1.

## CHAPTER 5

### MODEL VALIDATION & MODIFICATION

Validation is closely related to the credibility of a proposed computational model. Therefore, this process should be performed to ensure that the developed model accurately reproduces the estimated system dynamics. In addition, the muscle intracellular action potential (IAP) model was initially proposed because of the distorted performances by previous IAP models. Therefore, the proposed muscle IAP model is validated in this chapter. Due to limited funds and instruments, the indirect method is applied for model validation. All experimental resources are obtained from previous literature, and most processes in validation are similar to those of optimizations. Through the optimizations in the previous chapters, it was shown that the proposed IAP model had high credibility with specific values of parameters. However, those values were optimized to only one experimental result. By using comparisons with mode measuring data, the computed parameters in optimization can be evaluated if they are consistent in other experimental IAP dynamics.

#### 5.1 VALIDATION

Due to the experimental limitations in obtaining the exact numbers underlying the biological activities, it is common to design computational models for biological principles and processes. By using developed models, the biological behavior or dynamics are predicted and the obtained information is applied for medical treatments, research references, and various biological understandings. However, those models are easily criticized by reviewers who consider that all results from computational models are

inherently wrong [68]. To avoid the criticisms, a proposed computational model is required to be evaluated for accuracy by comparing it with real experimental data, so called validation. Validation is a process to determine how well the computational models accurately display or predict any given physical dynamics [39,43,68]. Through the process of validation, a simplified computational model is examined if it can predict or reproduce any fundamental experiment data for the more complicated system. Therefore, validation is closely dependent on resources or experimental results from the viewpoint of computational analysis [39].

Generally, there are two validation types: direct and indirect validations [8,39]. Direct validation conducts real experiments on the target subjects by controlling experimental components, such as experimental sources, measuring methods, detailed constituents, and accepted error ranges. Therefore, analysts or model designers can access and control every experimental step, and it helps to increase the fundamental confidence of a computational model in later comparison with an experimental result [9]. The performed experiments are designed to show the closeness to the simulated results. Therefore, the most significant properties and conditions are incorporated on purpose [39]. On the other hand, indirect validation uses experimental outcomes from other literature or research. Model developers typically cannot control any of an experiment's properties, which results in preference for indirect validation. However, indirect validation is very useful under cost restrictions, experimental difficulties, and difficulty in quantifying property values [39].

## 5.2 PARAMETER DETERMINATIONS

Of three different optimization methods, the Gauss-Newton method showed the lowest SSR values, which implied that the results of the Gauss-Newton method were the most fitted to the measured IAP data. It temporally concluded that the parameter values by the Gauss-Newton method were acceptable to build a muscle IAP model when the range for a parameter was too wide to make a decision. In addition, the physical meanings, the state of the ion channel and the speed of ion movements in the parameters were also considered in determining the values of parameters. Each probability density function in the IAP model shows the changes of ionic conductance and the combinations of parameters, such as  $[\alpha_1, \beta_1, \gamma_1]$ ,  $[\alpha_2, \beta_2, \gamma_2]$ , and  $[\alpha_3, \beta_3, \gamma_3]$ , have a floating relationship among them. This means that the change of one parameter in each combination affects the other parameters in the same combination.

The parameters,  $[\alpha_1, \alpha_2, \alpha_3]$ , were consistent in the objective function with the Erlang PDFs;  $\alpha_1$  and  $\alpha_2$  were 1 and 5, respectively. These values were close to the numbers in the function with gamma PDFs. However,  $\alpha_3$  was computed as 7 with the Gamma PDFs and 8 with the Erlang PDFs. Considering its numerical meaning in the proposed IAP model, the assigned number for  $\alpha_3$  was one of two values, 7 or 8. The other parameters,  $[\beta_1, \beta_2, \beta_3]$ , were approximately determined by considering the values of  $[\alpha_1, \alpha_2, \alpha_3]$ . The range of  $\beta_1$  was between 0.302 and 0.374. However, the SSR values in the steepest descent and the conjugate gradient methods with the Erlang PDFs were relatively high. Therefore, it could be narrowed to the range between 0.302 and 0.336. When 1 was assigned to  $\alpha_1$ , the parameter,  $\beta_1$ , could be assigned to 0.316, which was the result by the Gauss-Newton method with the Erlang PDFs. Using the same approach, 2.924 was

TABLE 5: Selected parameters,  $[\alpha_1, \alpha_2, \alpha_3, \beta_1, \beta_2, \beta_3, \gamma_1, \gamma_2, \gamma_3]$ , based on the results of different optimization methods, such as the Gauss-Newton, the Steepest Descent, and the Conjugate Gradient, for objective functions with the Gamma PDFs or Erlang PDFs.

Parameter	Selected Values	
	SET 1	SET 2
$\alpha_1$	1	1
$\alpha_2$	5	5
$\alpha_3$	7	8
$\beta_1$	0.316	0.316
$\beta_2$	2.924	2.924
$\beta_3$	5.782	6.562
$\gamma_1$	8.711	8.711
$\gamma_2$	599.694	599.694
$\gamma_3$	10984	20373

assigned to  $\beta_2$ . On the other hand,  $\beta_3$  had two different values as  $\alpha_3$ . According to the obtained parameters, the value of  $\alpha_3$  could be two numbers, 7 or 8, which results in  $\beta_3$  possibly having two different values depending on the value of  $\alpha_3$ . Therefore,  $\beta_3$  was assigned to 5.782 when  $\alpha_3$  was 7, and  $\beta_3$  was 6.562 when  $\alpha_3$  was 8. The parameters,  $[\gamma_1, \gamma_2, \gamma_3]$ , were also assigned to specific numbers based on the determinations of other parameters.

### 5.3 VALIDATION FOR THE PROPOSED IAP MODEL

From previous research [105], three muscle IAP data were collected, and they were digitized by using Desktop Ruler (version 1.45). The digitized data were used as new sources for optimization. The Gauss-Newton method was selected based on its performance in the optimizations, and the Erlang PDFs in the objective function were determined with the initial assumption that the values in  $[\alpha_1, \alpha_2, \alpha_3, \beta_1, \beta_2, \beta_3]$  represent

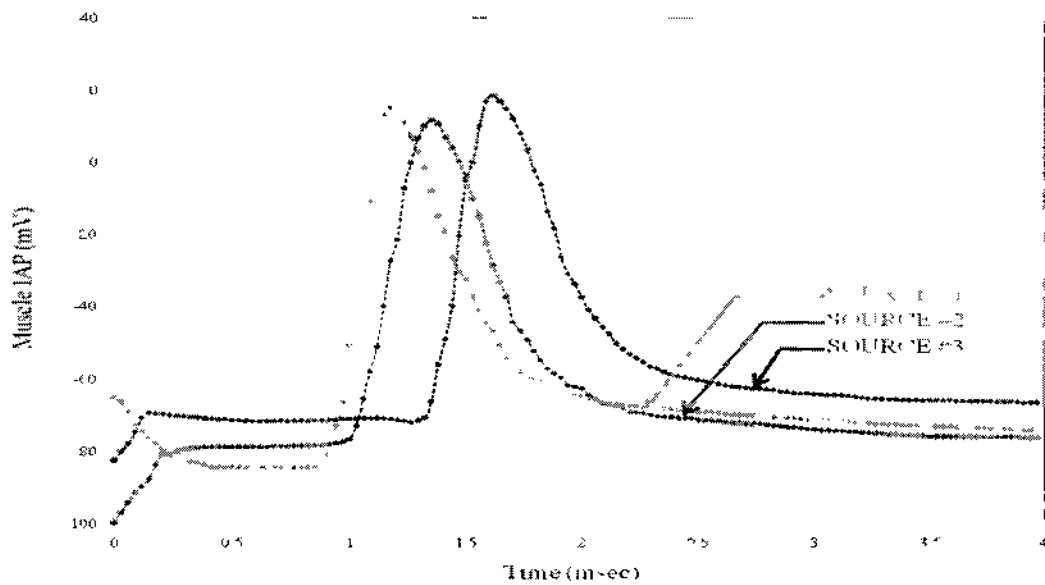


FIG. 24: Digitized measured muscle IAP [105] data for validation. All data were measured from the right m. extensor digitorum longus (EDL) and right m. soleus in the hind limb of rats. The muscle IAP data have different rest membrane potentials; approximately, -84, -77, and -72 mV for source #1, #2, and #3, respectively.

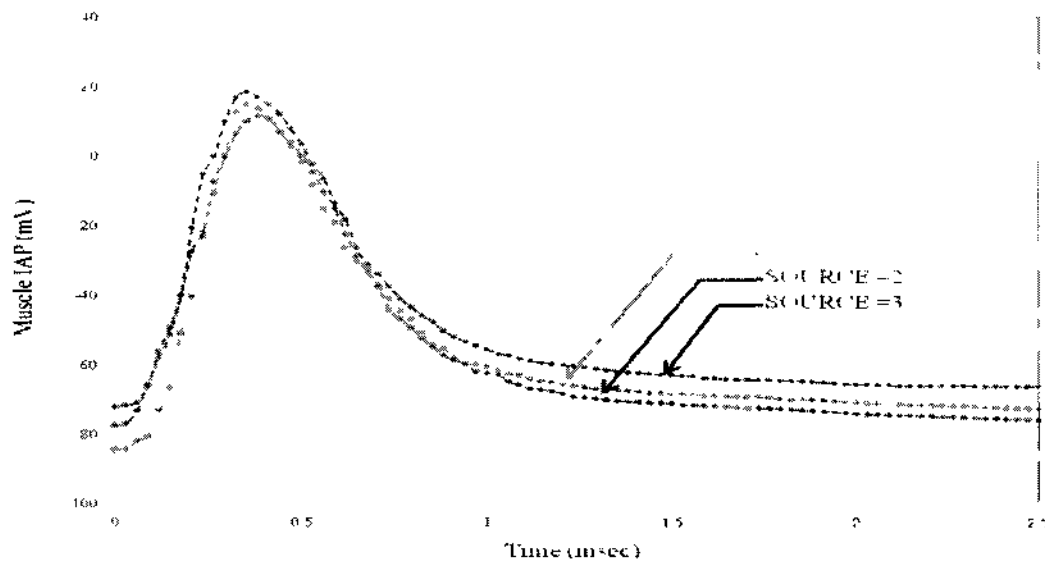


FIG. 25: Removed initial membrane potentials of the digitized IAP data. The highest values were observed approximately at 0.35, 0.38, and 0.35 msec for source #1, #2, and #3, respectively.

the number of ion channel states and the speed of ion movements. After optimization with each source, the results were compared with the selected parameters in Table 5.

### 5.3.1 MODEL VALIDATION: SOURCE 1

The obtained source had the resting membrane potential, -84.42 mV. The initial membrane potential before triggering the action potential was removed from the digitized data and smoothed as the digitized IAP data were smoothed in Matlab (version 7.8) using the function *smooth* with 3 points moving average. In validation, the reduced points for the moving average in smoothing the data were used to avoid any distortions between the digitized and smoothed data. Due to the smoothing, the data loss in the highest value was 1.20%. The objective function for a muscle IAP model was composed of three Erlang PDFs and the Gauss-Newton methods were used for optimization. Two different initial conditions, [1 5 7 0.316 2.924 5.782 8.711 599.694 10984] and [1 5 8 0.316 2.924 6.562 8.711 599.694 20373], caused by the different values in  $[\alpha_3, \beta_3]$  for optimization were applied using the values shown in Table 5. All operational conditions, such as a fractional parameter, optimal step size and parameter updating methods, were the same as shown in the Gauss-Newton optimization method in 4.1.3. The iterative operation continued as long as the sum squared of residue (SSR) decreased.

### 5.3.2 MODEL VALIDATION: SOURCE 2

The obtained source had the resting membrane potential, -77.53 mV. By using Matlab (version 7.8), the digitized IAP data were smoothed with 3 points moving average. The digitized data before a real action potential was triggered were deleted for optimization.

The data loss in the highest value was 1.01% after data smoothing. As in the previous model validation, three Erlang PDFs were the main components in the objective function and the Gauss-Newton method was used for optimization. Including initial conditions, all operational conditions in the Gauss-Newton method were the same as those in the model validation of source 1. In optimization, two different initial conditions were applied, and the program iteration was continued based on the SSR values.

### **5.3.3 MODEL VALIDATION: SOURCE 3**

The obtained source had the resting membrane potential  $-72.10$  mV. As explained in the two previous validations, the function *smooth* with 3 points moving average in Matlab (version 7.8) was used for data smoothing after removing the initial resting membrane potential before an actual action potential. Due to the smoothing, the data loss in the highest value was 1.21 %. The objective function for the muscle IAP model was composed of three independent Erlang PDFs, and the Gauss-Newton method was the main optimizing method. All operational parameters in the method were the same as indicated in the previous validation sections. Two different initial conditions for optimization were applied using the values shown in Table 5. The SSR values in optimization were the main sources to determine whether the process continued.

## **5.4 MODIFICATION**

The three digitized muscle IAP data showed minor differences, such as the time to reach the peak point, the resting membrane potential, and the highest values. For example, the



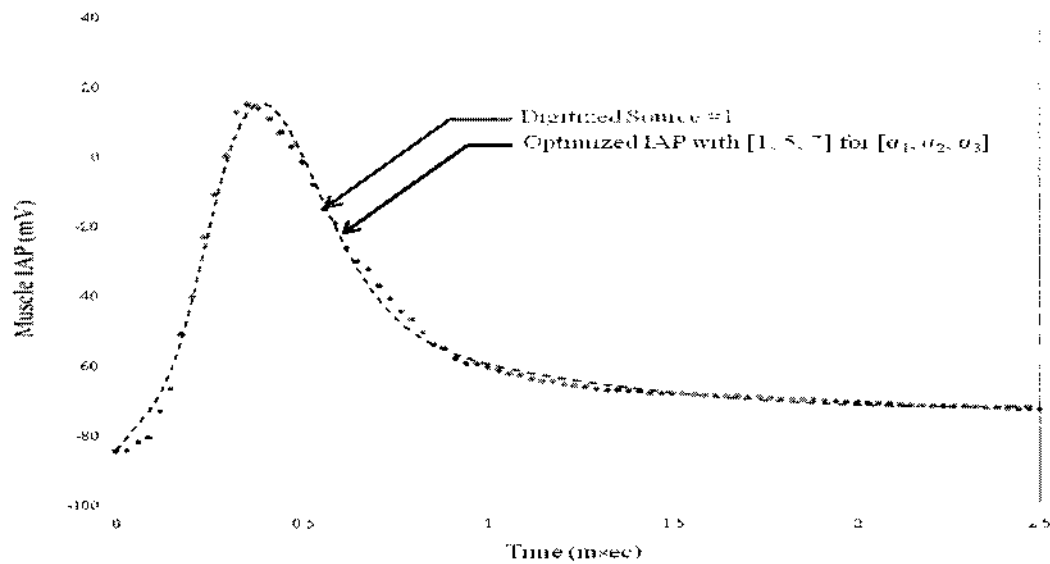


FIG. 26: Source #1 from the measured muscle IAP [105] in dots and the generated IAP in dashes. The initial condition for optimization was [1 5 7 0.316 2.924 5.782 8.711 599.694 10984] and the values in  $[\alpha_1, \alpha_2, \alpha_3]$  were consistent during optimization as [1, 5, 7]. The final SSR was 325.65.

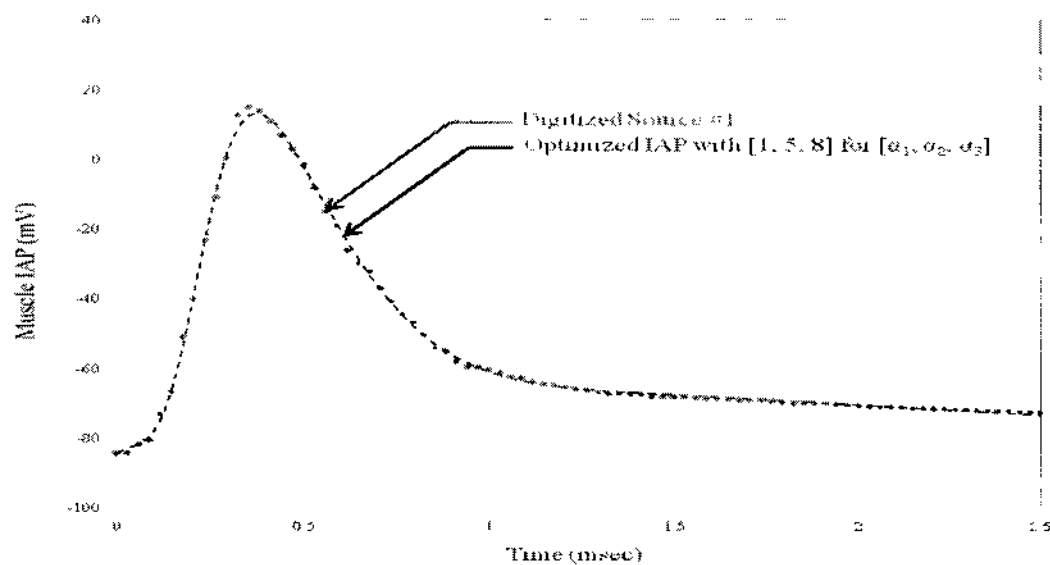


FIG. 27: Source #1 from the measured muscle IAP [105] in dots and the generated IAP in dashes. The initial condition for optimization was [1 5 8 0.316 2.924 6.562 8.711 599.694 20373] and the values in  $[\alpha_1, \alpha_2, \alpha_3]$  were consistent during optimization as [1, 5, 8]. The final SSR was 36.48.

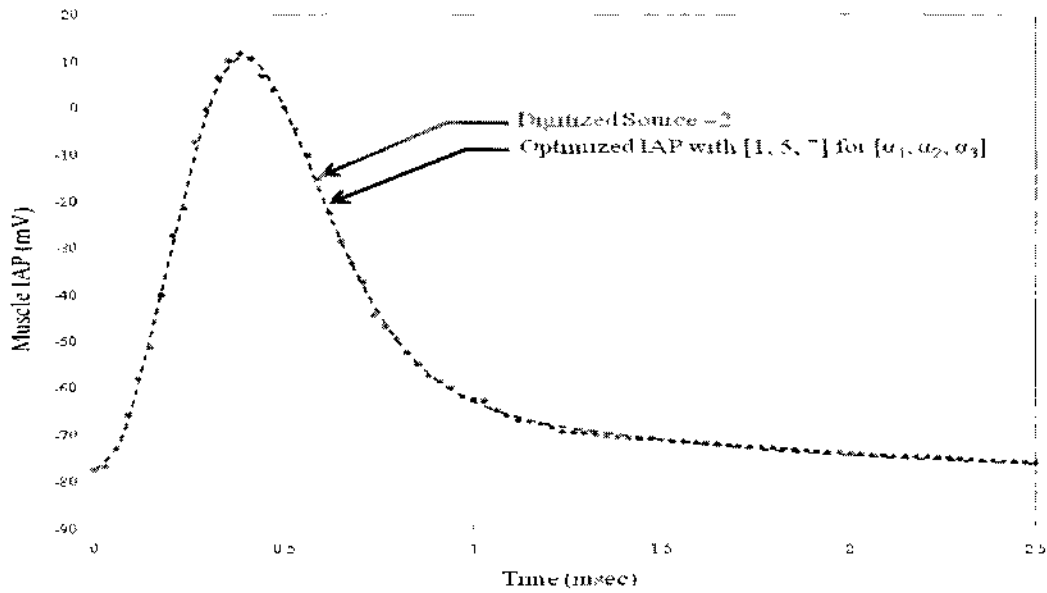


FIG. 28: Source #2 from the measured muscle IAP [105] in dots and the generated IAP in dashes. The initial condition for optimization was [1 5 7 0.316 2.924 5.782 8.711 599.694 10984] and the values in  $[\alpha_1, \alpha_2, \alpha_3]$  were consistent during optimization as [1, 5, 7]. The final SSR was 24.73.

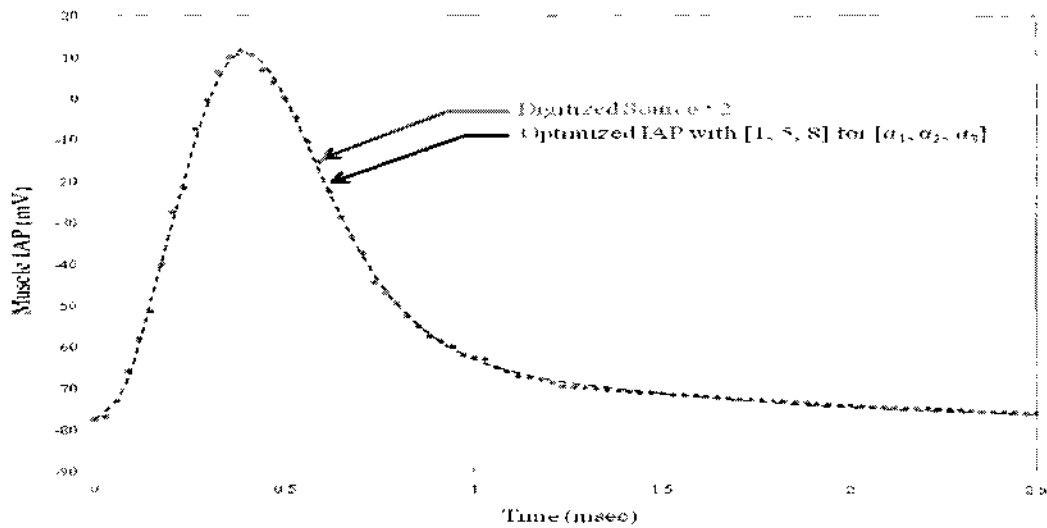


FIG. 29: Source #2 from the measured muscle IAP [105] in dots and the generated IAP in dashes. The initial condition for optimization was [1 5 8 0.316 2.924 6.562 8.711 599.694 20373] and the values in  $[\alpha_1, \alpha_2, \alpha_3]$  were consistent during optimization as [1, 5, 8]. The final SSR was 27.19.

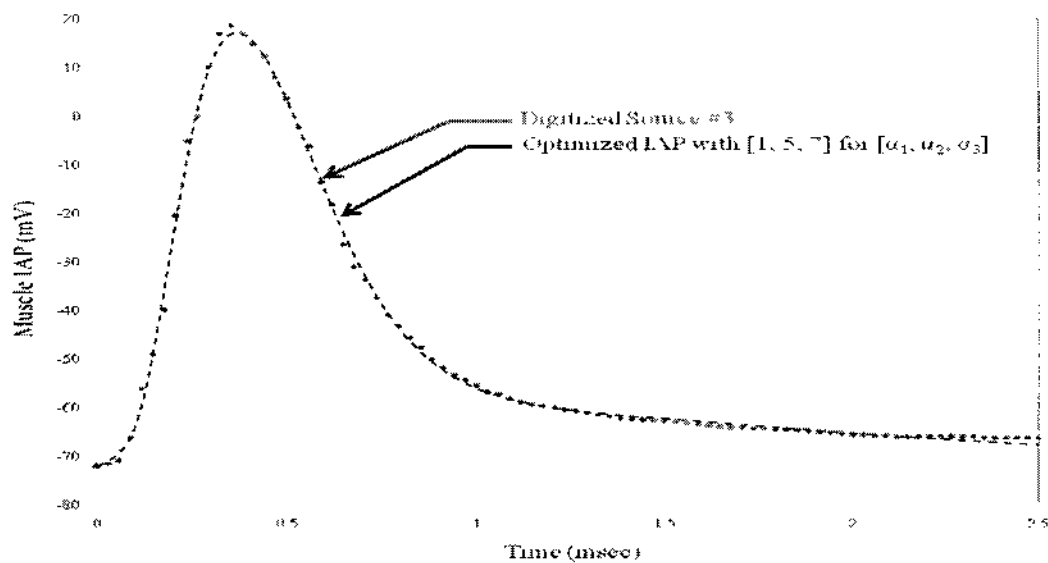


FIG. 30: Source #3 from the measured muscle IAP [105] in dots and the generated IAP in dashes. The initial condition for optimization was [1 5 7 0.316 2.924 5.782 8.711 599.694 10984] and the values in  $[\alpha_1, \alpha_2, \alpha_3]$  were consistent during optimization as [1, 5, 7]. The final SSR was 36.48.

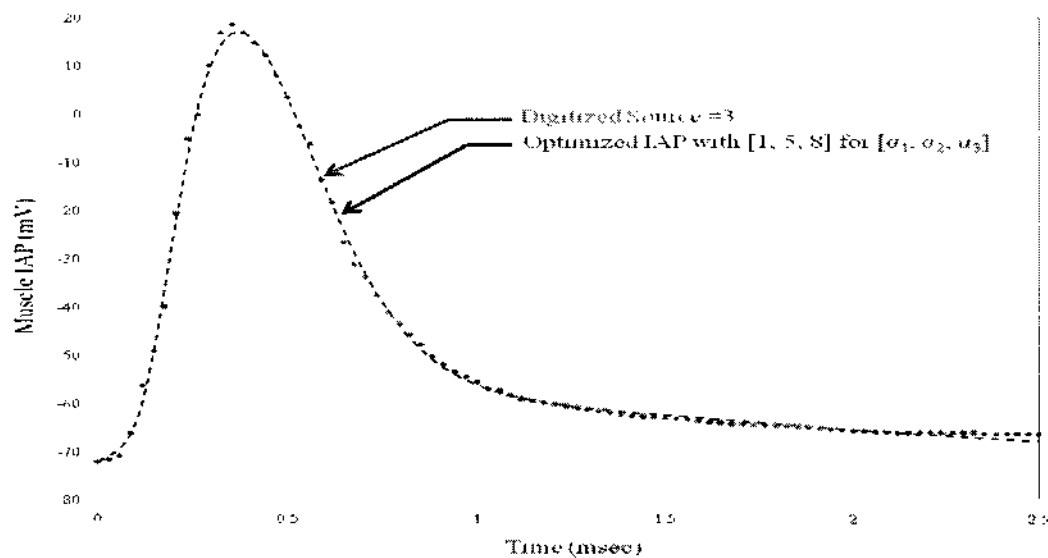


FIG. 31: Source #3 from the measured muscle IAP [105] in dots and the generated IAP in dashes. The initial condition for optimization was [1 5 8 0.316 2.924 6.562 8.711 599.694 20373] and the values in  $[\alpha_1, \alpha_2, \alpha_3]$  were consistent during optimization as [1, 5, 8]. The final SSR was 40.37.

TABLE 6: Summary of computed parameters, [ $\alpha_1, \alpha_2, \alpha_3, \beta_1, \beta_2, \beta_3, \gamma_1, \gamma_2, \gamma_3$ ], by using different sources. The proposed IAP model has three independent Erlang PDFs, and the parameters were matched to the unknown values in the model. Due to the space limitation, all numbers were approximated.

	Initial	SOURCES			Initial	SOURCES		
	SET 1	#1	#2	#3	SET 2	#1	#2	#3
$\alpha_1$	1	1	1	1	1	1	1	1
$\alpha_2$	5	5	5	5	5	5	5	5
$\alpha_3$	7	7	7	7	8	8	8	8
$\beta_1$	0.316	0.47	0.48	0.32	0.316	0.23	0.49	0.33
$\beta_2$	2.924	0.34	3.24	3.14	2.924	2.90	3.25	3.19
$\beta_3$	5.782	4.60	11.31	6.84	6.562	6.47	13.07	8.04
$\gamma_1$	8.711	37.5	19.44	10.98	8.711	11.09	20.12	11.52
$\gamma_2$	599.694	0.002	1257.1	1016.8	599.694	582.61	1268.2	1121.4
$\gamma_3$	10984	4184.1	231437.2	17321.2	20373	18784.9	1066583.8	48822.7
SSR	--	325.65	24.73	36.48	--	36.48	27.19	40.37

times to reach the peak point during excitation were 0.35, 0.38, and 0.35 msec for source #1, #2, and #3, respectively, which meant that the highest value was observed in source #2 later than those of the other sources. In addition, the resting membrane potentials of the sources also varied in the range between -84.42 and -72.10 mV. However, all sources showed the typical characteristics of muscle IAP. For instance, all sources lasted less than 2 msec for excitation, and there was no excessive repolarization, so called hyperpolarization. Specifically, total action potential amplitudes were bigger than 60 mV, and the rising times<sup>10</sup> of these action potentials were not more than 0.16 msec.

Based on the results of IAP modeling in Chapter 4, the proposed IAP model contained three Erlang PDFs, which represented ion conductance, and the Gauss-Newton method was used for optimization. Depending on the initial conditions for the parameters,

<sup>10</sup> The duration between 10 and 90 % in depolarizing phase of an action potential [44]

the computational results of unknown parameters,  $[\alpha_1, \alpha_2, \alpha_3, \beta_1, \beta_2, \beta_3, \gamma_1, \gamma_2, \gamma_3]$ , were differently optimized.

Due to the relatively high SSR value, the results of source #1 in the initial set 1 were first removed from consideration. The values in  $[\alpha_1, \alpha_2, \alpha_3]$  were consistent as indicated in the initial conditions, and they could be chosen as [1, 5, 7] or [1, 5, 8]. However, the results of source #1 by the initial set 1 implied that a muscle IAP model might be incorrect when using [1, 5, 7] for  $[\alpha_1, \alpha_2, \alpha_3]$  in some data. Therefore, the values for  $[\alpha_1, \alpha_2, \alpha_3]$  were determined by [1, 5, 8]. To validate other important parameters,  $[\beta_1, \beta_2, \beta_3]$ , the meaningful separations of obtained parameters were necessary. For example, the proposed muscle IAP model was composed of three independent modified Erlang PDF, and each PDF was supposed to represent a specific ion conductance. Therefore, the parameters could be combined as  $[\alpha_i, \beta_i, \gamma_i]$ ,  $[\alpha_2, \beta_2, \gamma_2]$ , and  $[\alpha_3, \beta_3, \gamma_3]$ . From the physiological background of ion conductance, the conductance by leakage has very small effects on the muscle IAP while  $\text{Na}^+$  and  $\text{K}^+$  conductances have a major impact. In addition, the values in  $[\gamma_1, \gamma_2, \gamma_3]$  showed the simple amplitude for each Erlang PDF to adjust to the measured IAP, which meant that their values were very dependent upon the other parameters,  $[\alpha_1, \alpha_2, \alpha_3, \beta_1, \beta_2, \beta_3]$ . Therefore, the considerations for  $[\gamma_1, \gamma_2, \gamma_3]$  were omitted, and their values were determined based on the other parameters.

The obtained value of  $\beta_2$  had the range between 2.90 and 3.25 while its initial value was 2.924. When considering that this value came from the measured biological data, it was reasonable to present a possible range for each parameter. However, the aim in this study was to make a muscle IAP model, and an average value was computed using the obtained numbers. Based on the initial and obtained numbers, the computed number was

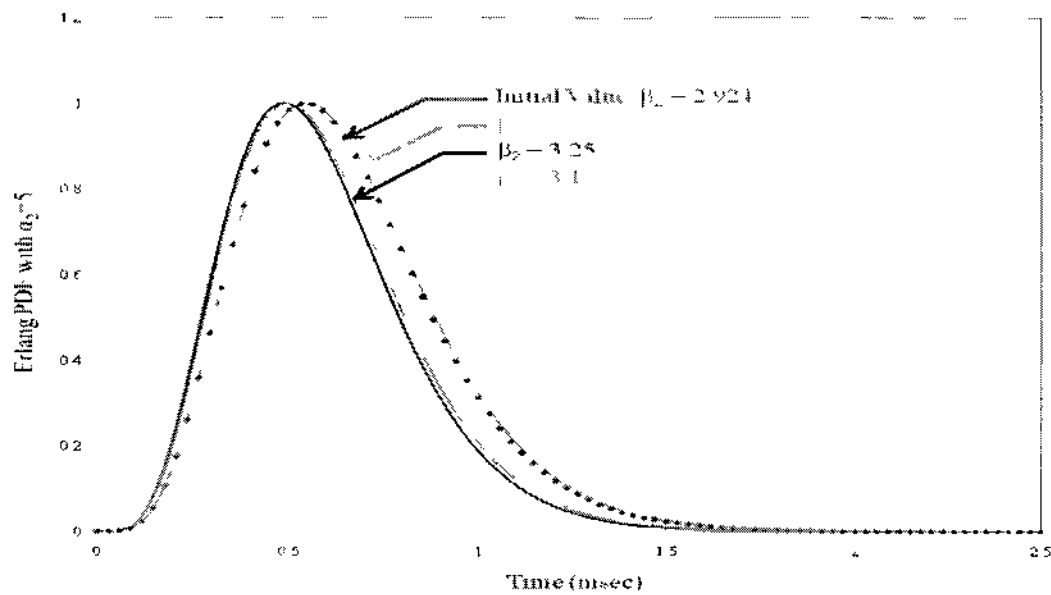


FIG. 32: Normalized Erlang PDF with  $\alpha_2=5$ . The dots plotted results with the initial values containing  $\beta_3=2.924$ . The lines represent the sources #1 ( $\beta_3=2.90$ ), #2 ( $\beta_3=3.25$ ), and #3 ( $\beta_3=3.19$ ), respectively.

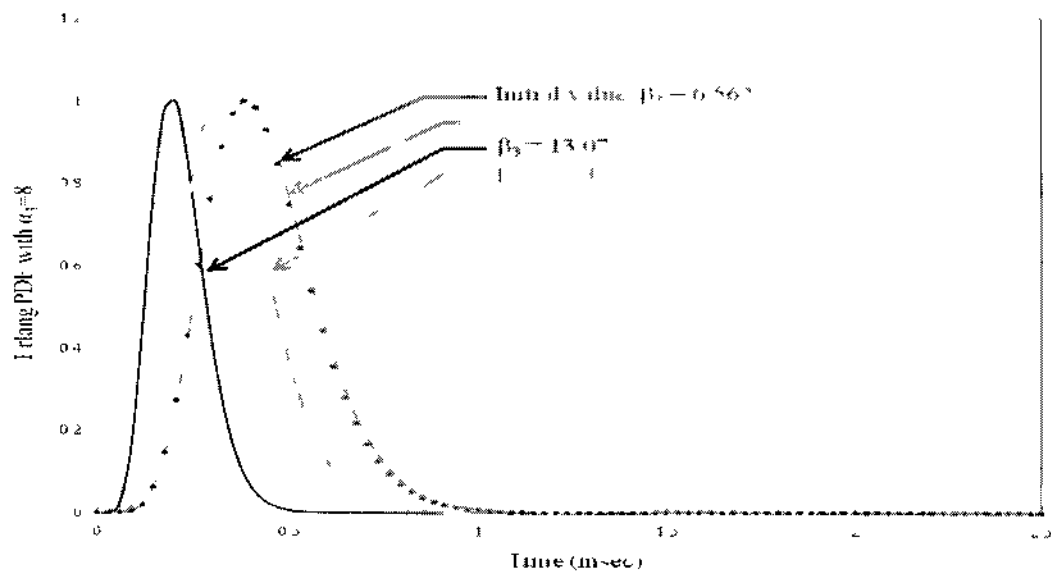


FIG. 33: Normalized Erlang PDF with  $\alpha_3=8$ . The dots plotted results with the initial values containing  $\beta_3=6.562$ . The lines represent the sources #1 ( $\beta_3=6.47$ ), #2 ( $\beta_3=13.07$ ), and #3 ( $\beta_3=8.04$ ), respectively.

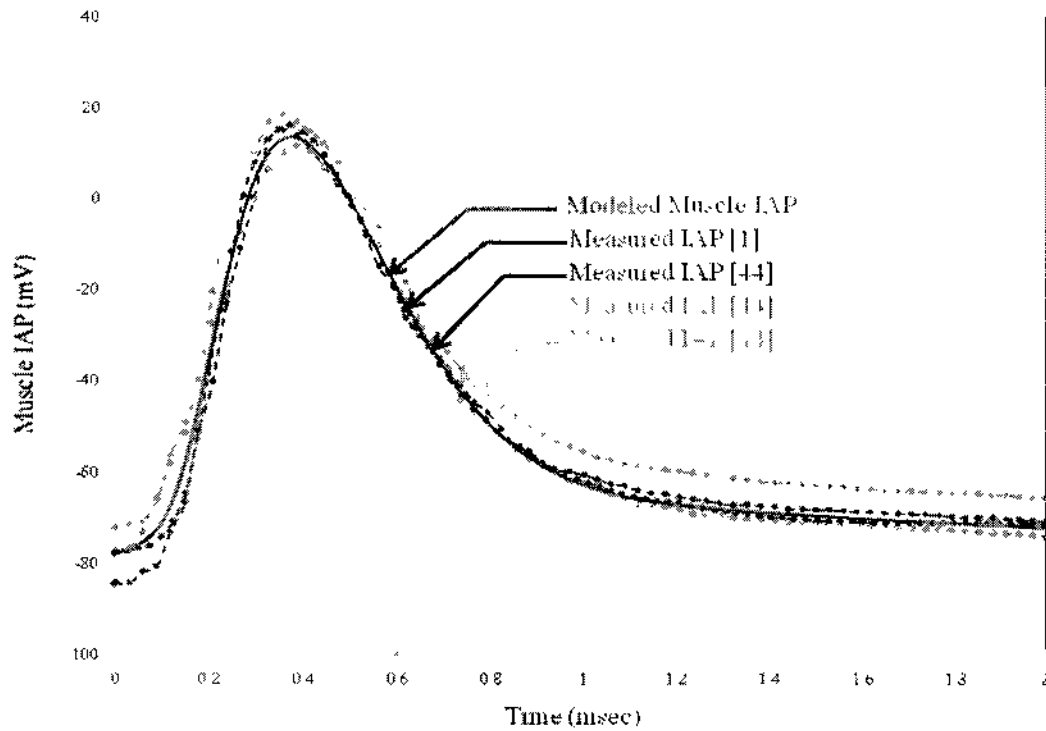


FIG. 34: Modeled muscle Intracellular Action Potential (IAP) with measured IAPs from different references [17,105]. The model consisted of three independent Erlang PDFs, and nine parameters were assigned. These parameters were [1, 5, 8, 0.33, 3.07, 7.02, 9.68, 890.83, 21772] for  $[\alpha_1, \alpha_2, \alpha_3, \beta_1, \beta_2, \beta_3, \gamma_1, \gamma_2, \gamma_3]$ , respectively.

TABLE 7: Final parameters for the muscle IAP model. By considering biological characteristics in the generation of a muscle IAP, 6 parameters,  $[\alpha_1, \alpha_2, \alpha_3, \beta_1, \beta_2, \beta_3]$ , were determined and the other parameters,  $[\gamma_1, \gamma_2, \gamma_3]$ , were optimized by using the Gauss-Newton method.

	Final Parameters
$\alpha_1$	1
$\alpha_2$	5
$\alpha_3$	8
$\beta_1$	0.33
$\beta_2$	3.07
$\beta_3$	7.02
$\gamma_1$	9.68
$\gamma_2$	890.83
$\gamma_3$	21772

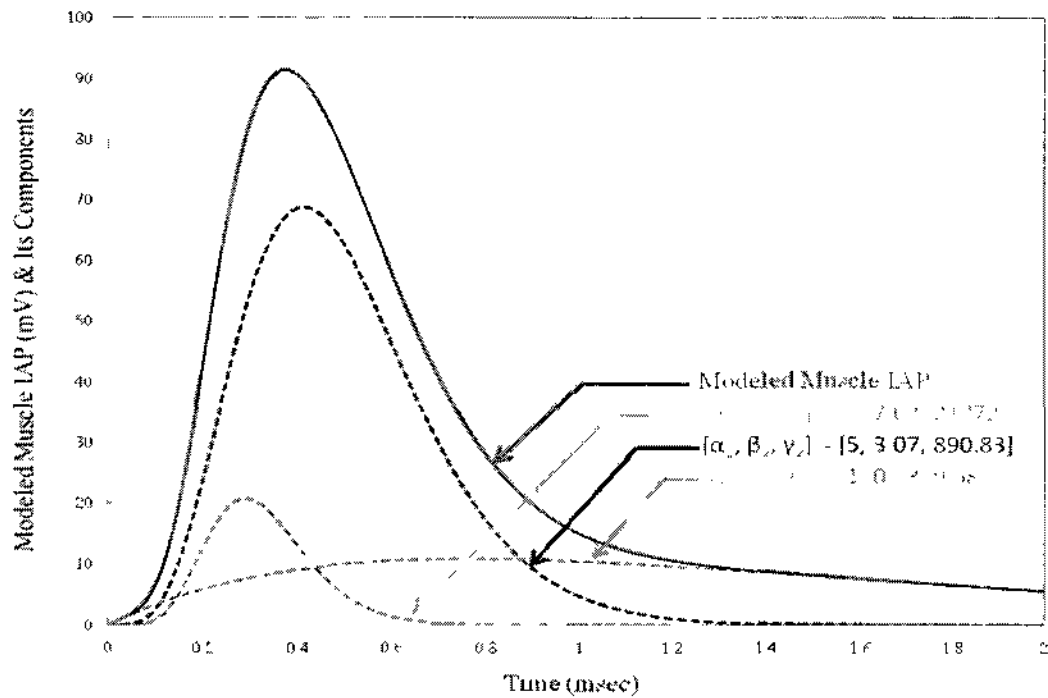


FIG. 35: Modeled muscle Intracellular Action Potential (IAP) with its components. The modeled IAP is composed of three independent components which are assumed to be related with each ion channel conductance.

3.07 for  $\beta_2$ . Unlike  $\beta_2$ , there was a relatively wide range for  $\beta_3$  because of the high value from source #2. The value of  $\beta_3$  from source #2 can be a possible number for  $\beta_3$ , but it was relatively far from the other values for  $\beta_3$ . Therefore, only three sources including the initial value were used to compute the number of  $\beta_3$ , which was 7.02. To complete the IAP model, optimization with the 6 obtained values,  $[\alpha_1, \alpha_2, \alpha_3, \beta_1, \beta_2, \beta_3]$ , and 3 unknown parameters,  $[\gamma_1, \gamma_2, \gamma_3]$ , was repeated using the Gauss-Newton method as shown in Chapter 4. The final values for the muscle IAP model were as shown in Table 7.



## CHAPTER 6

### DISCUSSIONS

By adopting the relationship between IAP generation and multiple ion channel conductivities as shown in H-H neuron experiments, a muscle IAP model has been successfully constructed. Unlike previous muscle IAP models, the newly proposed muscle IAP model contains some unique advantages to show ion channel conductivities during cell excitation and to compute the separate ionic current for each ion type.

#### 6.1 ION CHANNEL (CONDUCTANCE) MODELING

Typical models of ion channel dynamics or kinetics are developed in a stochastic fashion because of the discrete conductance levels of ion channels through the patch clamp technique [2,3]. In voltage-gated ion channels, the ionic movement is critical for generation of biological potentials, and the stochastic process of channel gating underlying the potential is fundamental to understanding the ion flow through channels. Generally, the stochastic properties of ion channels are modeled by using stationary Markov models (SMM)<sup>11</sup> [2]. A SMM is easily able to represent the various topologies of ion channels, which are directly related to the multiconformational characteristics of an ion channel. For example, a Na<sup>+</sup> ion channel is composed of proteins such as four  $\alpha$ -subunits and one to three  $\beta$ -subunits. In an  $\alpha$ -subunit, there are four homologous domains that consist of six membrane segments and each domain contains the selective filter, voltage sensor, and TTX<sup>12</sup> binding site. The different conformations of these proteins in the Na<sup>+</sup> ion channel reveal its specific states. Even though the number of proteins is

---

<sup>11</sup> The statistic models for a real- world process to transit from one to another state.

<sup>12</sup> Tetrodotoxin. By attaching to a specific site, it blocks action potentials.

different, this relationship between the conformation and the state of ion channel is true in all other voltage-gated ion channels. However, it has been unsolved as to how many stable states actually exist during the dynamics of an ion channel.

Since the structure of a  $K^+$  ion channel from bacteria was revealed in 1998 [24], X-ray crystallography has been widely used to physically view the real states of ion channels. By crystallizing an ion channel at a certain state, its structure is revealed through X-ray diffraction analysis. With this advanced method, the open state structure of the voltage-gated ion channels has been successfully solved [92,94]. However, the closed state of ion channels still remains unknown, especially in conformational channel structures. Therefore, ion channel modeling can be different depending on the number of the closed channel states [30,62]. Nevertheless, most ion channel models possess ambiguity in determining the number of closed channel states because of the difficulties in distinguishing different ion channels in closed states [74].

For the ion channel model in this study, the optimized numbers for  $\alpha$  were used to represent the possible ion channel states including an open state. As explained in Chapter 4, the increased numbers in  $\alpha$  at the graphically same location generate the narrower signal pattern. When considering the relationship between the number of proteins in a channel and their state numbers, more proteins in a channel result in the higher values in the parameter,  $\alpha$ . For example, a  $Na^+$  ion channel with four subunits and two subunit accessories in skeletal muscle had 8 different channel states based on the determined parameter,  $\alpha_3$ . Apparently, this number cannot represent a specific state topology of a  $Na^+$  ion channel, but it may provide the minimum number of states that can reveal the stable invariant manifolds of the proteins in the channel [47]. Also, the computed number, 5, for

$\alpha_2$  implies the possible states of the  $K^+$  ion channel, and 1 was assigned to  $\alpha_1$  for leakage in the channel model of this study. With the assumption in these numbers, other parameters can also be determined. Specifically, the parameter  $\beta$  controls the increasing and decreasing rates, which means that a lower value in  $\beta$  produces a faster increase or decrease. From the aspect of ion movement, these changes in conductance can be partially caused by the speed of ion movement, which is one of the important factors in deciding the biological function of the channels [35].

As explained, the proposed ion channel model, specifically ion channel conductance model, was developed with electrophysiological considerations and experimental facts. As shown by the study of Hodgkin and Huxley (H-H), the action potential in cells is generated by the driving forces of channel conductances and the proposed ion channel conductance models for  $Na^+$ ,  $K^+$  and leakage under the action potential model in this study consistently show the previous theory by H-H.

## **6.2 ION CHANNEL CONDUCTIVITY**

The conductivities of  $Na^+$  and  $K^+$  channels lead to depolarization and repolarization, respectively, during cell excitation, and their dynamic properties are critical in modeling an IAP, especially in muscle. As shown in the H-H experiments [11], the patterns of these ion channel conductances were apparently different in duration.  $Na^+$  channel conductance was characterized as a fast increase and a fast decrease within a short time period. Even though the strength of an applied stimulus could change the amplitude of  $Na^+$  conductance, the responding pattern of the  $Na^+$  conductance to different stimuli was similar. In addition, the responding time was shorter as the applied stimulus became

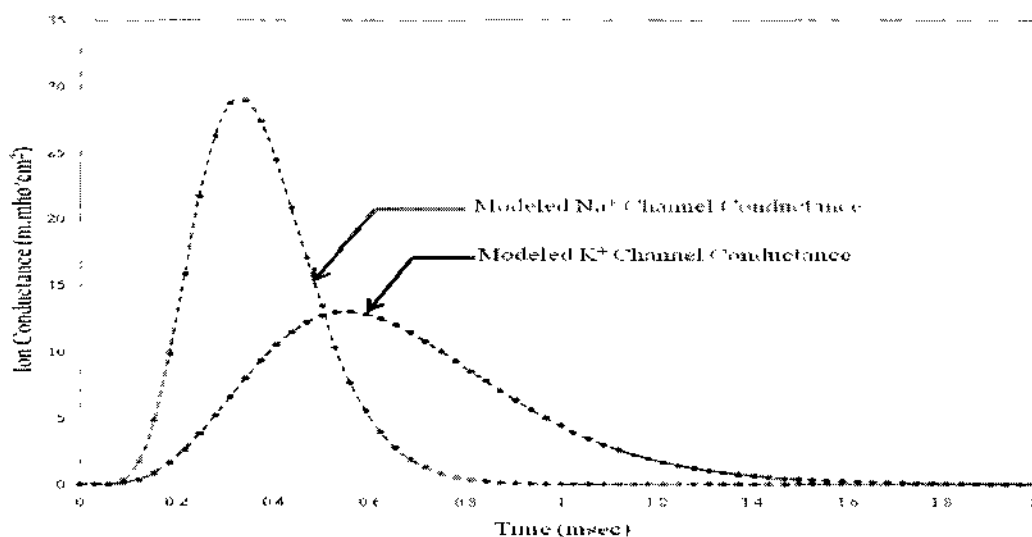


FIG. 36: Generated conductances for Sodium ( $\text{Na}^+$ ) and Potassium ( $\text{K}^+$ ) in nerve. The provided parameters for each conductance were obtained from the result by the Gauss-Newton optimization method with the Erlang PDFs.  $[\alpha_{\text{Na}}, \beta_{\text{Na}}]$  were [8, 1.34], and  $[\alpha_{\text{K}}, \beta_{\text{K}}]$  were [5, 1.21]. The amplitudes for conductances were modified based on the H-H neuron model.

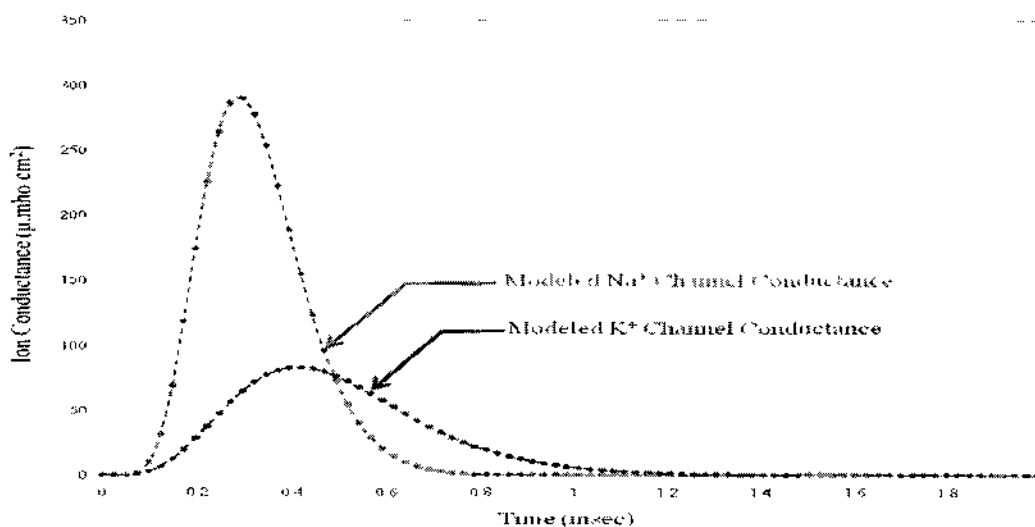


FIG. 37: Generated conductances for Sodium ( $\text{Na}^+$ ) and Potassium ( $\text{K}^+$ ) in muscle. The provided parameters for each conductance were obtained from the result by the Gauss-Newton optimization method with the Erlang PDFs.  $[\alpha_{\text{Na}}, \beta_{\text{Na}}]$  were [8, 7.02], and  $[\alpha_{\text{K}}, \beta_{\text{K}}]$  were [5, 3.07]. The maximum amplitudes for conductances were obtained from a previous paper [78].

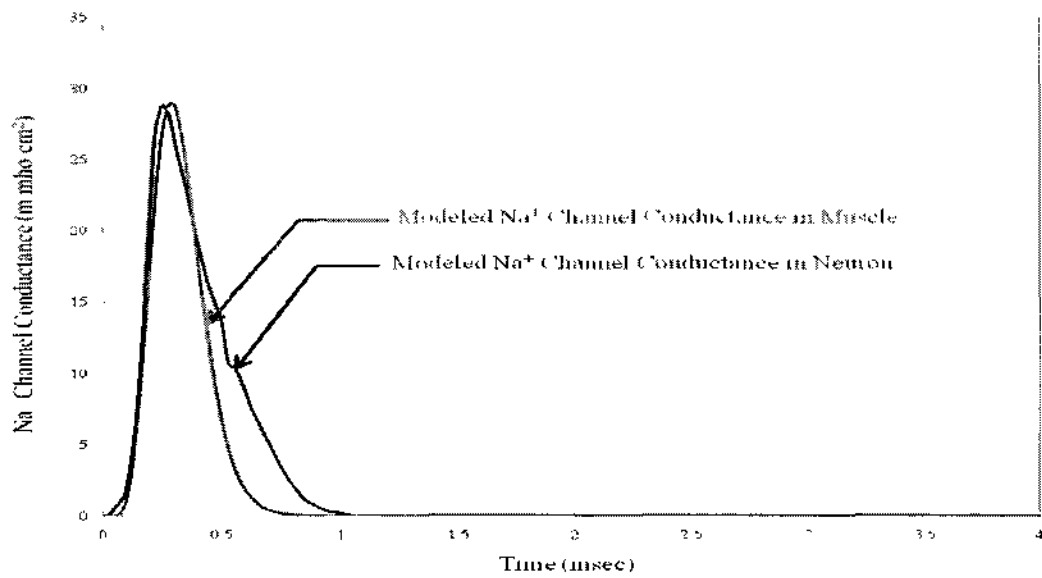


FIG. 38:  $\text{Na}^+$  conductances of muscle and neuron. The  $\text{Na}^+$  channel conductance for neuron was based on H-H model and the generated  $\text{Na}^+$  channel conductance for muscle was by the Erlang PDF with [8, 7.02] for  $[\alpha_{\text{Na}}, \beta_{\text{Na}}]$ , respectively. For comparison, the maximum amplitudes for conductance in muscle were adjusted to those in neuron.

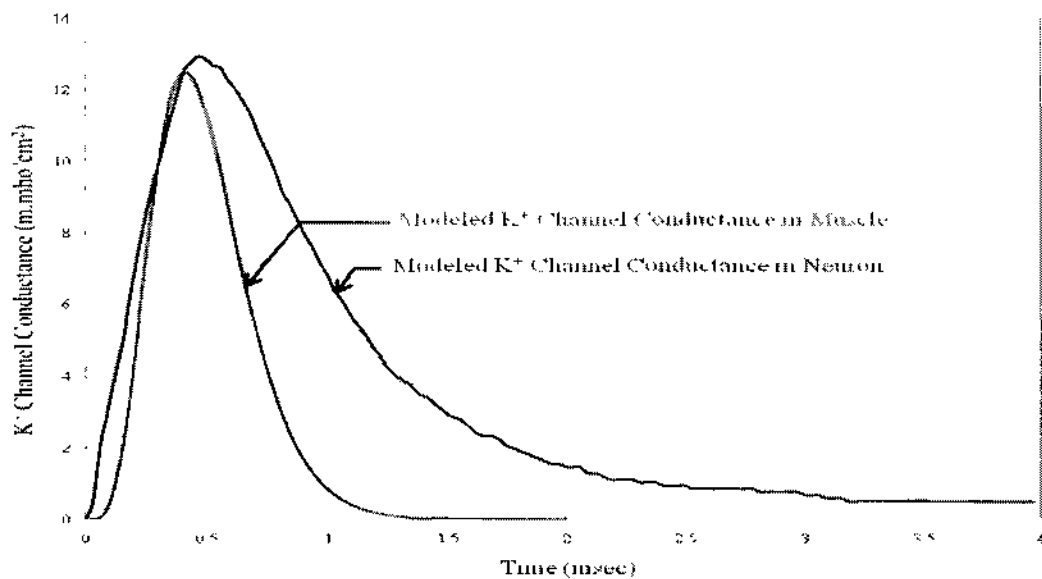


FIG. 39:  $\text{K}^+$  conductances of muscle and neuron. The  $\text{K}^+$  channel conductance for neuron was based on H-H model and the generated  $\text{K}^+$  channel conductance for muscle was by the Erlang PDF with [5, 3.07] for  $[\alpha_{\text{Na}}, \beta_{\text{Na}}]$ , respectively. For comparison, the maximum amplitudes for conductance in muscle were adjusted to those in neuron.

larger. On the other hand,  $K^+$  channel conductance was identified with a relatively slower increase than  $Na^+$  channel conductance during depolarization and lasted as long as an applied stimulus remained. The increased strength of a stimulus made the increasing rate greater and the maximum conductances for different stimuli were continuously maintained with a constant stimulus. These specific characteristics are captured well in the generated nerve IAP (Figure 36) from the result by the Gauss-Newton optimization method with Erlang PDFs. Those similar changes in ion conductances were also shown in muscle (Figure 37). As explained in Chapter 2, most mechanisms to generate a muscle IAP are similar to a nerve IAP. The only difference between them is the number of ions involved with generating an IAP. Specifically, two ions,  $Na^+$  and  $K^+$ , play a dominant role in generating a muscle IAP, and their conductances are the key in generating a meaningful muscle IAP.

In Figures 38 and 39, the comparisons between the generated  $Na^+$  and  $K^+$  channel conductances in muscle and neuron are shown. The generated  $Na^+$  and  $K^+$  channel conductances in muscle were based on the Erlang PDFs in the currently generated muscle IAP model in this study and those in neuron were based on the H-H models [11]. Due to the difference in amplitude, the amplitudes of the conductances in muscle were increased to match those in neuron for comparison. The  $Na^+$  channel conductances in muscle and neuron showed similar profiles during cell excitation. However, the  $K^+$  channel conductance in neuron presented a longer time duration than that of the Erlang PDF in the muscle IAP model in this study. It is reasonable because there are some differences in the IAP profiles of muscle and neuron; for example, the duration of IAP in neuron is longer than that in muscle, and there is no hyperpolarization in muscle.

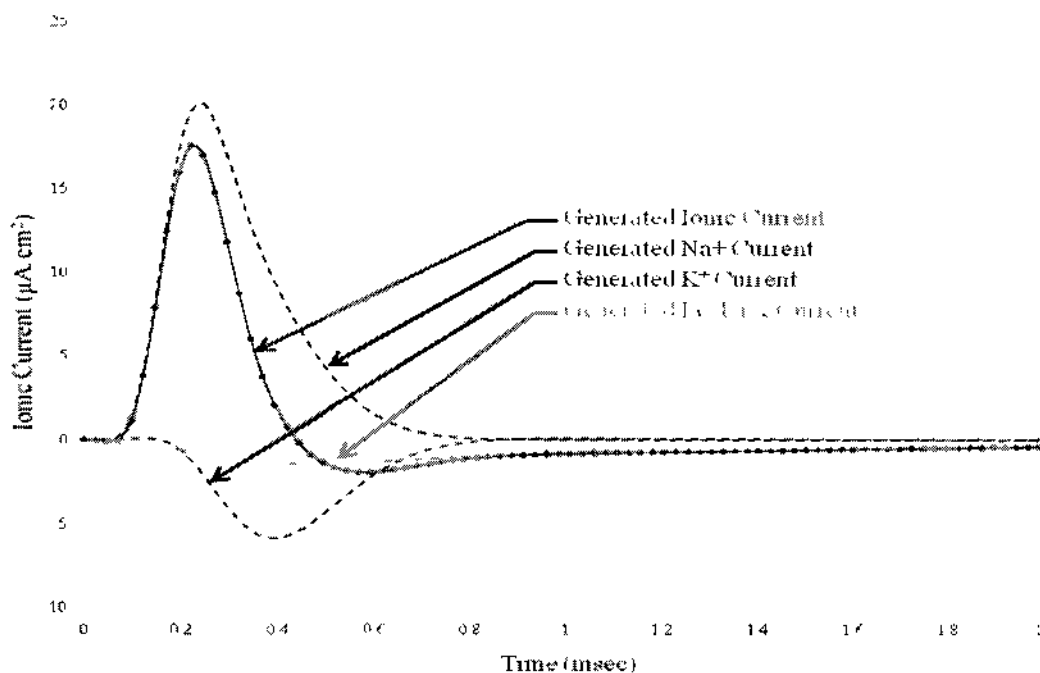


FIG. 40: Generated ionic currents for Sodium ( $\text{Na}^+$ ), Potassium ( $\text{K}^+$ ), and leakage in muscle. The consolidated ionic current was computed by the summation of the generated currents for  $\text{Na}^+$ ,  $\text{K}^+$ , and leakage.

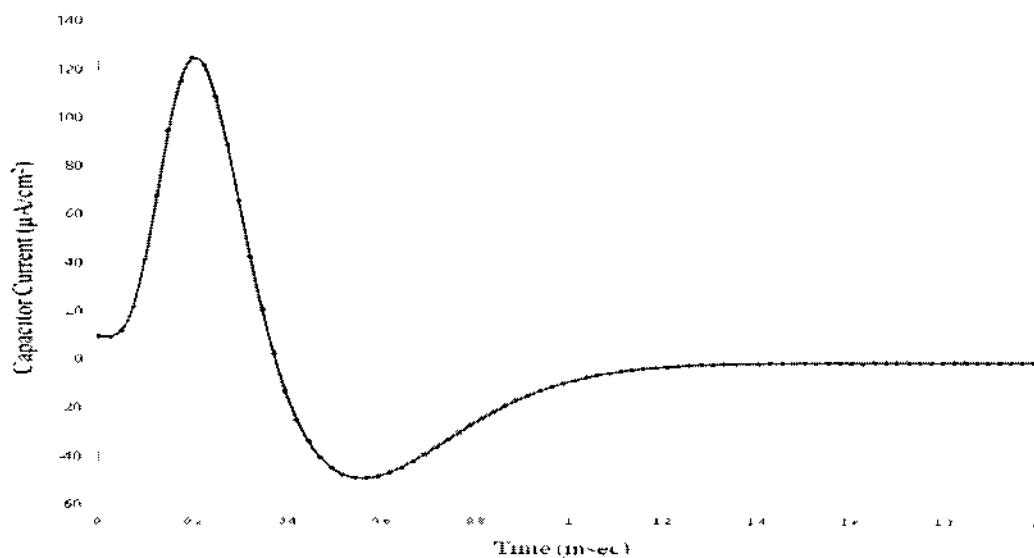


FIG. 41: Generated capacitor current in muscle. The membrane capacitor,  $C_m$ , was assumed as  $1 \mu\text{F}/\text{cm}^2$  as many previous studies suggested [11,72,75,78,89].

### 6.3 TOTAL IONIC CURRENT

The H-H circuit model (Figure 2) showed that the ionic current through cell membrane could be computed using ion conductances. As shown in equations (1.1)-(1.3), the summation of the individual ionic currents produces the consolidated ionic current. The total ionic current is eventually provided by adding the capacitive current to the consolidate current. Based on the generated ion conductances, each ionic current for  $\text{Na}^+$ ,  $\text{K}^+$  and leakage are computed as follows:

$$I_{\text{Na}} = g_{\text{Na}}(V_m - E_{\text{Na}}) \quad (6.1)$$

$$I_{\text{K}} = g_{\text{K}}(V_m - E_{\text{K}}) \quad (6.2)$$

$$I_{\text{L}} = g_{\text{L}}(V_m - E_{\text{L}}) \quad (6.3)$$

where  $V_m$  is the membrane potential, and  $E_x$  represents equilibrium potential for an ion species,  $x$ . The resting membrane potential was  $-77.7$  mV from the final muscle IAP model (Figure 34), and  $63$  mV and  $-58$  mV were applied for  $E_{\text{Na}}$  and  $E_{\text{K}}$ , respectively [26]. The equilibrium for the leakage was decided by considering that the leakage current has a small effect on the ionic current, and it was assumed to be  $-70$  mV. For the ion conductance models, the parameters by the Gauss-Newton optimization method with Erlang PDFs were applied with  $[1, 0.33, 5, 3.07, 8, 7.02]$  for  $[\alpha_{\text{L}}, \beta_{\text{L}}, \alpha_{\text{K}}, \beta_{\text{K}}, \alpha_{\text{Na}}, \beta_{\text{Na}}]$ , respectively. All amplitudes of ion conductances were modified based on the H-H neuron model. The ionic current was computed using equation (1.1). To find the total ionic current, a capacity current was added to the consolidated ionic current and computed as follows:



$$I_c = C_m \frac{dV_m}{dt} \quad (6.4)$$

where  $C_m$  is the membrane capacity, which is generally  $1 \mu\text{F}/\text{cm}^2$ . Based on the above computations, the total ionic current can be calculated using equation (1.4). Due to the limits of experimental references in capacitor currents, the total ionic current is not shown in this study.

#### 6.4 TRANSMEMBRANE CURRENT

Transmembrane current<sup>13</sup> is also called transmembrane ionic current and can be computed by the second derivative of the IAP [75,89]. Mathematical generation of the transmembrane current is possible using the core conductor model [45]. By simplifying a real excitable cell with some specific assumptions, the core conductor model can generate the transmembrane current. The assumptions used by the core conductor model are listed as follows:

- (1) Two conductors, the intracellular and extracellular fluids, are separated by the cell membrane. Both fluids are homogeneous and isotropic, and they follow Ohm's law.
- (2) An excitable cell has a cylindrical and symmetric shape.
- (3) Any magnetic effects are ignored.
- (4) The current flows in intracellular and extracellular fluids move longitudinally.

With assumption (1), the intracellular and the extracellular potentials can be computed as follows:

---

<sup>13</sup> The flowing current through the cell membrane caused by the potential difference between intra- and extracellular fields

$$\frac{dV_e}{dt} = -r_e i_e \quad (6.5)$$

$$\frac{dV_i}{dt} = -r_i i_i \quad (6.6)$$

where  $V_i$  and  $V_e$  are the intracellular and extracellular potentials, respectively.  $i_i$  and  $i_e$  are the intracellular and extracellular currents, respectively.  $r_i$  and  $r_e$  are the intracellular and extracellular resistors, respectively. Using assumptions (2) and (3), the following relations can be obtained.

$$\frac{di_i}{dt} = -2\pi a i_m \quad (6.7)$$

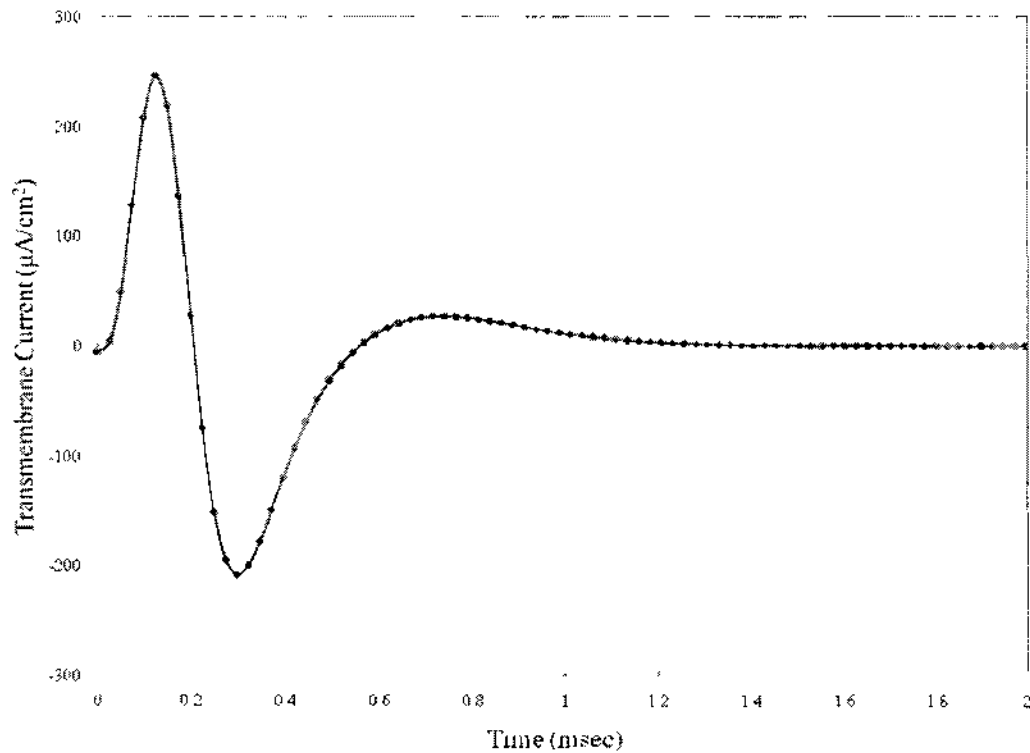


FIG. 42: Generated Transmembrane current in muscle. The cell radius ( $a$ ) and the intracellular resistor ( $r_i$ ) were obtained from a previous study [78] and they were  $27.5 \mu\text{m}$  and  $4209.06 \text{ k}\Omega/\text{cm}$  respectively.

$$i_i(t) = -i_e(t) \quad (6.8)$$

where  $a$  is the radius of the cell, and  $i_m$  is the transmembrane current. Using equations (6.5), (6.6) and (6.8), the relation between  $V_i$  and  $V_e$  can be calculated as follows:

$$\frac{1}{r_e} \frac{dV_e}{dt} + \frac{1}{r_i} \frac{dV_i}{dt} = 0 \quad (6.9)$$

$$V_e(t) = -\frac{r_e}{r_i} V_i(t) \quad (6.10)$$

Based on equations (6.6) and (6.7),

$$2\pi a i_m = \frac{1}{r_i} \frac{d^2 V_i}{dt^2} \quad (6.11)$$

Therefore, the transmembrane current can be computed as follows:

$$i_m = \frac{1}{2\pi a r_i} \frac{d^2 V_i}{dt^2} \quad (6.12)$$

As shown in equation (6.12), the transmembrane current can be computed by the second derivative of the intracellular potential.

From a previous study [106], the specific values for a cell radius and an intracellular resistor were obtained, and they were 27.5  $\mu\text{m}$  and 4209.06  $\text{k}\Omega/\text{cm}$  respectively. In addition, the conduction velocity<sup>14</sup> (CV) was assumed to be 4  $\text{m}/\text{sec}$ , which is the most general CV in a muscle fiber [108-110], and it was used to find the correct unit for the

---

<sup>14</sup> The propagating velocity of an action potential in an excitable cell

transmembrane current. By applying these values, the transmembrane current was generated (Figure 39).

## 6.5 APPLICATIONS OF ION CHANNEL MODELS

As shown in muscle IAP modeling, an ion channel (conductance) model provides the fundamental sources to generate an IAP. Moreover, an ion channel model can be used in generating the ionic currents for specific ions such as  $\text{Na}^+$  and  $\text{K}^+$ , which is not easy to measure in experimental laboratories. Using an ion channel model, only simple mathematical computations are required to generate the ionic currents. This is not the only benefit from ion channel models when considering that ion channels are closely related to many cellular functions and various pathological disorders [15,25], especially in excitable cells such as neurons, cardiac myocytes, and skeletal muscle fibers. The applications for ion channels are also varied from simple electrophysiological research to hypothalamic neural thermosensitivity [69]. Recently, ion channels have been used as targets for many venom<sup>15</sup> peptides [90], and these applications of ion channels are possible when the structures and characteristics of ion channels become explicit. An ion channel model can be successfully used in understanding the characteristics of ion channels when mainly focused on electrophysiological features.

Due to their critical role in physiological processes, ion channels have been considered important therapeutic targets [36]. Based on the structural and electrophysiological characteristics of ion channels, a new drug or chemical for specific channels can be designed. In particular, the electrophysiological dynamics in ion

---

<sup>15</sup> Toxins discharged by certain types of animals to inject their victims

channels should be comprehended for therapeutic strategies for a new drug. An ion channel model can be useful for examining how fast a newly developed medicine affects a specific target area or how long the effects of the medicine last in that area. For example, consider the case where there are two ion channels for the path of a drug, and let's assume that the ion channels are  $\text{Na}^+$  and  $\text{K}^+$  channels. As shown in the previous ion channel conductivities, the conductivities of these ion channels are different in a reactive time and duration as much as their maximal amplitudes during cell excitations. If the  $\text{Na}^+$  channel is targeted for a drug, the drug works faster and lasts a shorter time than the case that targets the  $\text{K}^+$  channel. Electrophysiological dynamics arising from the different targets can help decide the structural and chemical characteristics of a new drug and its possible reactions can be estimated by using an ion channel model.

An ion channel model can also be used to investigate neural thermosensitivity [69]. It is well known that depolarization and hyperpolarization of ion channel conductances are affected by temperature [103]. The changes in temperature affect the firing pattern of the extracellular action potential, which indirectly shows the changes in IAP. Eventually, the changes in IAP result from the changes in ion channel conductivities. Therefore, the ion channel conductance due to thermosensitivity can be examined by an ion channel model by adding a variable for temperature.

## CHAPTER 7

### CONCLUSION AND FUTURE WORK

To allow for less computational burden and easier implementation, several simplified intracellular action potential (IAP) models have been used. Of these IAP models, Rosenfalck's and Nandedkar's IAP models have been widely accepted to generate muscle IAPs while the Dimitrov and Dimitrova (D-D) IAP model has been recently developed and utilized. However, Rosenfalck's and Nandedkar's IAP models produced unrealistic amplitudes and time durations, and the D-D IAP model has the disadvantage of a difficult implementation. Additionally, previous models have failed to link morphological structure and physiological behavior of ion channels to the IAP model itself. Therefore, a muscle IAP model is required to resolve all the problems that are inherent in previous IAP models.

#### 7.1 CONCLUSION

To understand how IAP in a muscle fiber is generated, it is necessary to examine the main sources for IAP. A muscle fiber is generally surrounded by extracellular fluid, and the area around the muscle fiber has a relatively high concentration of sodium ( $\text{Na}^+$ ). Contrastingly, the inside of a muscle fiber is filled with intracellular fluid that has a relatively high concentration of potassium ( $\text{K}^+$ ). These two main ions,  $\text{Na}^+$  and  $\text{K}^+$ , are the fundamental sources in generating a muscle IAP during cell excitation. A muscle IAP is composed of several typical phases beginning with a rapid increase, then continuing with a relatively slow decrease, and ending with a very slow decreasing phase. These distinctive phases are caused by the inward or outward flow of different ions. However,

typical muscle fibers are enveloped by a special bilayer called the cell membrane that blocks the free flow of ions. To allow ions to pass through the cell membrane, there are special gates called ion channels. Ion channels play a main role in the movement of ions, and the voltage-gated ion channels are dominant on the cell membrane controlling most changes in an IAP. Moreover, each ion channel is permeable only to a specific ion type. For example,  $\text{Na}^+$  can pass the cell membrane only through  $\text{Na}^+$  channels, and  $\text{K}^+$  moves only through  $\text{K}^+$  channels. During the resting state of a muscle fiber, IAP is negatively ranged between -75 and -90 mV. Once a muscle fiber is excited, the conductivity of  $\text{Na}^+$  channels sharply increases which results in the flow of many  $\text{Na}^+$  into the muscle fiber. Due to the rapid increase in  $\text{Na}^+$ , the inside of the muscle fiber starts to be more positively charged, which is called depolarization. Depolarization led by  $\text{Na}^+$  ends within a short period of time, and repolarization starts with  $\text{K}^+$  outward flow activated by opening  $\text{K}^+$  channels. After repolarization, a cell excitation finishes and is presented in IAP by very slow potential decreases until the IAP obtains its initial potential, the so-called resting membrane potential.

Based on these physiological dynamics, a new IAP model is developed using optimization methods. In optimization, an objective function is constructed, which contains all involved ion channels' dynamics. The objective function is composed of three independent Erlang probability density functions (PDF) and each PDF matches with the ion channel conductivity of different ions. Through iterative methods, nine unknown values in the objective function are generated, and these values are adjusted through validation and modification. The final IAP model with calculated values is well matched to several experimental results.

An IAP model is required in generating an Electromyogram (EMG). An EMG is computed by the summation of motor unit action potentials (MUAPs) and a MUAP can be calculated by the summation of the extracellular action potentials (EAPs) in one motor unit. An EAP from a muscle fiber is calculated by the multiplication of a weighted function and the transmembrane current. The weighted function is computed using the inverse distance between a possible measuring point and the muscle fiber location. Also, the transmembrane current can be calculated using the second derivative of the IAP. Due to the interconnected computations for the EMG, development of a precise and realistic IAP model is required, and the IAP model in this study satisfies these requirements.

In addition to being the source in generating an EMG, the IAP model in this study has several advantages over other previous IAP models. First, the IAP model directly shows the separated ion channel conductance model in its equation. As previously explained, a typical IAP is generated by the dynamical changes of ion channel conductances. Therefore, the changes of ion channel conductances have been considered in designing the objective function during optimization. Depending on different values of  $\alpha$ , the type of ion channel is determined which helps to classify which independent function in the IAP model represents what kind of ion channel conductance. By applying the maximum values of ion channel conductance from the experimental results, the dynamics of ion channel conductances are easily generated. Second, the IAP model can be used to examine muscle fiber diseases related to abnormal ion channel activity. Any abnormal changes in ion channel conductances result in an unusual IAP, and it is possible to investigate the major problems by examining independent ion channel conductances. A third advantage is the realistic amplitudes and time duration of the IAP model in this



study. As proved by comparison with several experimental results, the IAP model in this study shows a good matching shape to the real IAP. This implies that the IAP model in this study can be free from the problem of unrealistic IAP generation. It has never been overcome by popular IAP models that are still utilized in EMG generation. The last advantage is the ease of implementation for the generation of the transmembrane current. As explained, the transmembrane current can be calculated by the second derivative of the IAP model. Therefore, the function of an IAP model needs to be continuous in time to be differentiated twice. Notably, the D-D IAP model is unable to be used in calculating the transmembrane current because of its functional discontinuity. The IAP model in this study is developed with continuous functions, and it can be easily implemented to generate the transmembrane current. Overall, the IAP model in this study shows better results in the aspects of being a realistic model and supporting practical applications than other previous IAP models.

## **7.2 FUTURE WORKS**

By developing a new IAP model based on ion channel dynamics, an advanced and accurate IAP model is presented in this study. In particular, an IAP model with meaningful components is designed. However, some components in the developed IAP model are still unknown. For example, the number of closed states in the ion channel is not as clear as other research assumes. Based on the ion channel structures, the possible closed channel states may be presumed, but an exact number of channel states is not known.

The IAP model in this study also has a limitation in explaining the meaning of  $\gamma$ , which is simply used to adjust the IAP model to the reference data. If all other values in the IAP model are correctly assigned and optimized, the values in  $\gamma$  also represent a meaningful component. Instead of directly using the values in  $\gamma$ , however, the maximum conductance values were obtained from the results of an experiment that measured the ion channel conductances. This might be related to the uniqueness of a solution in optimization. Even though the uniqueness was partially resolved by applying different optimization methods, the obtained  $\gamma$  suggests that more research is necessary in the future.

## REFERENCES

1. A. Hadas, L.Kautsky, M. Goek, E.E. Kara, "Rates of Decomposition of Plant Residues and Available Nitrogen in Soil, related to Residue Composition through Simulation of Carbon and Nitrogen Turnover," *Soil Biology and Biochemistry*, Vol. 36, pp 255-266, 2004
2. A. Nekouzadeh, Y. Rudy, "Statistical Properties of Ion Channel Records. Part I: Relationship to the Macroscopic Current," *Mathematical Biosciences*, Vol. 210, pp 291-314, 2007
3. A. Nekouzadeh, Y. Rudy, "Statistical Properties of Ion Channel Records. Part II: Estimation from the Macroscopic Current," *Mathematical Biosciences*, Vol. 210, pp 315-334, 2007
4. A. Randall, P. Baldi, "SELECTpro: Effective Protein Model Selection Using a Structure-based Energy function Resistant to BLUNDERS," *BMC Structural Biology*, Vol. 8, pp 1-16, 2008
5. A. Takeuchi, N. Reyes, P. Artigas, D.C. Gadsby, "The Ion Pathway through the Opened Na<sup>+</sup>, K<sup>+</sup>-ATPase Pump," *Nature*, Vol. 456, pp 413-416, 2008
6. A. Tarntola, B. Valette, "Generalized Nonlinear Inverse Problems Solved Using the Least Square Criterion," *Reviews of Geophysics and Space Physics*, Vol. 20, pp 219-232, 1982
7. A. Tovar, K. Khandelwal, "Uniqueness in Linear and Nonlinear Topology Optimization and Approximate Solutions," *2nd International Conference on Engineering Optimization*, pp 1-10, 2010
8. A.C. Jones, R.K. Wilcox, "Finite Element Analysis of the Spine: Towards a Framework of Verification, Validation and Sensitivity Analysis," *Medical Engineering Pysics*, Vol. 30, pp 1287-1304, 2008
9. A.E. Anderson, B.J. Ellis, J.A. Weiss, "Verification, Validation and Sensitivity Studies in Computational Biomechanics," *Computer Methods in Biomechanics and Biomedical Engineering*, Vol. 10, pp 171-184, 2007
10. A.L. Hodgkin, A.F. Huxley, B. Katz, "Measurement of Current-Voltage realizations in the membrane of the Giant Axon of LOLIGO," *Journal of Physiology*, Vol. 116, pp 424-448, 1952
11. A.L. Hodgkin, A.F. Huxley, "A Quantitative Description of Membrane Current and its Application to Conduction and Excitation in Nerve," *Journal of Physiology*, Vol. 117, pp 500-544, 1952
12. A.L. Hodgkin, A.F. Huxley, "Currents Carried by Sodium and Potassium Ions through the Membrane of the Giant Axon of LOLIGO," *Journal of Physiology*, Vol. 116, pp 449-472, 1952
13. A.L. Hodgkin, A.F. Huxley, "The Components of Membrane Conductance in the Giant Axon of LOLIGO," *Journal of Physiology*, Vol. 116, pp 473-496, 1952
14. A.L. Hodgkin, A.F. Huxley, "The Dual Effect of Membrane Potential on Sodium Conductance in the Giant Axon of LOLIGO," *Journal of Physiology*, Vol. 116, pp 497-506, 1952
15. A.P. Robertson, R.J. martin, "Ion-Channels on Parasite Muscle: Pharmacology and Physiology," *Invertebrate Neuroscience*, Vol. 7, pp 209-217, 2007
16. B. Hammarberg, E. Stålberg, "Novel Ideas for Fast Muscle Action Potential Simulations Using the Line Source Model," *IEEE Transactions on Biomedical Engineering*, Vol. 51, pp 1888-1897, 2004
17. B.K. van Veen, H. Wolters, W. Wallinga, W.L.C. Rutten, H.B.K. Boom, "The Bioelectrical Source in Computing Single Muscle Fiber Action Potentials," *Biophysical Journal*, Vol. 64, pp 1492-1498, 1993

18. B.S. Goh, F.Ye, S.S. Zhou, "Steepest Descent in Unconstrained Optimization with New Step Lengths," (<http://carma.newcastle.edu.au/~jb616/Preprints/Theses/GYZ-Jota.pdf>)
19. C.M. Weaver, S.L. Wearne, "The Role of Action Potential Shape and Parameter Constraints in Optimization of Compartment Models," *Neurocomputing*, Vol. 69, pp 1053-1057, 2006
20. D. Amarantini, L. martin, "A Method to Combine Numerical Optimization and EMG data for the Estimation of Joint Moments under Dynamic Conditions," *Journal of Biomechanics*, Vol. 37, pp 1393-1404, 2004
21. D. Dumitru, J.C. King, W. van der Rijt, D.F. Stegeman, "The Biphasic Morphology of Voluntary and Spontaneous Single Muscle Fiber Action Potentials," *Muscle & Nerve*, Vol. 17, pp 1301-1307, 1994
22. D. Feferic, "Limitations of Gradient Methods in Sequence Learning," *Proceedings of the 9th International Conference on Neural Information Processing*, Vol. 5, pp 2369-2373, 2003
23. D. Randall, W. Burggren, K. French. *Animal Physiology: Mechanisms and Adaptations* (5th edition), New York, W.H. Freeman and Company, 2001
24. D.A. Doyle, J.M. Cabral, R.A. Pfuetzner, A. Kuo, J.M. Gulbis, S.L. Cohen, B.T. Chait, R. MacKinnon, "The Structure of the Potassium Channel: Molecular Basis of K<sup>+</sup> Conduction and Selectivity," *Science*, Vol. 280, pp 69-77, 1998
25. D.C. Camerino, D. Tricarico, J.F. Desaphy, "Ion Channel Pharmacology," *Neurotherapeutics*, Vol. 4, pp 184-198, 2007
26. D.J. Randall, W.W. Burggren, K. French, *Eckert Animal Physiology: Mechanisms and Adaptations*, New York, W H Freeman & Co., 2001
27. D.W. Stashuk, "Simulation of Electromyographic Signals," *Journal of Electromyography and Kinesiology*, Vol. 3, pp 157-173, 1993
28. E. Marban, T. Yamagishi, G.F. Tomaselli, "Topical Review: Structure and Function of Voltage-gated Sodium Channels," *Journal of Physiology*, Vol. 508, pp 647-657, 1998
29. F. Bezanilla, "Ion Channel: From Conductance to Structure," *Neuron*, Vol. 60, pp 456-468, 2008
30. F. Francis, M.R. Garcia, O. Mason, R. Middleton, "A Mathematical Model for Voltage Gated Ion-channel Conduction," *Journal of Theoretical Biology*, ISSN 0022-5193, 2010
31. F.H. Martini. *Fundamentals of Anatomy & Physiology* (7th edition), San Francisco, Pearson Benjamin Cummings, 2006
32. G. Johannsen, "Line Source Models for Active Fibers," *Biological Cybernetics*, Vol. 54, pp 151-158, 1986
33. G. Kim, M. Ferdjallah, "Non-Linear Least Square Optimization of Intracellular Action Potential Model using a Series of Modified Gamma Distribution Functions," *International Symposium Computational Modeling of Objects Presented in Images: Fundamentals, Methods, and Applications*, pp 17-29, 2010
34. G. Kim, M. Ferdjallah, "Single Muscle Fiber Action Potentials Modeling and Simulation," *VMASC Student Capstone Conference*, pp 12-18, 2009
35. G. Yellen, "The Voltage-Gated Potassium Channels and their Relatives," *Nature*, Vol. 419, pp 35-42, 2002
36. G.J. Kaczorowski, O.B. McManus, B.T. Priest, M.L. Garcia, "Ion Channels as Drug Targets: The Next GPCRs," *Journal of Genetic Physiology*, Vol. 131, pp 399-405, 2008
37. G.V. Dimitrov, N.A. Dimitrova, "Precise and Fast Calculation of the Motor Unit Potentials Detected by a point and rectangular plate electrode," *Medical Engineering & Physics*, Vol. 20, pp 374-381, 1998
38. H. Cho, "Data Transformation for Sum Squared Residue," *Advances in Knowledge Discovery and Data Mining*, Vol. 6118, pp 48-55, 2010

39. H.B. Henninger, S.P. Reese, A.E. Anderson, J.A. Weiss, "Validation of Computational Models in Biomechanics," *Journal of Engineering in Medicine*, Vol. 224, pp 801-812, 2009
40. H.K. Thompson, C.F. Starmer, R.E. Whalen, H.D. McIntosh, "Indicator Transit Time Considered as a Gamma Variate," *Circulation Research*, Vol. 14, pp 502-515, 1964
41. H.O. Hartley, "The Modified Gauss-Newton Method for the Fitting of Nonlinear Regression Functions by Least Squares," *Technometrics*, Vol. 3, pp 269-280, 1961
42. H.P. Ludin, "Microelectrode Studies of Normal and dystrophic Human Muscle," *Electroencephalography Clinical Neurophysiology*, Vol. 25, pp 411, 1968
43. I. Babuska, J.T. Oden, "Verification and Validation in Computational Engineering and Science: Basic Concepts," *Computer Methods in Applied Mechanics and Engineering*, Vol. 193, pp 4057-4066, 2004
44. I.A. Gravagne, I.D. Walker, "On the Structure of Minimum Effort Solutions with Application to Kinetic Redundancy Resolution," *IEEE Transactions on Robotics and Automation*, Vol. 16, pp 855-863, 2000
45. J. Clark, R. Plonsey, "A Mathematical Evaluation of the Core Conductor Model," *Biophysical Journal*, Vol. 6, pp 95-112, 1966
46. J. Duchene, J.Y. Hogrel, "A Model of EMG Generation," *IEEE Transactions on Biomedical Engineering*, Vol. 47, pp 192-201, 2000
47. J. Keener, "Invariant Manifold Reductions for Markovian Ion Channel Dynamics," *Journal of Mathematical Biology*, Vol. 58, pp 447-457, 2009
48. J. Otamendi, "The Importance of the Objective Function Definition and Evaluation in the Performance of the Search Algorithms," *Proceedings 16th European Simulation Symposium*, 2004
49. J. Zhang, Y. Xiao, Z. Wei, "Nonlinear Conjugate Gradient Methods with Sufficient Descent Condition for large-Scale Unconstrained Optimization," *Mathematical Problems in Engineering*, pp 1-16, 2009
50. J.D. Markman, R.H. Dworkin, "Ion Channel Targets and Treatment Efficacy in Neuropathic Pain," *The Journal of Pain*, Vol. 7, pp 538-547, 2006
51. J.H. Kaplan, "The Sodium Pump and hypertension: A Physiological Role for the Cardiac Glycoside Binding Site of the Na,K -ATPase," *Proceedings of the National Academy of Science*, Vol. 102, pp 15723-15724, 2005
52. J.P. Morth, B.P. Pedersen, M.S. Toustrup-Jensen, T.L.M. Sorensen, J.Petersen, J.P. Andersen, B. Vilsen, P. Nissen, "Crystal Structure of the Sodium-Potassium Pump," *Nature*, Vol. 450, pp 1043-1050, 2007
53. J.R. Falces, A.M. Trigueros, L.G. Useros, I.R. Carreno, J.N. Irujo, "A Mathematical Analysis of SFAP Convolutional Models," *IEEE Transactions on Biomedical Engineering*, Vol. 52, pp 769-783, 2005
54. J.R. Falces, A.M. Trigueros, L.G. Useros, I.R. Carreno, J.N. Irujo, "Modeling Fibrillation Potentials – A New Analytical Description for the Muscle Intracellular Action Potential," *IEEE Transactions on Biomedical Engineering*, Vol. 53, pp 581-592, 2006
55. J.S. Dyer, P.C. Fishburn, R.E. Steuer, J. Wallenius, S. Zionts, "Multiple Criteria Decision Making, Multiattribute Utility Theory: The Next Ten Years," *Management Science*, Vol. 38, pp 645-654, 1992
56. K. Liu, P. Zhang, J. Shao, X. Zhu, Y. Zhang, J. Bai, "A 2D Strain Estimator with Numerical Optimization Method for Soft-Tissue Elastography," *Ultrasonics*, Vol. 49, pp 723-732, 2009
57. K.C. McGill, Z.C. Lateva, S. Xiao, "A Model of the Muscle Action Potential for Describing the Leading Edge, Terminal Wave, and Slow Afterwave," *IEEE Transactions on Biomedical Engineering*, Vol. 48, pp 1357-1365, 2001

58. K.C. McGill, Z.C. Lateva, "A Model of the Muscle-Fiber Intracellular Action Potential Waveform, Including the Slow Repolarization Phase," *IEEE Transactions on Biomedical Engineering*, Vol. 48, pp 1480-1483, 2001
59. K.G. Keenan, F.J. Valero-Cuevas, "Experimentally Valid Predictions of Muscle Force and EMG in Models of Motor-Unit Function Are Most Sensitive to neural Properties," *Journal of Neurophysiology*, Vol. 98, pp 1581-1590, 2007
60. L. Mesin, M. Joubert, T. Hanekom, R. Merletti, D. Farina, "A Finite Element Model for Describing the Effect of Muscle Shortening on Surface EMG," *IEEE Transactions on Biomedical Engineering*, Vol. 53, pp 593-600, 2006
61. L. Moffatt, "Estimation of Ion Channel Kinetics from Fluctuations of Macroscopic Currents," *Biophysical Journal*, Vol. 93, pp 74-91, 2007
62. M. Gurkiewicz, A. Korngreen, "A numerical Approach to ion Channel Modeling Using Whole-Cell Voltage-Clamp Recordings and a Genetic Algorithm," *Computational Biology*, Vol. 3, pp 1633-1647, 2007
63. M. Ishikawa, P.V. Komi, "Muscle Fascicle and Tendon Behavior During Human locomotion Revisited," *Exercise & Sport Science Reviews*, Vol. 36, pp 193-199, 2008
64. M. Mischi, J.A. den Boer, H.H.M. Korsten, "On the Physical and Stochastic Representation of an Indicator Dilution Curve as a Gamma Variate," *Physiological Measurement*, Vol. 29, pp 281-294, 2008
65. M. Nakatsui, K. Horimoto, M. Okamoto, Y. Tokumoto, J. Miyake, "Parameter optimization by Using Differential Elimination: A General Approach for Introducing Constraints into Objective Functions," *BMC Systems Biology*, Vol. 4, pp 90-101, 2010
66. M. Nakatsui, K. Horimoto, "Parameter Optimization in Network Dynamics Including Unmeasured Variables by the Symbolic-Numeric Approach," *The Third International Symposium on Optimization and System Biology*, pp 20-22, ORSC & APORC, Zhangjiajie, China, 2009
67. M. Rana, G. Hamarneh, J.M. Wakeling, "Automated Tracking of Muscle Fascicle Orientation in B-Mode Ultrasound Images," *Journal of Biomechanics*, Vol. 42, pp 2068-2073, 2009
68. M. Viceconti, S. Olsen, L. P. Nolte, K. Burton, "Extracting Clinically Relevant Data from Finite Element Simulations," *Clinical Biomechanics*, Vol. 20, pp 451-454, 2005
69. M. Wechselberger, C.L. Wright, G.A. Bishop, J.A. Boufant, "Ionic Channels and Conductance-Based Models for Hypothalamic Neural Thermosensitivity," *American Journal of Physiology – Regulatory, Integrative and Comparative Physiology*, Vol. 291, pp R518-R529, 2006
70. M. Zeleny, "Multiple Criteria Decision Making: Eight Concepts of optimality," *Human System Management*, Vol. 17, pp 97-107, 1998
71. M. Zwolak, J. Wilson, M.D. Ventra, "Dehydration and Ionic Conductance Quantization in Nanopores," *Journal of Physics: Condensed Matter*, Vol. 22, pp 1-12, 2010
72. M.M. Lowery, N.S. Stoykov, P.A. Dewald, T.A. Kuiken, "Volume Conduction in an Anatomically based Surface EMG Model," *IEEE Transactions on Biomedical Engineering*, Vol. 51, pp 2138-2147, 2004
73. M.R. Hestenes, E. Stiefel, "Methods of Conjugate Gradient for Solving Linear Systems," *Journal of Research of the National Bureau of Standards*, Vol. 49, pp 409-436, 1952
74. P. Kienker, "Equivalence of Aggregated Markov Models of Ion-Channel Gating," *Proceedings of the Royal Society of London B: Biological Sciences*, Vol. 236, pp 373-377, 1989

75. P. Rosenfalck, "Intra- and Extracellular Potential Fields of Active Nerve and Muscle Fibers. A Physico-mathematical Analysis of Different Models," *Acta Physiologica Scandinavica*, Vol. 321, pp 15-146, 1969
76. P. Venkataraman, *Applied Optimization with MATLAB Programming*, New York, Wiley-Interscience, 2002
77. P. Zhou, N.L. Suresh, W.Z. Rymer, "Model Based Sensitivity Analysis of EMG-Force Relation with Respect to Motor Unit Properties: Applications to Muscle Paresis in Stroke," *Annals of Biomedical Engineering*, Vol. 35, pp 1521-1531, 2007
78. P.H. Kleinpenning, T.H.J.M. Gootzen, A.V. Oosterrom, D.F. Stegeman, "The Equivalent Source Description Representing the Extinction of an Action Potential at a Muscle Fiber Ending," *Mathematical Bioscience*, Vol. 101, pp 41-61, 1990
79. R. Fletcher, C.M. Reeve, "Function Minimization by Conjugate Gradients," *The Computer Journal*, Vol. 7, pp 149-154, 1964
80. R. Merletti, L.L. Conte, E. Avignone, P. Guglieminotti, "Modeling of Surface Myoelectric Signals-Part I: Model implementation," *IEEE Transactions on Biomedical Engineering*, Vol. 46, pp 810-820, 1999
81. R. Plonsey, "Action Potential Sources and their Volume Conductor Fields," *IEEE Transactions on Biomedical Engineering*, Vol. 56, pp 601-611, 1977
82. R. Schwartz, *Biological Modeling and Simulation*, London, The MIT Press, 2008
83. R.F. Ker, "The Implications of the Adaptable Fatigue Quality of Tendons for Their Construction, Repair, and Function," *Comparative Biochemistry and Physiology (Part A)*, Vol. 133, pp 987-1000, 2002
84. R.G. Pensa, J.F. Boulicaut, "Numerical Data Co-clustering via Sum-Squared Residue Minimization and User-Defined Constraint Satisfaction," *Process of 16th Italian Symposium on Advanced Database Systems*, pp 279-286, 2008
85. R.J. Schilling, S.L. Harris, *Applied Numerical Methods for Engineers: using MATLAB and C*, Pacific Grove, Brooks/Cole Publishing Company, 2000
86. R.L. Evans, "Two Comments on the Estimation of Blood Flow and Central Volume from Dye-Dilution Curves," *Journal of Applied Physiology*, Vol. 14, pp 457, 1959
87. R.M. Alexander, "Tendon Elasticity and Muscle Function," *Comparative Biochemistry and Physiology (Part A)*, Vol. 133, pp 1001-1011, 2002
88. S. Abbasbandy, A. Jafarian, "Steepest Descent Method for Solving Fuzzy Nonlinear Equations," *Applied Mathematics and Computation*, Vol. 174, pp 669-675, 2006
89. S. Andreassen, A. Rosenfalck, "Relationship of Intracellular and Extracellular Action Potentials of Skeletal Muscle Fibers," *Critical Reviews in Bioengineering*, Vol. 6, pp 267-306, 1981
90. S. Dutertre, R.J. Lewis, "Use of Venom Peptides to Probe Ion Channel Structure and Function," *Journal of Biological Chemistry*, Vol. 285, pp 13315-13320, 2010
91. S. Hanna, "Defining Implicit Objective Functions for Design Problems," *Genetic and Evolutionary Computation Conference*, pp 2013-2020, 2007
92. S. Lee, A. Lee, J. Chen, R. MacKinnon, "Structure of the KvAP Voltage-Dependent K<sup>+</sup> Channel and its Dependence on the Lipid Membrane," *Proceedings of the National Academy of Sciences of the United States of America*, Vol. 102, pp 15441-14556, 2005
93. S. Manttari, T. Traskback, M. Jarvilehto, "Sodium Channel Development Changes the Conduction Velocity in Skeletal Muscle," *Basic Applied Myology*, Vol. 15, pp 23-28, 2005
94. S.B. Long, E.B. Campbell, R. MacKinnon, "Crystal Structure of a Mammalian Voltage-Dependent Shaker Family K<sup>+</sup> Channel," *Science*, Vol 309, pp 897-907, 2005
95. S.D. Nandedkar, E. Stålberg, "Simulation of Single Muscle Fiber Action Potentials," *Medical & Biological Engineering & Computing*, Vol. 21, pp 158-165, 1983

96. T.C. Krejcie, J.A. Jacquez, M.J. Avram, C.U. niemann, C.A. shanks, T.K. Henthorn, "Use of Parallel Erlang Density Functions to Analyze First-pass Pulmonary Uptake of Multiple Indicators in Dogs," *Journal of Pharmacokinetics and Pharmacodynamics*, Vol. 24, pp 569-588, 1996
97. T.I Arabadzhiev, G.V. Dimitrov, V.E. Chakarov, A.G. Dimitrov, N.A. Dimitrova, "Effects of Changes in Intracellular Action Potential on Potentials Recorded by Single Fiber, Macro, and Belly-Tendon Electrodes," *Muscle & Nerve*, Vol.37, pp 700-712, 2008
98. T.I Arabadzhiev, G.V. Dimitrov, V.E. Chakarov, A.G. Dimitrov, N.A. Dimitrova, "factors Affecting the Turns Analysis of the Interference EMG Signal," *Biomedical signal Processing and Control*, Vol. 3, pp 145-153, 2008
99. T.I Arabadzhiev, V.G. Dimitrov, N.A. Dimitrova, G.V. Dimitrov, "Influence of Motor unit Synchronization on Amplitude Characteristics of Surface and Intramuscularly Recorded EMG Signals," *European Journal of Applied Physiology*, Vol. 108, pp 227-237, 2010
100. T.I. Arabadzhiev, G.V. Dimitrov, N.A. Dimitrova, "Intracellular Action Potential Generation and Extinction Strongly Affect the Sensitivity of M-wave Characteristic Frequencies to Changes in the Peripheral Parameters with Muscle Fatigue," *Journal of Electromyography and kinesiology*, Vol. 15, pp 159-169, 2005
101. V.V. Gursky, K.N. Kozlov, A.M. Samsonov, "Combined Optimization Technique for Biological Data Fitting," *Computational System Biology*, pp 60-63, 2004
102. W. Stühmer, "Structure-Function Studies of Voltage-gated Ion channels," *Annual Review of Biophysical Chemistry*, Vol. 20, pp 65-78, 1991
103. W.A. Catterall, K.G. Chandy, G.A. Gutman, "The IUPHAR Compendium of Voltage-Gated ion Channel," *International Union of Pharmacology Media*, 2002
104. W.W. Hager, H.Zhang, "A Survey of Nonlinear Conjugate Gradient Methods," *Pacific Journal of Optimization*, Vol. 2, pp 35-58, 2006
105. W.W.D. Jonge, F.L.H. GIELEN, P. Wirtz, P.D. Jong, J. Broenink, "The Different Intracellular Action Potentials of Fast and Slow Muscle Fibers," *Electroencephalography and Clinical Neurophysiology*, Vol. 60, pp 539-547, 1985
106. Y.H. Dai, Y. Yuan, "A Nonlinear Conjugate Gradient Method with a Strong Global Convergence Property," *SIAM Journal on Optimization*, Vol. 10, pp 177-182, 2000
107. Z. Chen, J.R. Tristano, W. Kwok, "Construction of an Objective Function for Optimization-based Smoothing," *Engineering with Computers*, Vol. 20, pp 184-192, 2004
108. Z. Shi, J. Shen, "Step-size Estimation for Unconstrained Optimization Methods," *Computational and Applied Mathematics*, Vol. 24, pp 399-416, 2005
109. Z. Yang, A. Elgamal, "Application of Unconstrained Optimization and Sensitivity Analysis to Calibration of a Soil Constitutive Model," *International Journal for Numerical Analytical Methods in Geomechanics*, Vol. 27, pp 1277-1297, 2007
110. [http://en.wikipedia.org/wiki/Voltage\\_clamp](http://en.wikipedia.org/wiki/Voltage_clamp)



## VITA

GyuTae Kim  
 Department of Electrical and Computer Engineering  
 Old Dominion University  
 Norfolk, VA 23529

### *EDUCATION*

Ph.D. Electrical and Computer Engineering, Old Dominion University, 2011  
 M.S. Electrical Engineering, University of Tennessee, 2008  
 M.E. Bioengineering, University of Utah, 2004  
 B.E. Electrical Engineering, Honk-Ik University, Korea, 1999

### *WORKING EXPERIENCES*

2010-Current Research / Teaching Assistant, Old Dominion University, Norfolk, USA  
 2009 Research Assistance, Old Dominion University, Norfolk, USA  
 2005-2008 Research / Teaching Assistant, University of Tennessee, Knoxville, USA  
 2003-2004 Research Assistance, University of Utah, Salt Lake City, USA  
 1994-1995 Communication Battalion in Military Service, DaeGu, Korea

### *PUBLICATIONS*

Mohammed Ferdjallah, **GyuTae Kim**, "Organ System Modeling", in Modeling and Simulation in the Medical and Health Sciences, Sokolowski JA, Banks C, John Wiley & Sons, 2011  
**GyuTae Kim**, Mohammad A. Ahad, Mohammed Ferdjallah, "Modeling & Simulation of the Effects of Pathological Changes on Computer Generated Muscle Action Potentials", 7<sup>th</sup> International Bioelectrics Symposium, 2010 Jun 24.  
**GyuTae Kim**, Mohammed Ferdjallah, "Non-Linear Least Square Optimization of Intracellular Action Potential Model Using a Series of Modified Gamma Distribution Functions", Computational Modeling of Objects Presented in Images: Fundamentals, Methods, and Applications, 2010 May: 17-29.  
**GyuTae Kim**, Mohammed Ferdjallah, Gerald Harris, "Fast Computational Analysis of Sway Area Using Center of Pressure Data in Normal Children and Children with Cerebral Palsy", American Journal of Biomedical Science, 2009 Jul; 1(4): 364-372.  
**GyuTae Kim**, Mohammed Ferdjallah, Gerald Harris, "Fast Differential Analysis of Center of Pressure Data in Normal Children and Children with Cerebral Palsy", Southern Biomedical Engineering Conference, 2009 May; 24(22): 341-342.  
**GyuTae Kim**, Mohammed Ferdjallah, "Single Muscle Fiber Action Potentials Modeling and Simulation", VMASC Student Capstone Conference, 2009 April: 12-18.  
**GyuTae Kim**, Mohammad Ahad, Mohammed Ferdjallah, Gerald Harris, "Correlation of Muscle Fatigue Indices between Intramuscular and Surface EMG Signals", Proceedings IEEE Southeastern Conference, 2007 Mar: 378-382.